MULTI-SCALE MODELLING OF ORGANIC PHOTOVOLTAICS SYSTEM P3HT:PCBM

TO TRAN THINH
B.Eng.(Hons.), NUS

A THESIS SUBMITTED FOR THE DEGREE OF DOCTOR OF PHILOSOPHY

DEPARTMENT OF MATERIALS SCIENCE AND ENGINEERING

NATIONAL UNIVERSITY OF SINGAPORE

2014

DECLARATION

I hereby declare that the thesis is my original work and it has been written by me in its entirety.
I have duly acknowledged all the sources of information which have been used in the thesis.

This thesis has also not been submitted for any degree in any university previously.

To Tran Thinh
5th Aug 2014

Acknowledgement

First and foremost, I would like to thank my supervisor, Associate Professor Stefan Adams for his scientific guidance, advice, patience and the relentless and heart-warming support for my works without which all of this would not have been possible. It was the extended discussions, the long-hours of brainstorming that have not only inspired me to keep pushing for new heights and soliciting new insights but also taught me how to think logically and systematically which, I believe, would benefit me in all my future endeavours.

I would like to thank the National University of Singapore (NUS) for giving me the opportunity to learn, to research and to immerse in the vibrantly rich culture of one of the best higher education institutes in the world. While the time I spent here is nigh to a decade, it feels short and with much more that I can do and learn. I made some of the best friends of my life here, from whom I have learnt much and there are still much more to learn from.

I would like to thank the Solar Energy Research Institute of Singapore for funding my PhD study and research. It is also here that I met some of the most talented scientists: Dr. Krishnamoorthy Ananthanarayana, who have aided me handsomely in device fabrications, device physics and the experimental aspects of organic solar cell; Professor Luther Joachim, whose vision of joining detailed molecular simulations with continuum, device level studies is one of its kind which has kept the group organised and focused; Associate Professor Peter Ho, whose expertise on organic solar cells have helped improved the scientific understanding of device physics as well as the technical aspects of the manuscripts. I am also grateful for the opportunity to learn and obtain the “Red Hat Certified Engineer” certification. The knowledge of which has tremendously smoothened my works in the past three years.

I would like to thank Mr. Yap Jing Han, my Final Year Project student, for his tenacious diligence that allows him to complete the tasks assigned with flying colours. Without some of his creative solutions, insights, tenacity, much of the results presented here under the Monte Carlo simulation part (see Section 2.4) would not have been possible.

Contents

Summary

Understanding of active layer morphology evolution and device physics in poly(3-hexyl thiophene) (P3HT) and phenyl-C61-butyric acid methyl ester (PCBM) Organic Photovoltaics (OPV) is crucial towards the improvement of device performance. The current lack of a solid theoretical framework at both the molecular and device level means that progress in OPV is not guided by strongly founded theoretical principles but via a more trial-and-error approach. Hence progress is slow and sparse. In particular, there is a missing link between existing insight at the atomistic or sub-atomistic and continuum device level. While ab-initio techniques are accurate, they lack the ability to simulate device level systems. On the other hand although continuum methods are more relevant to experimental work due to the similar dimension and time scale, they lack the ab-initio essence. Therefore in many cases the computational studies at the atomistic level are not able to directly provide the relevant input for the continuum level simulations, and the continuum level simulations have to resort to coarse estimates or (error-prone) experimental inputs, hence reducing the predictive power of the model. Having a consistent continuous theoretical framework spanning from ab-initio all the way to continuum level is an important step towards a unified and accurate model that could guide both device fabrication and molecular design relevant for high performance OPV. The aim of this work is thus focused on three main tasks:

1. Employ ab-initio simulation results to deduce new and improved modelling tools at atomistic as well as at coarser scale, which could shed more light of the mechanism of morphology evolution and charge transport.
2. Use the new tools to study the underlying mechanism affecting morphology evolution and charge transport in the photoactive layer. And, thereby, correlating morphological features and charge transport behaviour.

3. To show up a pathway for bridging the gap between atomistic and continuum level simulations. This step is important for future work where a complete theoretical framework joining atomistic and device simulation can be achieved.

To this end, a multi-scale simulation approach was developed in this work that goes from first-principles Density Functional Theory (DFT) methods to a more empirical Molecular Dynamics (MD) simulation which then goes onto a coarse-grained MD that is capable of even larger scale simulations infeasible with DFT techniques. We also introduce Monte Carlo (MC) simulations that use inputs from coarse-grained MD and thereby create a fluid transition from molecular or discrete simulation to continuum level simulations. Moreover, a first-principles charge transport model was developed to correlate morphology and charge transport directly relevant for device performance. A more detailed layout of the thesis is presented below.

In the early stage of the project, Molecular Dynamics (MD) and ab-initio methods are used in conjunction with one another to simulate the systems at the atomistic level. While MD makes possible modelling of relatively large system, ab-initio allows accurate validation of MD results where experimental data is not available. Furthermore, many important device physical properties can only be studied in great details with ab-initio. Base on ab-initio Density Functional Theory (DFT) calculations, we were able to improve the accuracy of our MD simulation. Furthermore, by applying coarse-graining method, we also succeeded in enhancing MD calculation speed to more than 200 times. This was done by represent each rigid group of atoms with an effective bead (eg. C_{60} cage, carbonyl group in PCBM and thiophene ring, side chain segments in P3HT). 88 atoms in PCBM were reduced to 5 beads and 60 atoms in the P3HT monomer were reduced to 6 beads. Using the coarse-grained forcefield, we studied the P3HT:PCBM interface at different P3HT orientations. The results suggest that face-on is the most stable interfacial

configuration; crystalline P3HT:PCBM is more stable than amorphous P3HT:PCBM; and PCBM can only through amorphous P3HT or grain boundaries in case of crystalline P3HT. This leads to the conclusion that phase separation in blended P3HT:PCBM bulk heterojunction is carried out via P3HT nucleation crystallization at the interface followed by diffusion of PCBM out of crystalline P3HT-rich region. To further speedup the active layer morphology simulation, P3HT:PCBM interfacial energy changes as a function of underlying P3HT thickness calculated using coarse-grained forcefield was employed for Monte Carlo (MC) simulations. This work allows us to see the effect of different blend ratios on the final morphology. Analysis of the phase separated domains sizes, volume of percolating domains[1] and P3HT:PCBM interfacial areas of phase separating domains suggests that 1:1 blend ratio is most optimal for both a balance holes, electrons percolation pathways and domain size ideal for exciton diffusions. We also studied the effect of pre-grown P3HT crystals on final P3HT:PCBM morphology and found that pre-grown crystal allows speeding up of domains formation in the early stage especially at the seed crystal sites where nucleation is not required. This means that for actual devices, sufficient pattern of P3HT crystals grown before thermal treatment could help influence the resultant active layer morphology.

To corroborate the active layer morphology and device performance, a charge transport model based on semi-classical Hückel method and Marcus theory was also developed for conjugated system. In the earlier attempts, only conjugated system (P3HT) was modelled directly while was treated as part of the metal-like electrode using Two Dimensional Electron Gas (2-DEG) model. The model was then extended such that PCBM is now incorporated inside the system Hamiltonian allowing for seamless simulation of dark current-voltage (J-V) curves and light absorption

[1] Please note that the term "percolating" in this context (and subsequent contexts within the thesis unless otherwise stated) refers to the domains that are in direct contact with the corresponding electrode.

spectrum. The model also incorporated morphological information obtained from both atomistic and coarse-grained MD simulations in order to elucidate the correlation between morphology and charge transport performance. Light absorption calculations suggested that this process is a pre-dominantly intra-chain transport with the broad peak at 500 – 540 nm and the 600 nm shoulder in the crystalline case is attributed to 1-2 hopping and 1-3 hopping respectively. Dark J-V calculations suggested that the process is predominantly inter-chain while optimal P3HT inter-chain coupling energy was found at 0.39 eV, midway between fully crystalline (0.56 eV) and fully disordered (0.11 eV) systems. Furthermore, the maximisation of the closet distance between phenyl group on PCBM and thiophene group on P3HT were also shown to lead to larger interfacial HOMO/LUMO mismatch and consequently lower leakage energy under illuminated conditions.

A short flowchart laying out the multi-scale modelling approached employed in this work can be seen in Figure 1. In short, the methodology is general and applicable to similar systems to elucidate important physical and chemical characteristics. Since the study presented here is based purely on multi-scale theoretical approach with minimal needs for experimental input, the framework can be used to predict and guide the molecular design of active layer materials relevant for high performance OPV devices. This also provides a seamless input that can smoothly transition into continuum simulation at device level scale where results are closely comparable to experimental values. Such a strategy has been successfully implemented for silicon-based solar cell and now, with the help of this work, is closer to realization for OPV.

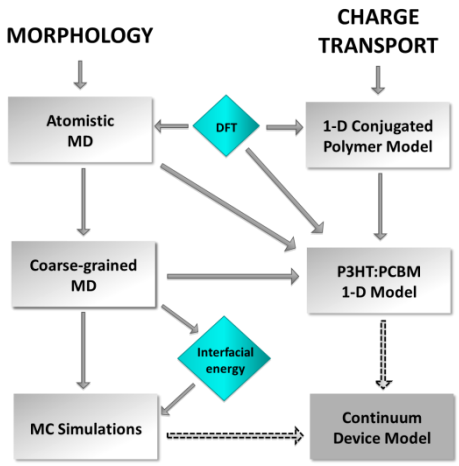

Figure 1. Summary of the flow of the multi-scale simulation performed in this work. Ab-initio DFT methods were employed to refined atomistic MD forcefields. MD forcefield and experimental information were then used to derive coarse-grained MD forcefield for more efficient morphology study. Using the interfacial energy profile calculated with the new coarse-grained, a MC scheme for morphology evolution was suggested. For charge transport, we established a 1-D charge transport model for conjugated polymer which was then expanded to include both donor and acceptor in OPV. The model uses input from DFT, atomistic and coarse-grained MD for 1-D device modelling. The morphology and charge transport information from MC model and 1-D charge transport model can be utilized in continuum device level simulation thereby providing a possible pathway to bridge the gap between molecular models and continuum device models.

List of Figures

List of Tables

Glossary

2-DEG	Two-Dimensional Electron Gas
AFM	Atomic Force Microscopy
DFT	Density Functional Theory
DP	Degree of Polymerization
DSIMS	Dynamic Secondary Ion Mass Spectrometry
EAM	Embedded Atom Model
EPBT	Energy Pay-Back Time
ET	Electron Tomography
FFT	Fast Fourier Transform
GDM	Gaussian Disorder Model
GISAXS	Grazing Incidence Small-Angle X-ray Scattering
HOMO	Highest Occupied Molecular Orbital
ITO	Indium Tin Oxide
JSC	Short Circuit Current
J-V	Current-Voltage Curve
LCAO	Linear Combination of Atomic Orbitals
LUMO	Lowest Unoccupied Molecular Orbital
MC	Monte Carlo
MCB	Monochlorobenzene
MD	Molecular Dynamics
MRC	Marcon, Rao and Cheung P3HT Forcefield
MW	Molecular Weight
NPT	Constant Temperature and Constant Pressure Ensemble
oDCB	Ortho-dichlorobenzene
OLED	Organic Light Emitting Diode
OPV	Organic Photovoltaics
P3HT	Poly(3-hexyl thiophene)

PBE	Perdew-Burke-Ernzerhof
PCBM	Phenyl-C61-butyric Acid Methyl ester
PCDTBT	Poly[N-9”-hepta-decanyl-2,7-carbazole-alt-5,5-(4’,7’-di-2thienyl-2’,1’,3’-benzothiadiazole)
PCPDTBT	Poly[2,6-(4,4-bis- (2-ethylhexyl)-4H-cyclopenta[2,1-b;3,4-b’]dithiophene)-alt-4,7-(2,1,3-benzothiadiazole)]
PEDOT	Poly(3,4-ethylenedioxythiophene)
PF10TB	Poly(9,9-didecanefluorene-alt-(bis-thienylene) benzothiadiazole)
PSS	Poly(styrene sulfonate)
rms	Root-mean-square
RSoXS	Resonant Soft X-ray Scattering
SEM	Scanning Electron Microscope
SPM	Scanning Probe Microscopy
SSH	Su, Schrieffer and Heeger Polaron Model
TCO	Transparent Conducting Oxide
TD-DFT	Time Dependant Density Functional Theory
TEM	Transmission Electron Microscopy
VdW	Van der Waals

Symbols and Mathematical Notations

k_{bonds}	Bond stretch harmonic coefficient
k_{angle}	Bond angle harmonic coefficient
r	Bond length
r_0	Equilibrium bond length
θ	Bond angle
θ_0	Equilibrium bond angle
V_1, V_2, V_3, V_4	Torsional energy parameters
φ	Torsion angle
q_i, q_j	Coulomb charges of atom i and atom j
ϵ_{ij}	Van der Waals bond strength between atom i and atom j
σ_{ij}	Equilibrium Van der Waals bond length between atom i and atom j
r_{ij}	Distance between atom i and atom j
L	Lagrangian of the system (= 'kinetic energy' minus 'potential energy)
p_i	Momentum of particle i
$A_{i,j}$	Long-range interaction constant between atom i and atom j
$\mathbf{r}_i, \mathbf{r}_j$	Position vectors of atom i and atom j
$\mathbf{R}_L$	Lattice translation vector
m	Determine the type of long-range interaction (e.g. $m = 1$ for Coulomb interaction and $m = 6$ or 12 for VdW interactions)
η	Constant that determines how fast Ewald summations would converge in real space and reciprocal space
erf	Error function
erfc	Complimentary error function
H	Hamiltonian of the system (= 'kinetic energy' plus 'potential energy)
ψ	Wavefunction of the system
m_i	Mass of particle i
∇	Laplace operator $\left(\nabla = \sum_{i=1}^{3} \frac{\partial^2}{\partial x_i^2}\right)$
U	Potential energy
E	Energy level of the system
$\rho(\mathbf{r})$	Electronic density at point '$\mathbf{r}$'
φ_i^{KS}	Kohn-Sham orbital
$\hat{V}_{eff}$	Effective potential energy

$\widehat{U}_{el}$	Coulomb repulsion between electrons
$\widehat{V}_{ext}$	the potential caused by nuclei
S	Orientational order parameter
u	Orientation vector of individual entity
n	Average orientation vector
$E(L)$	Interfacial energy
E_0	Equilibrium interfacial energy
L	Thickness of underlying layer (adjacent to the interface of interest)
λ^*	Effective screening length
G	Gibbs free energy
T	Temperature
Ω	Degeneracy of the current state
$rand$	Random number in the interval [0,1]
λ	Reorganization energy
ω	Angular frequency
σ	Electronic conductivity
μ_D	Electron mobility
v_F	Fermi velocity or the average velocity of conducting electron
E_F	Fermi energy level
$g(E)$	Density of state
$f(E)$	Fermi Dirac distribution
c	Speed of light ($c = 3 \cdot 10^8\ m \cdot s^{-1}$)
h	Planck constant ($h = 6.63 \cdot 10^{-34} J \cdot s$)
k_B	Boltzmann constant ($k_B = 1.38 \cdot 10^{-23} J \cdot K^{-1}$)
m_e	Electron mass ($m_e = 9.11 \cdot 10^{-31} kg$)
h	Planck constant ($h = 6.63 \cdot 10^{-34} J \cdot s$)
$\hbar$	Reduced Planck constant $\left(\hbar = \frac{h}{2\pi}\right)$
q	Electronic charge ($q = 1.602 \cdot 10^{-19} C$)

CHAPTER 1: Introduction

1.1. Overview

The interest in organic electronics started with the discovery of the first organic semiconductor in 1954 which was a charge transfer complex of perylene-bromine.[1] In 1978, polymeric semiconductors came to the scene with the discovery of highly conductive polyacetylene especially when doped with iodine.[2] It turned out that the presence of a conjugated backbone is essential to the conductivity of polymeric materials making polyacetylene the simplest conceivable polymeric semiconductor. Unlike silicon or inorganic materials based, organic semiconductors can be made by relatively cheap solution processing techniques, hence attracting a lot of research attentions. Today, we can find organic materials in a widespread of commercialised products, most noteworthy is organic light emitting diode (OLED) and Organic Photovoltaics (OPV). Application of organic semiconductor in photovoltaic started much later in 1983 where the first OPV cell with the active layer consisting solely of a single polymeric compound was reported with low efficiency of much less than 1%.[3] The main reason for the suboptimal result is the drastic difference in hole and electron mobility. For Poly(3-hexyl thiophene) (P3HT), for instance, the hole mobility is two orders of magnitude higher than its electron mobility.[4] Furthermore, unlike for silicon based solar cells, light absorption in OPV results in the formation of Frenkel excitons rather than electron-hole pairs. Excitons are bound electron and holes over short distances with a binding energy of ca. 0.5eV, which is much higher than thermal energy under typical ambient conditions, hence, excitons do not dissociate readily.[5] In 1986, Tang suggested the addition of an electron extractor/acceptor to the active layer, hence creating a first bilayer OPV which was demonstrated to reach a new efficiency height of 1%.[6] While this approach was able

to solve the differential mobility problem, the efficiency of charge separation remains one of the limiting factors for OPV devices: Although with the energy gap between the conduction bands (or Lowest Unoccupied Molecular Orbital (LUMO) in the case of organic conductors) of acceptor and donor greater than the binding energy of the exciton, dissociation should take place readily, in reality, excitons are short-lived and only have diffusion length of ca. 10nm, hence only a portion of the bilayer OPV is actively contributing to the overall device performance.[7] To overcome this issue, in 1995 Heeger and his group introduced the bulk heterojunction concept which combines acceptor and donor into one blended network of donor rich and acceptor rich regions, thus, greatly increasing donor/acceptor interface areas and hence potential sites for excitons dissociation; consequently boosting the photocurrent (ca. Figure 2b).[8] However, engineering an optimal bulk heterojunction remains a challenge due to the lack of understanding in the dynamics of morphology evolution of polymer blends. For instance, it was reported that the presence of the acceptor phenyl-C61-butyric acid methyl ester (PCBM) coerces the crystallisation process of P3HT leading to an overall reduced degree of crystallinity, and hence, lower charge transport efficiency.[9] On the other hand, an adequate theory for charge transport in organic semiconductor is also missing making trial and error or (not always correct) analogies to inorganic semiconductors the primary pathways towards deriving higher performing OPV active layer materials.[10]

Despite the shortcomings, OPV is still very appealing to researchers due to the potentially low cost of materials, as well as the cheap and readily available manufacturing techniques. The interest in OPV has increased tremendously in the past few years and is clearly evident in the increment of device efficiency from sub 1% in 1986 to more than 10% in the certified small-molecule champion cell.[11, 12] An illustration of OPV progress in the past 8 years can be seen in Figure 2a.

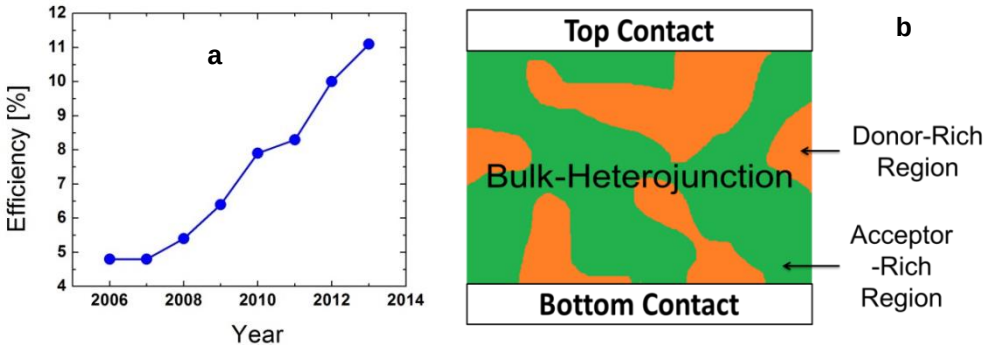

Figure 2. a) Graph of OPV efficiencies achieved in the past 8 years shows large improvements as a result of increased research interest. Data was collected from [11-20]. b) Schematic layout of bulk heterojunction active layer in OPV with a blended network of donor rich and acceptor rich regions.

A typical bulk heterojunction OPV consist of three distinct layers, the bottom contact, the photoactive layer (or bulk heterojunction layer) and the top contact. A common setup of a photoactive layer in OPV generally consists of an absorber (or donor) material and an acceptor material. The absorber acts as a light absorption medium where photons are converted into excitons. These will diffuse into the donor/acceptor interface region and dissociate into electrons and holes that are collected at the respective electrodes. However, the simplified diffusion model could be superseded by coherent photon absorption which offered compelling explanation for observed ultra-fast excitons dissociation.[21] On the other hand, since exciton dissociations occur at the interface, bulk-heterojunction is ideal in maximizing the interfacial area. Nevertheless, an uncontrolled morphology evolution could lead to isolated phases that raise the rate of charge recombinations. Active layer morphology could be controlled experimentally using additives such as nanoparticles[22] or polymeric crosslinking which allows for patterning of the active layers.[23] These methods are usually material specifics and cannot be applied for a wide range of active layer materials. The absorber materials include both small molecules and polymeric semiconductor with a general characteristic of continuous conjugation. Conjugation allows for delocalisation of π electrons across the entire molecule and smoothening of charge transport by hopping or coherent transport. In practice, there are a plethora of

materials that fit the basic requirements for an absorber, with new ones appearing regularly.

Some of the more commonly used absorber materials besides P3HT include poly[2,6-(4,4-bis- (2-ethylhexyl)-4H-cyclopenta[2,1-b;3,4-b']dithiophene)-alt-4,7-(2,1,3-benzothiadiazole)] (PCPDTBT),[24] poly(9,9-didecanefluorene-alt-(bis-thienylene) benzothiadiazole) (PF10TB),[25] poly[N-9"-hepta-decanyl-2,7-carbazole-alt-5,5-(4',7'-di-2thienyl-2',1',3'-benzothiadiazole) (PCDTBT)[26] and many others. Acceptor materials on the other hand are predominantly fullerene derivatives containing C_{60} (buckyball) or C_{70}. The two most common acceptor materials are therefore $PC_{60}BM$ and $PC_{70}BM$.[10] The chemical structures of these donor and acceptor materials can be seen in Figure 3. Besides the more conventional polymer/fullerene architecture, the active layer can also be fabricated entirely from polymers.[27, 28] All-polymer solar cells are superior to polymer/fullerene architecture in three aspects: (1) a conjugated polymer is a more effective light absorber than C_{60}/C_{70} derivative in the solar radiation spectrum; (2) it is easy to tune polymer electronic structures to produce the desirable band gap and energy level alignments; (3) polymer solubility and viscosity can be tailored to allow for cheap solution-processing techniques.[29] However, all-polymer OPV suffers from low fill factor (~ 60%) due to unbalanced electron/hole mobility[29] and generally lower performance with the best certified cell reaching only 6.4% in efficiency.[30]

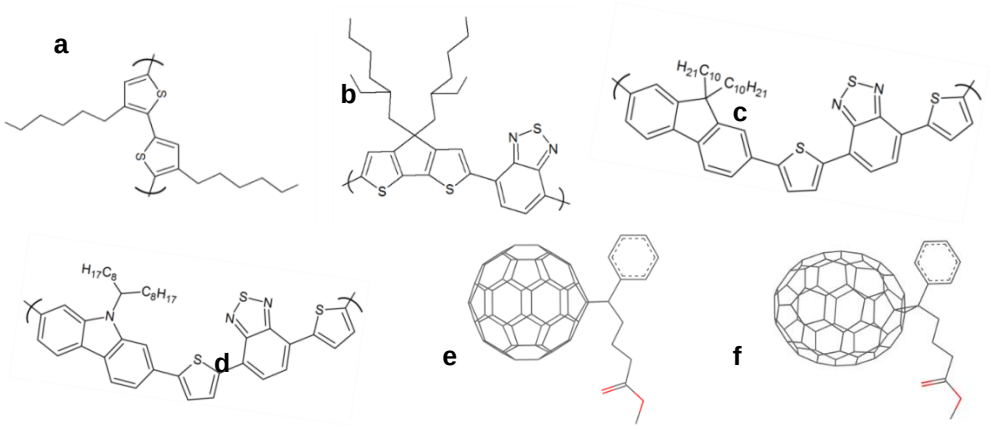

Figure 3. Chemical structure of some commonly used donor materials a) P3HT, b) PCPDTBT, c) PF10TB, d) PCDTBT and acceptor materials e) $PC_{60}BM$, f) $PC_{70}BM$.

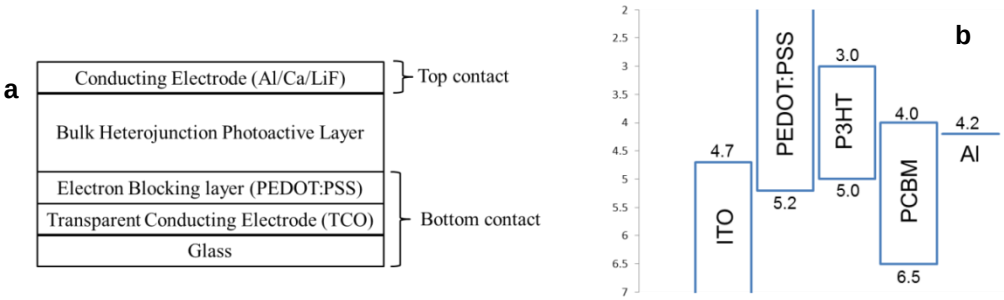

Figure 4. a) A schematic layout of a typical OPV cell. Here the incident sunlight is expected to enter the device from the bottom contact. b) Schematic diagram of the corresponding energy level of different components inside P3HT:PCBM OPV. While the mismatch in energy of Highest Occupied Molecular Orbital (HOMO) in P3HT and ITO as well as LUMO in PCBM and Al does improve charge extraction, it also reduces open-circuit voltage (V_{OC}) and, consequently, the overall efficiency

The bottom contact is conventionally defined as the side of the device where light enters the OPV, thus the primary requirement is transparency. Typically the bottom-most layer of this section is made out of glass which acts as both mechanical reinforcement as well as encapsulation or protection layer. The glass should be as transparent as possible to allow most sunlight to pass through. On top of the glass is the transparent conducting electrode or transparent conducting oxide (TCO) which injects and collects charges from the device while allowing the transmittance of sunlight. Indium Tin Oxide (ITO) is often the material of choice but its high cost has driven many researchers to search for alternatives such as gold grid, silver grid, silver nanotubes or carbon nanotubes.[31-35] Sitting right on top the TCO is a hole conducting yet electron blocking layer which is often poly(3,4-ethylenedioxythiophene)

poly(styrene sulfonate) or PEDOT:PSS. This layer is of particular importance for OPV because it enables the bulk heterojunction concept to function correctly. Without this layer, there would be indiscriminate charge collection at both the electrodes, hence, short-circuiting the device. While PEDOT:PSS is most commonly used for this purpose, efforts have been made to find suitable replacements that do not suffer from its key disadvantages of hygroscopy and acidity.[36, 37] As a result, PEDOT:PSS is known to be able to etch away the ITO layer, causing a diffusion of Indium into the OPV photoactive layer.[38] Furthermore, water stored inside the PEDOT:PSS layer also causes an increase in sheet resistance and a rapid degradation of the electron blocking layer when exposed to humid ambient conditions.[39] The typical way to mitigate this problem is inverted OPV design which brings the electron blocking layer deep into the cell, sandwiched between the photoactive layer and the top contact.[40] This reduces but does not eliminate the risk of exposing the PEDOT:PSS layer to ambient condition. Encapsulation at the bottom contact then plays a very important role in protecting the PEDOT:PSS layer. A more rigorous solution would be to replace PEDOT:PSS with a more stable hole conducting material, e.g. Molybdenum Oxide (MoO_x).[37] A schematic layout of a typical OPV cell with the bottom contact made of three distinct layers can be seen in Figure 4a.

The main photoactive layer consisting of the donor and acceptor materials in bulk heterojunction is positioned on top of the bottom contact. Beyond this layer is the top contact which is an electron extraction electrode. The top contact is made of electron conducting materials, thus, a metal or an n-type semiconductor is often used. Furthermore, the top contact should also have work function slightly larger than that of the acceptor material so that a built-in drift field can assist in electron collection without inducing too much energy loss in the form of a reduced open-circuit voltage V_{OC}. For this reason Aluminium, Calcium and Lithium Fluoride is often the material

of choice for top contacts in the system P3HT:PCBM.[41-43] An energy level diagram of Aluminium as top contact in P3HT:PCBM OPV is shown in Figure 4b.

1.2. Motivation

1.2.1. OPV Advantages

The biggest advantage of the OPV cell is the prospect for low cost photovoltaic. OPV can be manufactured by solution process technique which does not involve high vacuum or high temperature deposition processes like most silicon based solar cells. As a result, large OPV panels can be made using cheap solvent based roll-to-roll printing.[44, 45] Furthermore, due to its good absorption ability, OPV cells can be of submicron thickness (thick OPV may not work optimally due to large series resistance and carriers recombination resulting from low charge conductivity and large interfacial area respectively) so that their production require significantly less material compared to their silicon counter-part. Moreover, due to the high light absorption capability of the active materials, it is not necessary to texture the glass substrate at the bottom contact, which further drives down the manufacturing cost. In many instances, due to the flexibility of the polymeric thin film, OPV can be made into flexible devices which opens up applications in mobile devices or in conjunction with flexible OLED displays.[46] Recent achievements of exceeding 11% efficiency and proven life time lasting several years have also boosted confidence in OPV.[11, 19, 38, 47] Another very important concept to consider is the Energy Pay-Back Time (EPBT) which is defined as the amount of time needed for the device to generate and equivalent amount of energy consumed during its making and decommissioning. EPBT is approximately two to four years for inorganic photovoltaic while it can be as low as three months for OPV.[48] Production of OPV is thus more economical and environmentally friendly. On the other hand, it should also be noted that more than 90% of energy consumed is spent on the top, bottom contacts and encapsulation; out of which about 60% is spent for making and coating of TCO layer.[45, 49] Thus,

optimisation of non-photoactive layers also plays a very important role in reducing the EPBT of OPV construction. In summary, low cost materials and manufacturing techniques are the main appeal of OPV.

1.2.2. OPV Disadvantages

Despite the benefits of OPV, its share is within a humble 0.005% of the global market in 2011[49] and is expected to rise to ~ 1% in 2017.[50] With efficiencies below 8.5% for the submodules[11], it is hard to see it dominate over its competitors in the near future. The weaknesses of current OPV systems are often attributed to several factors. First, the band gap in absorber materials (donor) is typically high, for instance about 2 eV in P3HT (Figure 4b). This means that P3HT-based OPV can only absorb light with wavelength shorter than 620 nm. In practice, crystalline P3HT is known to have absorption ranges from 400 nm – 650 nm which is far from optimal because sunlight spectrum spreads from 300 nm to > 2000 nm, hence, a large portion of incoming sunlight is not utilised. In fact this is the main problem limiting the efficiency of OPV (c.f. Figure 5).[51] Efforts have been made to synthesise low band gap polymers i.e. PCPDTBT (1.4 eV), PCDTBT (1.8 eV) (ca. Figure 3) for high efficiency OPV. Following a general rule of thumb devised by Heeger et al., reduction in both donor band gap and LUMO level are the key parameters to reach efficiencies exceeding 10% on a single absorber layer OPV.[52] Second, as mentioned earlier, high binding energy of excitons prevents a spontaneous dissociation at room temperature (c.f. Figure 6).[53] While this problem is partially solved by the introduction of an acceptor material, low binding energy donor materials are always welcome since higher charge dissociations rate at donor/acceptor interface can accommodate higher LUMO level in the acceptor resulting in possible increment of V_{OC}.

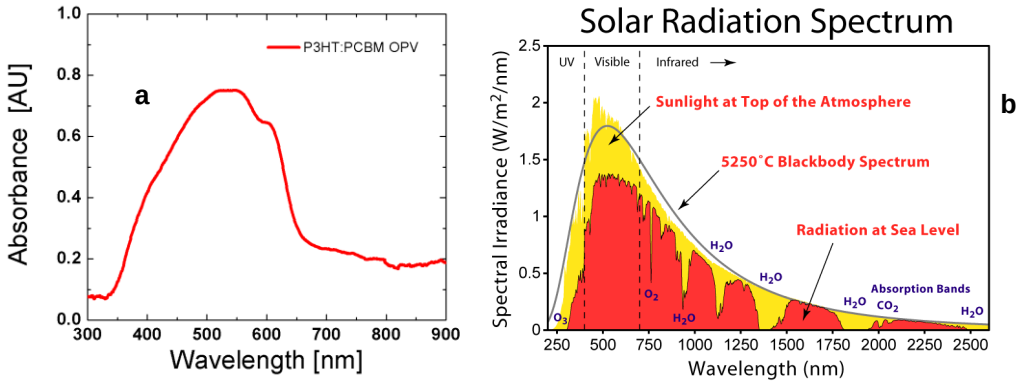

Figure 5.Comparison of a) P3HT:PCBM OPV light absorption[54] and b) the full solar spectrum[55]. This shows that the infrared regions (>750 nm) are not absorbed by OPV, hence, limiting the achievable efficiency.

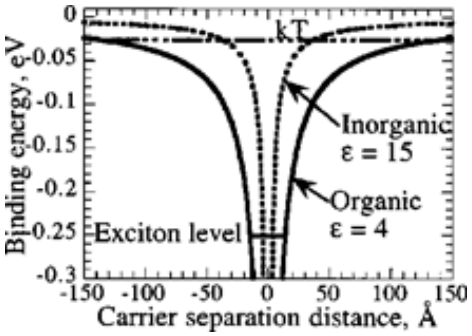

Figure 6. Comparison of excitons binding energy in organic ($\boldsymbol{\varepsilon = 4}$) and inorganic ($\boldsymbol{\varepsilon = 15}$) semiconductor shows excitons in organic materials are bound over a much larger distance. Adapted from [37].

Third, in contrast to their inorganic counterpart, polymeric semiconductors suffer from inefficient charge transport which is evident in the low charge mobility. While silicon could reach > 1000 $cm^2V^{-1}s^{-1}$, typical charge carrier mobility in polymeric conductors is up to the order of 10^{-1} $cm^2V^{-1}s^{-1}$, only. It was demonstrated that with an optimised heat treatment, improved crystallinity leads to an order of magnitude higher mobility and, as a result, a 400% increase in efficiency.[9, 56, 57] Last but not least, the small diffusion length of excitons, which is estimated to be about 10nm, means that large donor domains/crystallites are undesirable. On the other hand, following Heeger et al.'s argument using uncertainty principle, donor domain size should be approximately 20 nm for ultra-fast excitons dissociations to be possible.[21] It was reported that long annealing time leading to large crystallites often results in reduced performance while charge transport efficiency is improved.[58] Furthermore, careful control of morphology to provide bicontinuous bulk heterojunction is needed for optimal charge extraction. Isolated phases often lead to bimolecular recombinations which further induce a drop in V_{OC}.[8, 59] In summary, low efficiency caused by undesirable light absorption spectrum, high binding energy, low charge

mobility and exciton diffusion lengths are preventing OPV from achieving a higher market share.

1.2.3. The Need for a Deeper Theoretical Understanding

While most OPV problems are reported in literature, tackling them proves to be a challenge due to a lack of firm understanding in the device physics. For instance, there are many contradicting views on the origin of morphology evolution in P3HT:PCBM bulk heterojunction. While at the beginning of this project it was commonly assumed that phase separation during annealing is caused by a miscibility gap[60]; more recently there are growing indications (also from this work) that amorphous P3HT and PCBM are perfectly miscible but their crystalline phases are not, thus crystallisation is the driving force for phase separation.[9, 61] Furthermore, recent study suggested that the bicontinuous bulk heterojunction as the optimal morphology may not be experimentally feasible due to the observed multi-phased active layer morphology (i.e. crystalline donor phase, crystalline acceptor phase and mixed donor:acceptor phase).[62-64] Moreover, the theoretical framework for describing charge transport in organic semiconductor is also in need of more insightful research. The currently available theories can be used to explain certain observations; for instance the drop in charge mobility when the operating temperature is raised could be captured in a model of by Troisi and Orlandi.[65] Still, the model is only applicable to highly crystalline small molecule organic semiconductor, hence not conclusive for high molecular mass polymeric materials. One of the inherent difficulties in deriving a suitable model for conjugated polymeric semiconductors is the strong dependence of transport properties on molecular arrangements which is evident in the drastic difference of mobility in crystalline and amorphous regions. On the other hand, it proves challenging to capture the effects of chemical structures on physical properties in the framework of current models; which would be essential for a systematic molecule design for high performance OPV. The lack of a more complete

understanding in bulk heterojunction morphology and charge transport is thus one of the major areas that need to be addressed to speed up the progress in OPV research.

Moreover, it is important to have a continuous model spanning from molecular ab-initio all the way to device level simulation. This will help to connect the microscopic properties, which can be more faithfully simulated without or with minimal input from experiment, to macroscopic properties which are relevant in aiding experimental and OPV device architecture design. Such a framework would also help in pinpointing the influence of quantum behaviour on the overall device performance. The lack of a bridging framework means that current atomistic model cannot perform device relevant scale simulations while continuum models are usually based on inorganic solar cell theory, which has limited applicability to OPV.

1.2.4.Research Statement

In this work, we aim to complete three tasks:

1. Create new tools that would aid in elucidating the physical and chemical properties underlying the morphology evolution and charge transport process of OPV active layer at atomistic and device level. These tools are coarse-grained MD and first-principles charge transport model.

2. Use the developed tools to understand the underlying principles of morphology evolution and charge transport phenomenon in the active layer. We also seek to correlate the active layer morphology and charge transport behaviour which is critical to the device performance.

3. Bridge the gap between atomistic and continuum level simulations so that a continuous theoretical framework can be developed which is important in aiding both molecular and experimental design. The device-level MC simulations conducted in chapter 2.4 using the interfacial energy data

abstracted from the coarse-grained MD simulations in chapter 2.3 may serve as a first demonstration example.

Completing the three tasks laid out above would help in promoting the fundamental and theoretical understanding of the active layer in P3HT:PCBM based OPV focusing especially on morphological aspects and the possible ramifications of morphology on charge transport and light absorption. To this end, simulation tools such as empirical Molecular Dynamics (MD), ab-initio Density Functional Theory (DFT), extended Hückel orbital calculation method and Marcus electron transport theory were employed. For morphology studies, atomistic MD is first utilized which is most accurate down to atomic scale, shedding light on important parameters such as relative atomic arrangements and orientations which are critical to charge transport and other nanometre-scale effects. However, detailed MD could not hope to cover device-level dimension and the experimental time scale of morphology evolution due to the shear computational cost. Simulations were then scaled up by establishing and utilizing a coarse-grained MD scheme, which we found to speed up calculations about 200 times (c.f. Section 2.3.4). With the aid of coarse-graining, we studied P3HT:PCBM interfaces at domain size similar to reported experimental data allowing us to identify the most stable configurations relevant for further charge transport studies. To further bridge of the gap between MD simulations and experiments in term of both time and dimension we employed Monte Carlo (MC) simulation to shed light on the possible resultant P3HT:PCBM phase-separated morphology based on the parameters calculated from MD and reported experimental data. MC simulations results can then provide the input to continuum models for rapid computation of current-voltage behaviour as a function of bulk-heterojunction morphology in a separate project.

The effect of morphology on charge transport is studied by first considering a simple first-principles formulation based on the framework of extended Hückel method and

Marcus electron theory for the study of charge transport and light absorption in conjugated systems. The formulation is then extended to include inter-molecular charge hopping within the donor materials phase which can then be generalized for both donor and acceptor. This allows robust calculations of transport in the active layers by invoking the active layer Hamiltonian which incorporates geometric parameters at the interface as well as within individual domains and electronic information (HOMO/LUMO energy level and coupling energy). Geometric parameters and electronic information are obtained using DFT techniques and both MD, coarse-grained MD respectively. At the current stage, the model is limited to 1-D bilayer case. Nevertheless, it gave valuable information into molecular design for optimal transport performance.

Our calculations focused on P3HT:PCBM system due to two reasons. First, this has been the most widely studied bulk heterojunction system; hence many experimental data are readily available for comparison and validation of computational results.[10] Second, in our lab, P3HT:PCBM cells were proven to be stable and easily made from cheap solution processing techniques while maintaining decent reproducible efficiencies of > 3%.[66] Even though the direct applicability of the results presented in this work may appear limited to P3HT:PCBM OPV, the framework can be utilized to treat morphology evolution and charge transport in other OPV photoactive materials as well as in organic semiconductors in general.

CHAPTER 2: Morphological Modelling

2.1. Literature Review

As mentioned above, morphology layout of the bulk heterojunction is often discussed as one of the most important factors influencing the device performance. While it is widely assumed that a bicontinuous layout is most desirable for both charge dissociation and charge transport, an effective scheme towards achieving such is still not known,[59] since the mechanism driving morphology evolution is still a topic of scientific debate. Even though some maintain a thermodynamic model assuming a miscibility gap-driven morphology evolution, there is growing evidence that the kinetics of phase change from amorphous to crystalline P3HT might be the main driving force. In this section we will look at the most prominent morphology evolution models of P3HT:PCBM obtained from experimental observations.

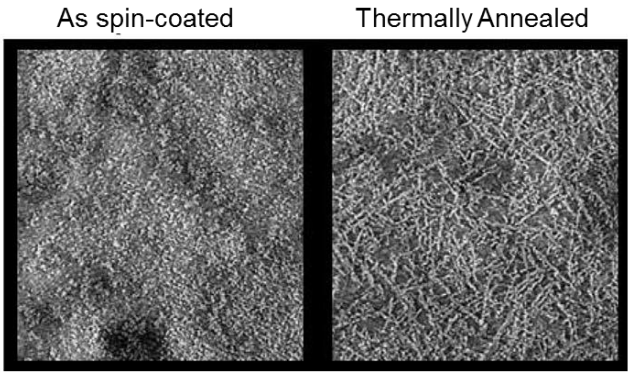

Bavel, S. S. v.; Sourty, E.; With, G. d.; Loos, J. *Nano Lett.* **2008,** 9, (2), 507-513.

Figure 7.TEM image showing the effect of annealing on P3HT:PCBM bulk heterojunction morphology. Thermal treatment of as little as a few minutes could lead to substantial phase separations.[67]

Ever since the introduction of bulk heterojunction concept in 1995, much research interest has been placed on the morphology evolution of donor/acceptor blends in OPV. The most typical way to study this is to deposit donor:acceptor blends from solutions and to monitor phase separation (most commonly by heat treatment) into the bulk heterojunction structure via a variety of established characterisation

techniques such as Transmission Electron Microscopy (TEM), Scanning Electron Microscope (SEM), Scanning Probe Microscopy (SPM), Atomic Force Microscopy (AFM), Electron Tomography (ET) and so on.[59] Most studies agree that upon annealing of an P3HT:PCBM blend at ~150°C, phase separation occurs (ca. Figure 7).[56, 67-70] Furthermore, diffraction patterns reveal the formation of crystalline P3HT after thermal treatment, which is also evident from the characteristic shoulder at 600 nm in the light absorption spectrum.[67, 71] These findings led to the spinodal decomposition model as the main phase separation mechanism in P3HT:PCBM, which, to a certain extent, harmonizes with experimental and simulation findings that about 20% of PCBM remains in the P3HT matrix forming donor rich regions.[58, 63, 72, 73] While bulk heterojunction morphology has been widely modelled in the frame of the miscibility gap picture, recent reports suggested that an alternative mechanism should be considered. By performing Dynamic Secondary Ion Mass Spectrometry (DSIMS) on a P3HT:deuterated PCBM (d-PCBM) bilayer thermally treated at different temperatures, Treat et al. (2011) demonstrated that PCBM can readily diffuse into P3HT at temperatures as low as 70°C and that it is very mobile within a P3HT matrix. Furthermore, by employing X-ray Scattering in Grazing Incidence Geometry (GIWAXS), they were able to observe morphology evolution of P3HT:d-PCBM during annealing process in real time. The study revealed that there are little to no perturbations of lattice parameters of the crystalline regions within P3HT during the diffusion process of d-PCBM into P3HT, which suggested that the amorphous regions in P3HT are the preferred media for PCBM diffusion.[61] Elsewhere, Chen et al. (2011) reported a similar finding by using Grazing Incidence Small-Angle X-ray Scattering (GISAXS) and Resonant Soft X-ray Scattering (RSoXS) also on a bilayer P3HT:PCBM confirming that P3HT crystallite sizes remain largely unchanged after the annealing process.[74] In a more recent publication Steiner et al. (2013) concluded on the basis of UV-vis and X-ray measurements that the miscibility limit of PCBM in P3HT corresponds to a weight ratio of about 2:1 in amorphous P3HT or 1:2 in

partially crystalline P3HT (regioregular P3HT with 50-70% crystallinity) and no spinodal demixing should occur during annealing.[75]

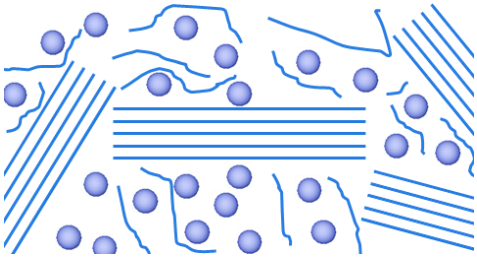

Figure 8. Schematic diagram of suggested P3HT:PCBM bulk heterojunction morphology consisting of pure crystalline P3HT, mixture of amorphousP3HT:PCBM and PCBM aggregate consistent with recent experimental observations.

On the basis of these findings, it appears reasonable to conjecture that while amorphous P3HT and PCBM are completely miscible in each other, their crystalline phases are not. This new line of thought was proposed and supported with various experimental details by Wu (2011).[9] With a combination of GIWAXS measurements on P3HT:PCBM bulk heterojunction and their analysis in terms of the Avrami-Erofeev formula(also called Johnson-Mehl-Avrami-Kolmogorov equation), it was demonstrated that the Avrami rate constant of P3HT crystallisation in P3HT:PCBM bulk heterojunction was four times lower than that of pristine P3HT implying that the presence of PCBM restrict the formation of P3HT crystallites. Furthermore, the high Avrami rate constant, low activation energy for PCBM aggregate, high activation energy for P3HT crystal formation and strong correlation between PCBM aggregation and P3HT crystallisation suggest that nucleation and crystallisation of P3HT is the primary driving force towards phase separation to form P3HT:PCBM bulk heterojunction.[9] While this experimental evidence infers that annealed P3HT:PCBM bulk heterojunction is made up of P3HT crystalline phase, amorphous P3HT:PCBM phase and PCBM aggregate (c.f. Figure 8) it still leaves many morphology-relevant questions unanswered including but not limited to for instance: How do P3HT and PCBM molecules align themselves at the interface? What is the preferred pathway for PCBM to segregate from the bulk heterojunction? Is there a

preferred orientation/structure for the presumed disordered P3HT:PCBM phase and PCBM aggregate? What are the roles of side chains in diffusion and phase separations?

To complement experimental approaches, theoretical studies have been undertaken to reveal more details of the morphology evolution mechanism. Cheung et al. (2009, 2010) employed MD using a forcefield that combined parameters for PCBM from the OPLS (Optimised Potentials for Liquid Simulations)[76] forcefield with parameters for P3HT from the Marcon and Raos (MR)[77] forcefield, to study atomistic arrangements of pure P3HT and pure PCBM, which were then used for first-principles charge transport studies.[78, 79] Huang et al. (2009, 2011) applied coarse-graining method on P3HT and C_{60} forcefield to reduce computational effort. Their morphology study of the P3HT:C_{60} bulk heterojunction at 650K shows phase separation and the formation of C_{60} clusters after just 135 ns.[80, 81] Similarly, Frigerio (2012) performed MD analysis on PCBM structure in oDCB (ortho-dichlorobenzene) and MCB (monochlorobenzene) from which the author concluded that fullerene clusters formed from MCB solutions assume structures more favourable for charge transport.[82] Alternative to atomistic approach, mesoscale modelling approach by Xue et al. (2012) suggested that a P3HT:PCBM composition ratio of 1:1, high annealing temperature and Flory-Huggins parameter $\chi > 1$ are required to yield the desirable bicontinuous highly phase-separated P3HT:PCBM bulk heterojunction.[83] This result is in line with coarse-grained modelling reported by Lee et al.[84]

In this thesis, morphological modelling starts with benchmarking the atomistic forcefield with ab-initio DFT calculations to improve the forcefield accuracy. A coarse-grained forcefield is then developed based on the atomistic one in order to study P3HT:PCBM interface at scale larger than typically observed domain sizes. From this analysis, an interfacial energy profile was computed and became the basis

of Monte Carlo (MC) simulation which allows us to simulate systems of comparable size to experimental OPV devices.

2.2. Atomistic Modelling

2.2.1. Primer on MD and DFT Simulation Techniques

2.2.1.1. Molecular Dynamics (MD) Method

Before delving into the details of this work, we will first discuss the basics behind MD and DFT simulation techniques as the primary tools for studying of P3HT:PCBM bulk heterojunction morphology. MD method is a classical method based on deterministic Newtonian mechanics. In this framework, atomic trajectories are determined by initial conditions (position and momentum) and inter-atomic interaction rules called forcefield. There are many types of forcefields which differ in functional forms, hence, are applicable to different class of materials; for instance Embedded Atom Model (EAM) or Tersoff forcefields are used mainly for metals or silicon respectively.[85, 86] In this work, however, we will be adopting a 'first generation' functional form which is widely used to model organic materials.[78] The 'first generation' forcefield consists of Lennard Jones potential as Van der Waals (VdW) interaction, Coulomb interaction, harmonic functional representing bond angle and bond stretching effects and dihedral potential for torsional behaviours. Cross terms are neglected. The detail functional form can be seen in Equation (3.1). where k_{bonds} and k_{angle} are the bond stretching and angle bend coefficients; r and θ are the bond length and bond angle; r_0 and θ_0 are the equilibrium bond length and bond angle; φ is the torsion angle; V_1, V_2, V_3 and V_4 are the torsion parameters; q_i is the Coulomb charge of atom i; r_{ij} is the distance between atom i and atom j; σ_{ij} is the equilibrium VdW bond distance between atom i and atom j; ϵ_{ij} is the VdW bond strength between atom i and atom j.

$$V = \sum_{bonds} \frac{1}{2} k_{bonds}(r - r_0)^2 + \sum_{angles} \frac{1}{2} k_{angle}(\theta - \theta_0)^2 + \sum_{torsions} \frac{1}{2}\big(V_1(1 + \cos\varphi) + V_2(1 - \cos 2\varphi) + V_3(1 + \cos 3\varphi) + V_4(1 - \cos 4\varphi)\big) + \sum_{Coloumb}^{i<j} \frac{q_i q_j}{r_{ij}} + \sum_{VDW}^{i<j} \left\{ +4\epsilon_{ij} \left[\left(\frac{\sigma_{ij}}{r_{ij}}\right)^{12} - \left(\frac{\sigma_{ij}}{r_{ij}}\right)^{6} \right] \right\} \quad (3.1)$$

The forcefield enables us to compute the potential energy of the system when atomic positions and related parameters are given. However, trajectory calculations require us to include the kinetic energy terms and invoke Euler-Lagrangian that seeks to minimise the Lagrangian of the system (Equation (3.2)).

$$\frac{d}{dt}\left(\frac{\partial L}{\partial p_i'}\right) = \frac{\partial L}{\partial p_i} \quad (3.2)$$

Here L is the Lagrangian, which is the kinetic energy subtracting away the potential energy, and p_i is the momentum of particle i. Although the formulae for both potential energy and kinetic energy are straightforward to evaluate, it becomes more complicated when periodic boundary condition are considered, in which case long range interactions like Coulomb or VdW interactions should be performed over extended distances, hence, raising computational cost. Nevertheless, MD simulations with periodic boundary conditions are often used to study bulk properties using Ewald summation to improve both efficiency and accuracy.[87] In Ewald summation, divergent summations required for long range interaction are split into two terms that converge in the real space and the reciprocal space respectively. This was done by first rewriting the energy summation of the long term interactions (c.f. Equation (3.3)).

$$S_m = \frac{1}{2}\sum_{L,i,j}\frac{A_{i,j}}{\left|\mathbf{r}_i - \mathbf{r}_j - \mathbf{R}_L\right|^m} = \frac{1}{2}\sum_{i,j}\frac{A_{i,j}\phi_m\left(\left|\mathbf{r}_i - \mathbf{r}_j - \mathbf{R}_L\right|\right)}{\left|\mathbf{r}_i - \mathbf{r}_j - \mathbf{R}_L\right|^m} + \frac{1}{2}\sum_{i,j}\frac{A_{i,j}\left[1 - \phi_m\left(\left|\mathbf{r}_i - \mathbf{r}_j - \mathbf{R}_L\right|\right)\right]}{\left|\mathbf{r}_i - \mathbf{r}_j - \mathbf{R}_L\right|^m} \quad (3.3)$$

where

$$\phi_m(r) = \frac{1}{\Gamma\left(\frac{m}{2}\right)}\int_{\frac{r^2}{\eta^2}}^{\infty} t^{\frac{m}{2}-1}\exp(-t)\,dt \quad (3.4)$$

In Equation (3.3) $A_{i,j}$ is a constant associated with long-range interaction between atom i and j; $\mathbf{r}_i$ ($\mathbf{r}_j$) is the position vector of atom $i(j)$; $\mathbf{R}_L$ is the lattice translation vector; ϕ_m is defined in Equation (3.4) and m determines the type of long range interaction with $m = 1$ and $m = 6$ or 12 for Coulomb and VdW interactions, respectively. For Coulomb interactions of a charge neutral system, Equation (3.4) and (3.3) becomes.

$$\phi_1(r) = \mathrm{erfc}(r/\eta) = 1 - \mathrm{erf}(r/\eta) \quad (3.5)$$

$$S_1 = \frac{1}{2}\sum_{L,i,j} q_i q_j \frac{\mathrm{erfc}(a)}{a} + \frac{2\pi}{\Omega}\sum_{\mathbf{h}}\left\{\sum_{i,j} q_i q_j \cos\left[\mathbf{h}\cdot\left(\mathbf{r}_i - \mathbf{r}_j\right)\right]\right\} h^{-2} e^{-b^2} - \frac{1}{\eta\sqrt{\pi}}\left(\sum_i q_i q_i\right) \quad (3.6)$$

where q_i is the charge of atom i; Ω is the volume of the unit cell; $\mathbf{h}$ is the lattice vector of the reciprocal lattice; $a = \left|\mathbf{r}_i - \mathbf{r}_j - \mathbf{R}_L\right|/\eta$, $b = \frac{1}{2}h\eta$, $h = |\mathbf{h}|$; η is an arbitrary constant which determines how fast the summations would converge in real space and in reciprocal space (the first and second summations in Equation (3.6) respectively). As η increases, the real-space sum converges more rapidly and the reciprocal space sum converges more slowly (that is, a large η implies a heavy computational load for reciprocal space, and a small η implies a heavy computational

load for real space). In our work, η was chosen such that the Ewald summation would amount to an uncertainty of $\pm 4 \times 10^{-5}$ eV for each unit cell. The same formulation can be extended for VdW calculations by changing the value of m. A more in-depth analysis of Ewald summations for all long range interactions can be found elsewhere.[87]

Another problem in MD is the control of pressure and temperature (commonly known as barostat and thermostat). Since analysis of system evolution is only meaningful if the state it is in, which means temperature and pressure, is known. If these parameters are left unchecked, system may escalate out of hand and obtained results are not reliable. One typical way of controlling temperature and pressure is attaching a pressure bath and heat bath to the system. We can then define the coupling strength between the baths and the system; this corresponds to how much influence ambient conditions have on the dynamics of the system. In the relatively simple Berendsen method, the position and velocity of each atom in the system are slightly adjusted after each iteration in order to reduce the difference between the instantaneous pressure/temperature and the ambient pressure/temperature and the coupling strength. In contrast to an instantaneous scaling of the particle velocities that would lead to clear deviations from thermodynamic ensembles (e.g. in terms of the Maxwell-Boltzmann velocity distribution) such a slight biasing of the velocities is known to result in only negligible deviations from equilibrium thermodynamics, while at the same time reducing computational effort significantly when compared to alternative thermostats (such as the Nosé-Hoover thermostat) that are strictly in line with thermodynamics.[88]

2.2.1.2. Density Functional Theory (DFT) Method

The accuracy in MD simulations depends heavily on the quality of the forcefield. In fact most forcefields are empirical since their parameters are engineered so that

certain experimental features can be reproduced. Thus, in order to validate the forcefield, we employ a more accurate and reliable technique, i.e. DFT. Contrary to MD method, DFT is an ab-initio technique employing quantum mechanics formulation which boils down to solving Schrödinger's equation (c.f. Equation (3.9)) which requires only the atomic numbers and coordinates of the atoms involved as inputs.

$$H\psi = \left[\sum_i \frac{-\hbar^2}{2m_i}\nabla^2 + \sum_i V(\mathbf{r}_i) + \sum_{i<j} U(\mathbf{r}_i, \mathbf{r}_j)\right]\psi = E\psi \tag{3.9}$$

Here H is the Hamiltonian of the system, i.e. the sum of both kinetic and potential energy; ψ is the wavefunction; m_i is the mass of particle i; $V(\mathbf{r}_i)$ is the potential energy of particle i; $U(\mathbf{r}_i, \mathbf{r}_j)$ represents the interaction of particle i and j; and E is the energy of the system. Since ψ is preserved on both sides of the equation, this is often referred to as the eigenfunction problem. However, in order to solve the Schrödinger's equation, the Born–Oppenheimer approximation needs to be considered. In this scheme, the wavefunction of the nuclei and electrons are decoupled due to the fact that nuclei are a lot heavier than electrons (Equation (3.10)). This means that electrons are modelled to respond instantaneously to the potential of the nuclei without affecting their states.

$$\Psi(\mathbf{R}_1, \mathbf{R}_1, \ldots \mathbf{R}_N, \mathbf{r}_1, \mathbf{r}_n \ldots) = \Phi(\mathbf{R}_1, \mathbf{R}_1, \ldots \mathbf{R}_N)\, \psi(\mathbf{r}_1, \mathbf{r}_n \ldots) \tag{3.10}$$

By applying variational theory, Hohenberg-Kohn existence theory[89] imposes that there is an isomorphic relation between the ground state electron density function and the Hamiltonian. To prove this, assume that for electron density function $\rho(\mathbf{r})$ we could find two different Hamiltonians potential field $\hat{V}$ and $\hat{V}'$ which correspond to H and H' with two ground-states $|\psi\rangle$ and $|\psi'\rangle$. We would then have:

$$E_0 = \langle\psi|H|\psi\rangle$$

and

$$E'_0 = \langle\psi'|H'|\psi'\rangle$$

According to variational theory:

$$E_0 < \langle \psi' | H | \psi' \rangle = \langle \psi' | H' | \psi' \rangle + \langle \psi' | H - H' | \psi' \rangle$$

Since the ground state density is common to all Hamiltonians:

$$\langle \psi' | H - H' | \psi' \rangle = \int \rho(\mathbf{r}) \left[\hat{V} - \widehat{V'} \right] d\boldsymbol{r}$$

Thus $$E_0 < E'_0 + \int \rho(\mathbf{r}) \left[\hat{V} - \widehat{V'} \right] d\mathbf{r} \qquad \text{I}$$

Similarly $$E'_0 < \langle \psi | H' | \psi \rangle = \langle \psi | H | \psi \rangle + \langle \psi | H' - H | \psi \rangle$$

$$\langle \psi | H' - H | \psi \rangle = - \int \rho(\mathbf{r}) \left[\hat{V} - \widehat{V'} \right] d\mathbf{r}$$

$$\Rightarrow E'_0 < E_0 - \int \rho(\mathbf{r}) \left[\hat{V} - \widehat{V'} \right] d\mathbf{r} \qquad \text{II}$$

Combine I and II:

$$E_0 + E'_0 < E'_0 + E_0$$

This is a contradiction. Thus $\rho(\mathbf{r})$ determines $\hat{V}$ and in turn the Hamiltonians and other physical observables. It is also conclusive that knowing $\rho(\mathbf{r})$ is sufficient to characterise the system. By applying this, in DFT method, we need to solve Kohn-Sham's Schrödinger equation instead (c.f. Equation (3.11)).[90]

$$\left[-\frac{1}{2} \nabla_i^2 + \hat{V}_{eff}(\mathbf{r}) \right] \varphi_i^{KS}(\mathbf{r}) = \epsilon_i \varphi_i^{KS}(\mathbf{r}) \qquad (3.11)$$

In this equation φ_i^{KS} is the Kohn-Sham orbital which holds no true physical meaning but is directly related to the electron density function (c.f. Equation (3.12)). And $\hat{V}_{eff}(r)$ is the potential energy which contains all other interactions (c.f. Equation (3.13)). The essence of Kohn-Sham's Schrödinger equation lies in the first term of Equation (3.11) which is defined as the kinetic energy of non-interacting electrons. This means that all electron-electron, and electron-nucleus interactions including coupling is reserved for $\hat{V}_{eff}(\mathbf{r})$.

$$\rho(\mathbf{r}) = \sum_{i=1}^{N} \left|\varphi_i^{KS}(\mathbf{r})\right|^2 \tag{3.12}$$

$$\hat{V}_{eff}(\mathbf{r}) = \hat{V}_{ext}(\mathbf{r}) + \hat{U}_{el}(\mathbf{r}) + \hat{V}_{xc}(\mathbf{r}) \tag{3.13}$$

where $\hat{U}_{el}(\mathbf{r})$ is the Coulomb repulsion between electrons.

$$\hat{U}_{el}(\mathbf{r}) = \int \frac{\rho(\mathbf{r})}{|\mathbf{r}' - \mathbf{r}|} d\mathbf{r}$$

and $\hat{V}_{ext}(\mathbf{r})$ is the potential caused by nuclei.

$$\hat{V}_{ext}(\mathbf{r}) = \sum_{a} \frac{-Z_a}{|\mathbf{R}_a - \mathbf{r}|}$$

The most complicated term in Equation (3.13) is the exchange-correlation $\hat{V}_{xc}(r)$ which represents coupling between electrons. $\hat{V}_{xc}(r)$ is often described as a sum of the exchange and the correlation potentials; unfortunately, the exact forms for both are not known. In fact, much research and development in DFT to a large extent revolves around optimising and comparing ways of approximating $\hat{V}_{xc}(r)$. In this work, however, we will adopt Projector Augmented Wave (PAW) pseudopotentials[91] and Perdew-Burke-Ernzerhof (PBE) functional[92] for both exchange and correlation component of $\hat{V}_{xc}(r)$ for all DFT calculations unless otherwise stated. This is because it is one of the more computationally efficient recent methods that were proven to produce relatively accurate results, especially in regard to geometry.[93] A more in depth discussion of DFT is available elsewhere.[94]

2.2.2.Forcefield Benchmarking against First-Principles Method

In this work, forcefield parameters for both P3HT and PCBM have not been derived from scratch. Instead we will start by validating the P3HT and PCBM forcefields reported by Marcon and Raos and later modified by Cheung et al. (2009, 2010) (MRC).[77-79] Validation was done in this project using DFT method with PBE functional; all DFT calculations were done using VASP code.[95]

2.2.2.1. PCBM Forcefield

For PCBM, we adopted the reported forcefield from Cheung et al.[79] who developed the forcefield based on the OPLS forcefield[76], with equilibrium bond lengths obtained from electron diffraction data.[96] The forcefield was later validated by Frigerio et al.[82] by comparison of lattice parameters of PCBM crystallised in oDCB at different annealing temperatures from 90 K to 400 K. To further validate this forcefield, we adopted crystal structure of PCBM in oDCB solvent as reported by Rispens et al.[97] The solvent-removed structure then underwent structure optimisation using ab-initio DFT with cut-off energy of 400 eV. The optimised structure further underwent geometric optimisation, this time, using MD method with the adopted forcefield; after which, it was allowed to relax at 300 K and 1 atm under constant temperature and constant pressure condition (NPT). The forcefield geometry-optimised structure and the NPT simulation results are benchmarked against the DFT optimised structure for validation of the forcefield. The resulting lattice parameters of all the runs are shown in Table 1, from which it is evident that there is not much variation between ab-initio DFT result and MD simulation runs. On the basis of benchmarking against DFT calculation and experimental result (as reported in literature), we claim that the adopted PCBM is validated.

Lattice Parameters	Experimental PCBM (in oDCB)[97]	DFT optimised PCBM	Atomistically optimised PCBM	NPT MD simulation of PCBM at 300K
a	13.76 Å	13.94 Å	13.67 Å ***(-1.9%)***	13.69 Å ***(-1.8%)***
b	16.64 Å	16.87 Å	17.08 Å ***(+1.2%)***	17.10 Å ***(+1.3%)***
c	19.08 Å	19.38 Å	19.40 Å ***(+0.1%)***	19.10 Å ***(-1.4%)***
α	90.0°	90.0°	90.0° ***(-%)***	90.0° ***(-%)***
β	105.3°	105.4°	108.8° ***(+3.1%)***	108.8° ***(+3.1%)***
γ	90.0°	90.0°	90.00° ***(-%)***	90.00° ***(-%)***

Table 1. Comparison of lattice parameters obtained for PCBM using different methods. Here the DFT result serves as a benchmark for geometry optimisation and MD simulation using the adopted PCBM forcefield. The percentages given in the close bracket on the last two columns on the right indicate the difference between the respective value and the corresponding result from DFT calculation. Close agreement between DFT and MD structures (after both geometry optimisation and molecular dynamics runs) validate the PCBM atomistic forcefield.

2.2.2.2. P3HT Forcefield[98]

Unlike for PCBM, the reported MRC forcefield for P3HT does not agree well with DFT calculations in terms of energy evolution of torsion angle between neighbouring thiophene rings. For a mere (i.e. repeating unit) of 2 thiophene rings, the MRC forcefield shows a single local minimum at 90°, which effectively is the most unstable configuration according to DFT calculation. Accordingly DFT suggests 2 local minima at 50° and 180° with the one at 180° being the most stable (c.f. Figure 9a). This trend persists when the molecular weight (M_W) of P3HT molecule increases: for a P3HT molecule of 8 thiophene rings again the MRC forcefield shows lowest energy point at 90° (c.f. Figure 9b). Since our DFT result agrees with other reported ab-initio calculations of P3HT molecules of up to 28 thiophene rings which employed B3LYP functional and 3-21G* basis set[99] (c.f. Appendix A), we concluded that the MRC forcefield is not accurate in description of torsion angle between neighbouring thiophene rings. Here our results for P3HT molecules focus on the alternate rotation

setting which gives a lower energy configuration at the global minimum when compared to the continuous rotation mode (c.f. Figure 10).

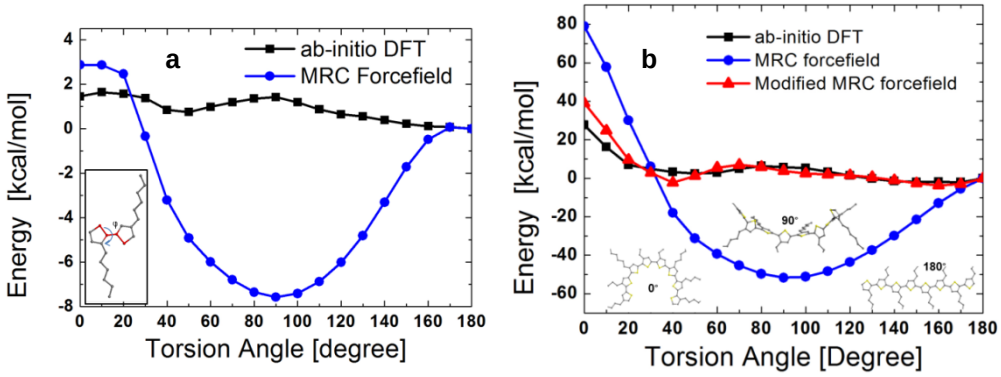

Figure 9. a) Energy changes of a 2 thiophene rings P3HT system as a function of torsion angle between the rings. Result computed from MRC forcefield shows most stable configuration at 90° which differs from our DFT benchmark that suggests 180° as the lowest energy configuration. Inset shows P3HT System of 2 thiophene rings with red part highlights the torsion angle 'φ'. Hydrogen atoms are omitted for clarity. b) Energy changes of P3HT molecule with 8 thiophene rings shows good agreement between the modified MRC forcefield using our new torsion parameters. Inset shows P3HT molecules configuration at different torsion angles.

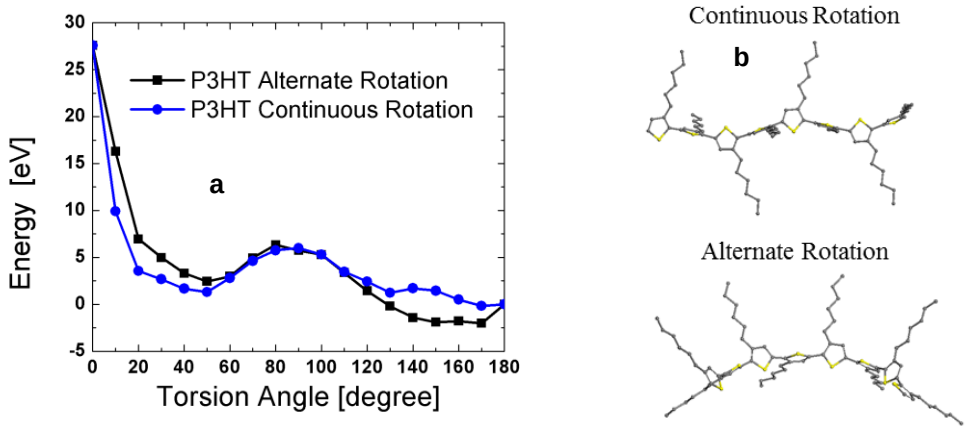

Figure 10. a) Energy changes of a P3HT molecule with 8 thiophene rings as a function of torsion angle. Here two modes of rotations namely alternate and continuous are compared. The difference between these two modes at 90° can be seen in (b). Since the global minimum of alternate rotation is more stable, and is more likely to manifest itself in actual P3HT compound, alternate rotation was used for torsion parameters fitting.

To make MD simulation consistent with DFT results, we modified the S-C-C-S torsion parameter (highlighted in red in Figure 9a) which bridges two thiophene rings in the forcefield. This change was done by least square fitting such that the overall energy variation as a function of torsion angle would be comparable to that of DFT

result (c.f. Figure 9b). This new torsion terms correspond to S11-C1-C1-S11 in the forcefield (c.f. Appendix A) and can be seen in Table 2. The complete forcefield is available for reference in Appendix A.

i	**j**	**k**	**l**	$\boldsymbol{V_1}$(kcal·mol^{-1})	$\boldsymbol{V_2}$(kcal·mol^{-1})	$\boldsymbol{V_3}$(kcal·mol^{-1})	$\boldsymbol{V_4}$(kcal·mol^{-1})
S11	C1	C1	S11	3.9697	9.1853	1.7845	2.4383

Table 2. New torsion parameters used in our modified MRC forcefield. With this, description of torsion angle agrees well with DFT result for P3HT molecules of 8 thiophene rings (c.f. Figure 9b).

With the new torsion terms, P3HT structures optimised using the modified forcefield show optimal configuration of planar neighbouring thiophene rings with side chains in trans position in good agreement with DFT calculations unlike the MRC forcefield which results in neighbouring rings oriented perpendicular to each other (c.f. Figure 11).

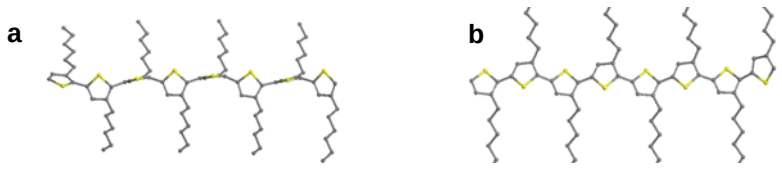

Figure 11. Optimised structures of P3HT molecule of 8 thiophene rings as calculated by a) MRC forcefield and b) our modified forcefield. While our modified forcefield was able to reproduce DFT results with the trans configuration as the most preferred, MRC forcefield relaxed to 90° torsion configuration which was highly unstable according DFT results. Hydrogen atoms are not show for clarity.

Further validation of the modified forcefield was done by benchmarking against experimentally available data. First we compared simulated densities of crystalline P3HT as computed by both the original forcefield and the modified forcefield with the experimentally reported value of 1.10±0.05 g/cm^3 (c.f. Table 3).[100] The simulated result was obtained at room temperature (300K) and atmospheric pressure (1atm) with NPT ensemble to replicate experimental condition. For all MD simulations, P3HT crystal assumed non-interdigitated and staggered form as determined from single crystal X-ray diffraction data by Brinkmann et al.[101] This structure has also been widely reported in literature from both experimental and theoretical studies.[102-104] Each crystalline P3HT unit cell consisted of 18 molecules with identical M_W.

Different systems with M_W varying from 3,320 to 26,560 were simulated to capture the effect of different M_W. From the results obtained, it is evident that the modified forcefield shows closer agreement with experimental data than the MRC forcefield, which consistently gives lower density than expected for P3HT Brinkmann's crystal structure regardless of M_W. This however does not come in as a surprise since the optimal 90° torsion angle between thiophene rings seen in MRC forcefield prevents the conjugated backbone from staying planar, which in turn reduces the packing efficiency of P3HT molecules. Modifying the torsion term allows the forcefield to reproduce the π-π packing more accurately.

M_W (g/mol)	**Density (g/cm^3)**	
	MRC forcefield[77-79]	**Modified MRC forcefield**
3,320	0.96	1.10
6,474	0.96	1.11
13,280	0.91	1.14
26,560	0.94	1.15
experimental value	1.10 ± 0.05	

Table 3. Simulated density at 300K and 1atm of crystalline P3HT ensembles at different M_W. Inadequate π-π packing in MRC forcefield did not allow for a reproduction of experimental density.

To thoroughly validate the simulated crystal structure of P3HT against experimental results, we carried out NPT simulations at 300 K and 1 atm for 30 ps followed by a geometric optimisation using both the MRC and modified forcefields. The simulated system consists of 12 polymer chains each with 12 monomers inside a unit cell following Brinkmann's reported crystal structure; each polymer chain is of infinite length. The resulting crystal lattice parameters indicate that the modified forcefield reproduces experimental values within 1% of difference in contrast to 5% difference obtained using MRC forcefield (c.f. Table 4). A closer look at the lattice parameters reveals that significant difference in crystal structure computed using MRC forcefield arises from the 'b' direction which corresponds to π-π stacking. Thus, by changing the torsion terms we have enhanced the accuracy of the forcefield in describing the

molecular arrangements in P3HT, especially in the π-π direction which is crucial for both morphology evolution and charge transport.

Lattice parameter	Brinkmann's Experimental result	Optimised by Modified forcefield	Optimised by MRC forcefield
a	16.00 Å	16.05 Å	15.82 Å
b	7.80 Å	7.71 Å	8.19 Å
c	7.80 Å	7.77 Å	7.59 Å
α	90.00°	90.45°	91.29°
β	90.00°	90.04°	89.54°
γ	86.40°	86.11°	87.93°

Table 4. Lattice parameters of crystalline P3HT as obtained from experimental methods and MD simulations using both MRC and modified MRC forcefields. For MD simulations, NPT ensembles at 300 K and 1 atm were run for 30 ps before carrying out geometry optimisations. The significant difference of 'b' lattice reveals inadequate description of π-π stacking in MRC forcefield which was corrected in the modified forcefield.

The above validation allows us to compare the simulated solid state molecular arrangements of P3HT with experimental results. However, it is not conclusive if the modified forcefield would be able to correctly reproduce the system dynamics which plays an important role in morphology evolution. To validate the dynamics model of the modified forcefield, we compared simulated melting temperature (T_m) of P3HT against experimental data at M_W ranging from 3,000 g/mol to 40,000 g/mol.

To simulate T_m, P3HT molten structures were generated by first placing equal number of straightened P3HT chains along the a, b and c direction in a unit cell with all angles set to 90° and lattice dimension slightly larger than that of the end-to-end distance of a straightened P3HT chain (i.e., 40 nm for 14,967 g/mol and 80 nm for 29,932 g/mol). For high molecular weight (>14,000 g/mol) we employed six molecules (2 along each direction) and twelve for smaller molecules (<10,000 g/mol with 4 along each direction) in a unit cell. These initial structures were then heated up to 1,000 K and 100 atm so that they would shrink to the equilibrium density within 300–500 ps. As the systems reached a stable density, we continue the system relaxation at 700 K and 1 atm for 1000 ps. These molten P3HT systems were then quenched at 0.125 $K \cdot ps^{-1}$ or 1.25×10^{11} $K \cdot s^{-1}$ until it reached room temperature (300K).

During the run, density of the system as a function of temperature was recorded and analysed. With such a high cooling rate, it is expected that instead of a discontinuity in the cooling curve at the melting point, a glass transition (T_g) (which translates to a sudden change in expansion coefficient or slope of the density vs. temperature profile) would be observed (c.f. Figure 12). This is in line with the theoretical understanding that glass transition temperature increases linearly with the natural logarithm of the cooling rate[105] and that the thermodynamic melting point is the upper limit for the rate-dependent glass transition of a supercooled melt. To verify that cooling rate of 1.25×10^{11} $K\cdot s^{-1}$ is sufficient for the overlapping of T_g and T_m, we simulated heating process for a crystalline P3HT system (following Brinkmann's reported structure[101]) with M_W of 6,653 g/mol in a unit cell consisting of 12 molecules. The initial structure was equilibrated under NPT at 250 K and 1 atm for 1,000 ps. After which, the system was subjected to heating at 1.25×10^{11} $K\cdot s^{-1}$ until 650 K. During this process, the density profile as a function of temperature was recorded and compared with the cooling curve which shows similar result of T_g and $T_m \approx 460K$ (c.f. Figure 12a). Mean square displacement analysis over MD runs at 500 K (c.f. Figure 12b) show a characteristic positive slope after some simulation time, which confirms that melting already took place at 500 K or $T_m < 500K$. The result confirms that cooling of molten P3HT is sufficient to determine T_m of P3HT system; hence, simulated melting was only carried out for M_W of 6,653 g/mol.

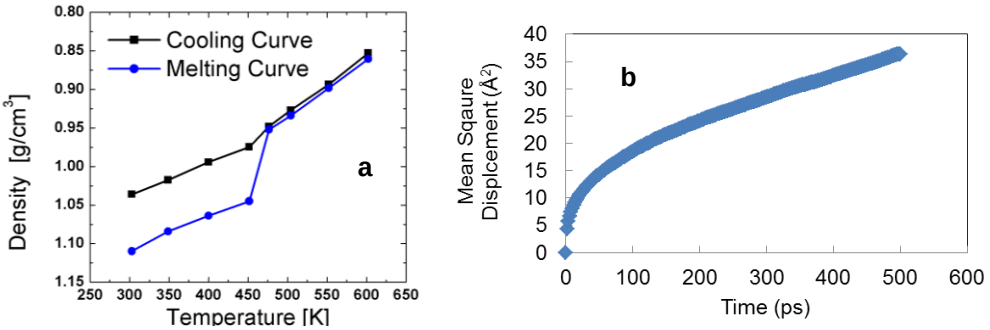

Figure 12. a) Cooling and heating curves of P3HT at M_W of 6,653 g/mol. Cooling curve was initiated from molten state while heating curve from Brinkmann's reported crystal structure. Both processes were subjected under a cooling and heating rate of 1.25×10^{11} $K\cdot s^{-1}$ respectively. The resulting similar values of T_g and T_m indicate that cooling curve alone is sufficient to determine T_m. b) Mean square displacement analysis over MD runs at 500 K further confirm that simulated $T_m \approx 460$ K as determined from melting and cooling curve is reasonable.

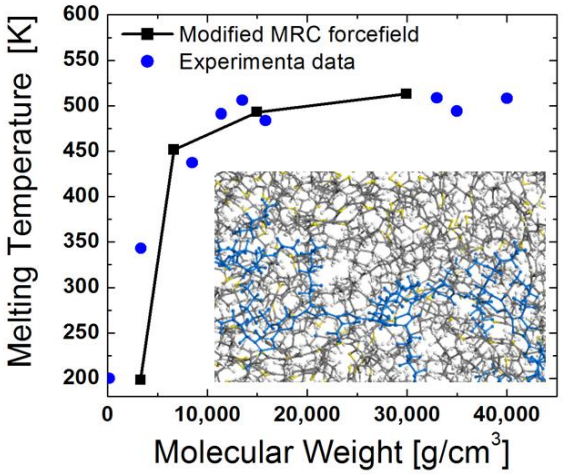

Figure 13. Melting temperatures of P3HT as a function of M_W obtained from simulation using the modified forcefield and experimental methods. Close agreement between simulations and experimental results confirm the validity of our modified forcefield in dynamics or morphology evolution studies. Inset shows snapshot of the MD simulation at 6,653 g/mol and T = 460K, highlighted blue atoms belong to a single P3HT molecule.

Comparison of experimental and simulated melting temperature of P3HT using the modified forcefield at different M_W can be seen in Figure 13. The simulated results were obtained from cooling curve as described above, while experimental results are adapted from various reports.[60, 106-108] Close agreement of experimental and simulated results reveals that the modified forcefield is able to replicate P3HT system dynamics accurately. Together with the previous validations, it can be concluded that our modified P3HT forcefield[98] is adequate for morphology study in P3HT:PCBM bulk heterojunction.

2.2.3.Morphology Study of P3HT:PCBM Blend

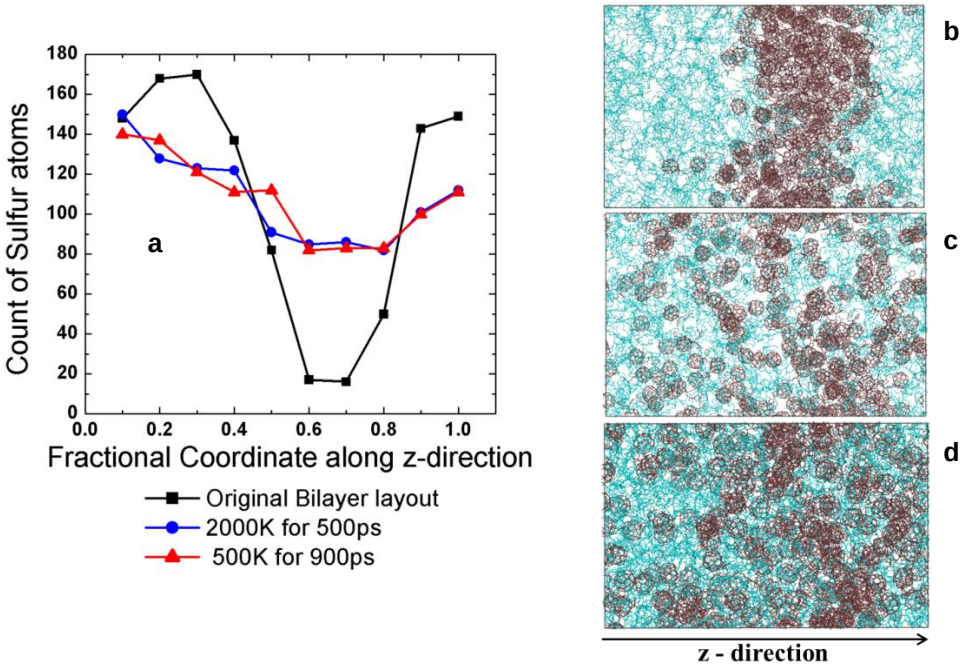

Figure 14. Morphology simulation of P3HT:PCBM blend with 6 P3HT molecules, each of 30,000 g/mol and 200 PCBM. a) Analysis of sulphur atoms distribution along z-direction shows diffusion of S-containing P3HT into PCBM regions after annealing at 2,000 K for 500 ps. The same trend continues but to a lesser extent when temperature is dropped to 500 K. The right-hand side graphs display simulation snapshots with PCBM shown in red and P3HT in light-blue for b) initial state of bilayer P3HT:PCBM layout; c) a more uniform distribution of both donor and acceptor after heat treatment at 2,000 K for 500 ps; and d) diffusion of P3HT/PCBM continues at 500 K yet with a lower rate due to the more densely packed structure at lower temperature.

The validated atomistic PCBM and P3HT forcefields were used for some preliminary bulk heterojunction morphology analysis. As a starting structure, we put 6 P3HT molecules each of M_W = 30,000 g/mol and 200 PCBM molecules in a bilayer structure which holds a total of 44,612 atoms in a unit cell of 7 nm x 7 nm x 11 nm dimension (c.f. Figure 14b). Individually, P3HT and PCBM structures were randomised by annealing in the molten state (700 K) for about 1000 ps followed by relaxation for another 1000 ps at 300K; hence they can be treated as amorphous except for the periodic boundary conditions. To mimic a bulk heterojunction blend, a bilayer structure was created by joining the above P3HT and PCBM substructures and the phases were allowed to mix at 2,000 K for 500 ps (c.f. Figure 14c). Thereafter the system underwent was relaxed at 500 K for about 900 ps (c.f. Figure 14d) to bring back the volume to a density close to experimental values (the density will have

decreased substantially during the 2000 K simulation facilitating the mixing) and to replicate the annealing process in P3HT:PCBM OPV which is often done at ~ 450 K (A slightly higher temperature was chosen here to speed up the equilibration).[71, 107] All simulations were carried out under NPT setting at a pressure of 1 atm.

By analysing sulphur atoms distributions along the z-direction, it is possible to qualitatively discern the degree of mixing of the two phases. From Figure 14a, it is clear that there is a strong phase separation in the original bilayer layout evident in the large difference between the count sulphur atoms in the middle of the cell and other regions; this corresponds to an aggregate of PCBM in the middle of the unit cell and highly pure P3HT phase elsewhere as seen in Figure 14b. After annealing at 2,000 K for 500 ps, the difference in sulphur atom count between different regions reduces significantly, indicating the interdiffusion of both species. Correspondingly, the simulation snapshot (c.f. Figure 14b) also shows a more uniform distribution of PCBM molecules. As the temperature dropped to 500 K, it is clear that after the 900 ps run, the overall distribution of both species changed only marginally which could be attributed to both low diffusion and higher density at low temperature. Nevertheless, we can still see the effect of further interdiffusion of two phases as the region of low sulphur content after annealing at 500 K is smaller (red curve) than before annealing at 500 K (blue curve). This is in line with recent experimental findings that PCBM can diffuse easily into amorphous P3HT.[61] However more detailed analysis at this atomistic level was not performed here due to the high computational demand of such atomistic calculations that – at least with the computational means available – limit the size of the unit cell that can be simulated to a value that is at best comparable to the expected domain size in P3HT:PCBM blend (which is estimated to be about 10 nm). Thus in the next section we will discuss forcefield coarse-graining which helped us improve computation speed by more than

100 times opening up the possibility to extend both the size of the simulated system and the simulated period.

2.3. Coarse-graining for efficient analysis[64]

In MD simulations, coarse-graining is a general term that describes the reduction in number of species or atoms in the system in order to save computation cost. This is typically done by representing a rigid group of atoms ("rigid unit") by a single pseudo-atom ("bead"), hence, omitting the interatomic interactions of the atoms within the rigid unit and only considering the interactions between beads. Since the number of calculations is reduced considerably, simulation speed is enhanced, but the accuracy of the final result may be lowered. Thus both the choice of the rigid unit or coarse-graining scheme and the forcefield parameters of the new forcefield must be derived carefully in order not to significantly alter the kinetics or thermodynamics of the system. In this work, we will adopt the same functional forms for coarse-grained forcefield. This means that each rigid unit is treated like a pseudoatom with charges, mass, VdW and other parameters analogous to an atom in an atomistic forcefield; thus, the same MD code can be applied to the new system. We will now discuss the choice of rigid unit and parameters derivation for P3HT and PCBM coarse-grained forcefield.

2.3.1. Coarse-graining Scheme

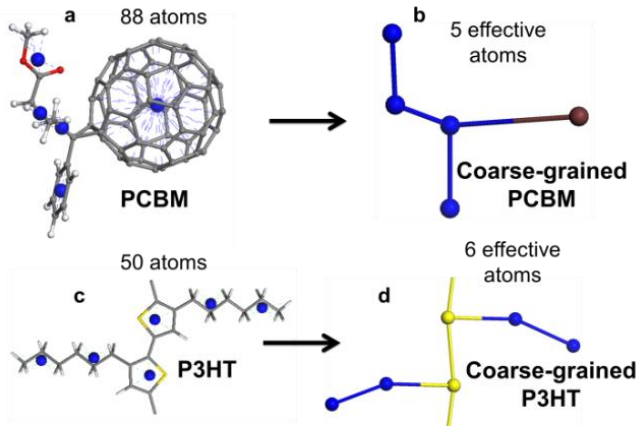

Figure 15. Atomic structure of a) PCBM and c) P3HT with the blue beads represent the centroid of each rigid unit and coarse-grained structures of b) PCBM and d) P3HT

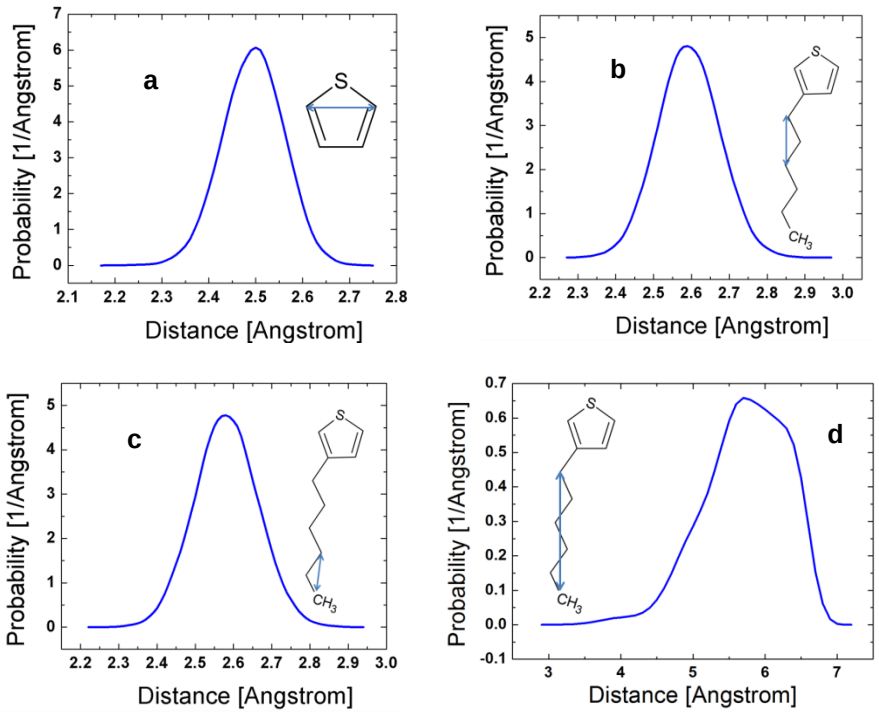

Figure 16. Length distribution of various rigid units in P3HT coarse graining scheme over NPT run 6 P3HT molecules, each of 6,653 g/mol at 500 K for 3,000 ps of a) C atom in the 2 and 5 positions of thiophene ring unit and terminal C atoms for the b) side chain segment nearer to thiophene ring and c) the remaining chain segment (these distances as shown as blue arrows in the insets). The small distribution spread of < 0.5 Å shows the rigidity of corresponding units. (d) The same analysis was carried out over the entire side chain where a significant spread of >2.5 Å means that the entire side chain is not rigid during MD simulations or further coarse-graining of the side chain would compromise the accuracy of the forcefield. Hydrogen atoms are not shown for clarity.

As mentioned earlier, coarse-graining involves representing each group of atoms with an effective atom positioned at the centroid of the group. Because the shape and characteristic of the effective atom ("bead") does not change in the course of MD

simulation, the effect on the accuracy of the simulations should be minimal as long as beads represent rigid units in the atomistic structure. The detailed coarse-graining scheme of both P3HT and PCBM can be found in Figure 15.

For P3HT, the choice of rigid units in this work closely resembled that of Huang et al. [80], which resulted in three types of coarse-grained atoms representing the thiophene ring, the C_3H_6 chain segment nearer to the thiophene ring and the terminal C_3H_7 chain segment in P3HT. This scheme can be seen in Figure 15c and d, where the blue beads in 'c' correspond to the centroid of the rigid unit or position of effective atom. To validate this choice of rigid units, we performed a structure analysis over NPT runs of 6 P3HT molecules, each of 6,653 g/mol at 500 K and 1 atm for 3,000 ps (c.f. Figure 16a-c). The small spread of < 0.5 Å of length distribution function observed consistently over all chosen rigid units indicates the validity of P3HT coarse-graining scheme. Note that further coarse-graining the side chain (representing the whole side chain by a single bead) would substantially compromise the accuracy of the forcefield. This is evident in the structure analysis of the side chain length (distance from the carbon atom covalently bonded to the thiophene ring to the terminal carbon atom on the side chain) calculated over the same MD simulation. This is shown in Figure 16d where significant spread of > 2.5 Å suggests that the side chain of each P3HT mere is not rigid during MD simulations.

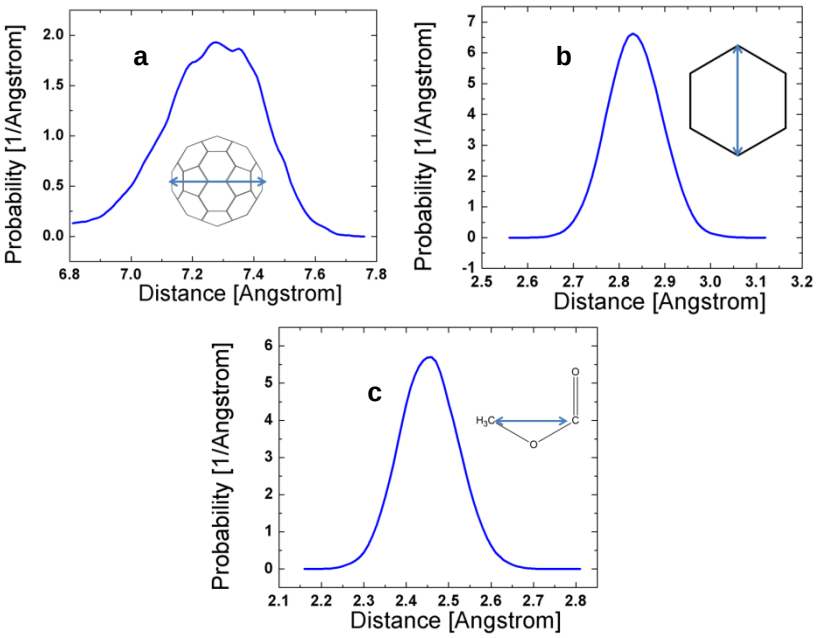

Figure 17. Length distribution of various rigid units in PCBM coarse graining scheme over NPT run 48 PCBM molecules at 600 K for 3,000 ps of a) diameter of fullerene C_{60} cage, b) largest dimension of 6-member ring and c) C-C distance of carbonyl group (similar to Figure 16 the blue arrows shows the length scale analysed). Small spread of < 0.5 Å for 6-member ring and carbonyl group and ~ 0.6 Å for C_{60} shows the current coarse-graining scheme is plausible. Hydrogen atoms are neglected for clarity.

For PCBM, we follow Huang et al.'s convention for representing fullerene C_{60} cage with a single bead.[80] However, (as Huang's work dealt with C_{60} instead of PCBM) a new coarse-graining scheme was suggested by us for the PCBM side chain. It appears straightforward to identify the C_2H_2 and C_2H_4 segments near to the fullerene cage (c.f. Figure 15) as such rigid units, since the shape of these groups heavily depends on C-C sp3 covalent bonds which remains largely unchanged during MD simulations due to the harmonic bond model (Equation (3.1)) (which translate to a quadratic increase in energy as bond gets longer than equilibrium distance; this also means no bond breaking or forming in the model) and a relatively large spring constant (which makes deviation from equilibrium value highly unfavourable).[79]

The choice of the other rigid units namely the fullerene cage, the 6-member ring and the carbonyl group as seen in Figure 15a and Figure 15b, is again based on a structure rigidity analysis over NPT runs of 48 PCBM molecules at 600 K and 1 atm for 3,000 ps. Similar to the analysis done for P3HT coarse-graining scheme, here we also look

at the length distribution function of key dimension in various chosen rigid units to decide on their relevance in the coarse-graining scheme. Again, the relatively low spread in the length distribution function (< 0.5 Å for 6-member ring and carbonyl group and ~0.6 Å for the C_{60} cage) confirms that the coarse-graining scheme chosen is plausible (c.f. Figure 17). It is also important to take note that the structure analysis done for both P3HT and PCBM (c.f. Figure 17 and Figure 16) was based on MD runs in molten state. Thus the coarse-graining scheme is valid even at elevated temperature.

2.3.2. Parameters Derivation

<table>
<tr><th>Interaction Type</th><th>Forcefield Parameters</th><th>Derivation Approach</th></tr>
<tr><td>Angle bend</td><td>k_{angle}, θ</td><td rowspan="4">Least square fitting
against atomistic forcefield</td></tr>
<tr><td>Bond stretch</td><td>k_{bonds}, r</td></tr>
<tr><td>Torsion</td><td>$V_1, V_2, V_3, V_4, \theta$</td></tr>
<tr><td>Coulomb</td><td>q</td></tr>
<tr><td rowspan="2">VdW</td><td>σ</td><td>Diameter of smallest sphere enclosing all constituents
and half of this for planar units
scaled to reproduce ***experimental density***</td></tr>
<tr><td>ϵ</td><td>Sum of all constituents' ϵ
scaled to reproduce ***experimental melting point***</td></tr>
</table>

Table 5. Summary of approaches used to derive different coarse-grained forcefield parameters.

As mentioned earlier, the same functional from used for atomistic forcefield was employed for coarse-grained forcefield. Unlike Huang's approach to calculate the energy landscape of up to 1.2 nm around each atom for each type of interaction[80], we also took into account long range interactions beyond 1.2 nm thus making gas phase simulations possible. Furthermore, the forcefield presented here can be readily integrated into most available MD codes and allows for easy incorporation of solvent or additives into the forcefield. However, parameters derivation for this approach is

not trivial and varies with each type of interaction. A summary of the derivation methods used for each of the forcefield components can be found in Table 5.

The derivation of the parameters for the coarse-grained forcefield started with short-range interactions that are angle bend, bond stretch and torsion. These were calculated by direct fitting against atomistic forcefield. First, geometry of single molecule of P3HT and PCBM was optimised in gas phase using the previously derived atomistic forcefield. By moving all atoms in the coarse-grained rigid unit together, we varied the different angle bend, bond length and torsion angle accordingly. For each variation, the change of system energy caused by the respective interaction type was determined using the atomistic forcefield. The thereby recorded energy profiles as a function of bond angle, bond length or torsion angle was used to derive the respective parameters for the coarse-grained forcefield. Fitting results for short range interactions are available in Appendix B and Appendix C.

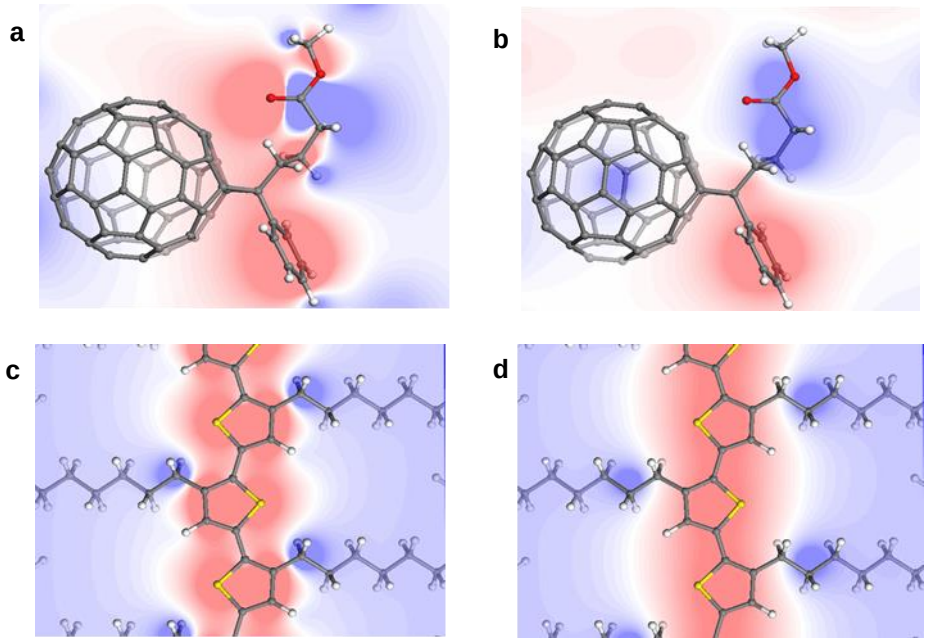

Figure 18. Electrostatic potential of a single isolated PCBM (a and b) and P3HT (c and d) molecule. (a) and (c) were based on atomistic forcefield while (b) and (d) on coarse-grained one.
Red: Negative Potential; Blue: Positive Potential

To derive the charges for the new system, we considered the electrostatic potential of P3HT and PCBM in their crystalline state. For P3HT, this was the reported

Brinkmann's structure[101]; for PCBM, a DFT optimised structure was used (c.f. Section 2.2.2.1). These optimised structures were then converted to their corresponding coarse-grained forms starting from random charges placed at the beads. These charges were then relaxed until the electrostatic potential of coarse-grained structure agreed closely with the atomistic one especially in regions of more than 1 Å away from the atoms in the atomistic model (as this region is more relevant for the intermolecular interactions). The electrostatic potential in periodic boundary condition was computed by solving Poisson equation using Fast Fourier Transform (FFT) method. A comparison between the electrostatic potential of a single isolated molecule as computed from the atomistic model and its corresponding coarse-grained counter-part reveals suitable agreement between two models (c.f. Figure 18).

For the VdW contributions, the two parameters σ and ϵ (c.f. Equation(3.1)) were derived in a two-step procedure. First initial estimates of σ and ϵ are obtained. For σ, which is the equilibrium distance between two identical species, a value equivalent to the diameter of a smallest sphere that could enclose the whole rigid unit was given. This value, however, is an overestimation for planar units such as thiophene rings or 6-member rings. Thus for these flat units, the radius of the smallest sphere enclosing the structure was used as a first estimate. For ϵ, which defines the strength of VdW interactions, the sum of ϵ from the atomistic forcefield of all constituents were used as the initial value. In the next step, the updated coarse-grained forcefield were used to optimise the crystalline P3HT and PCBM structure obtained from Brinkmann's work and DFT simulation as described above. σ values were then scaled accordingly until a close agreement (< 5 %) in crystal lattice parameters and densities with the atomistic model is observed (c.f. Table 6). We then retained the new σ values and scaled ϵ such that experimental melting temperature can be reproduced with the coarse-grained forcefield. In this work the melting temperature of 551 K for PCBM and 450 K for P3HT at 6,653 g/mol were adapted for the derivation of ϵ.[106, 107]

Simulated melting temperatures were obtained by finding discontinuity in the curve of density versus temperature recorded during heating of crystalline P3HT and PCBM (as discussed in Section 2.2.2.2). Heating curve of crystalline P3HT at 6,653 g/mol and PCBM calculated using the refined coarse-grained forcefield can be seen in Figure 19.

Parameters	% difference crystalline PCBM	% difference crystalline P3HT
a	-0.81	-1.73
b	4.67	4.50
c	-4.45	-1.05
Density	0.80	-1.61

Table 6. Percentage difference of crystal lattice parameters and density of crystalline P3HT and PCBM between optimised structures using coarse-grained forcefield and experimental result (for P3HT) and DFT simulation (for PCBM). Positive values mean coarse-grained forcefield gives larger result and vice versa

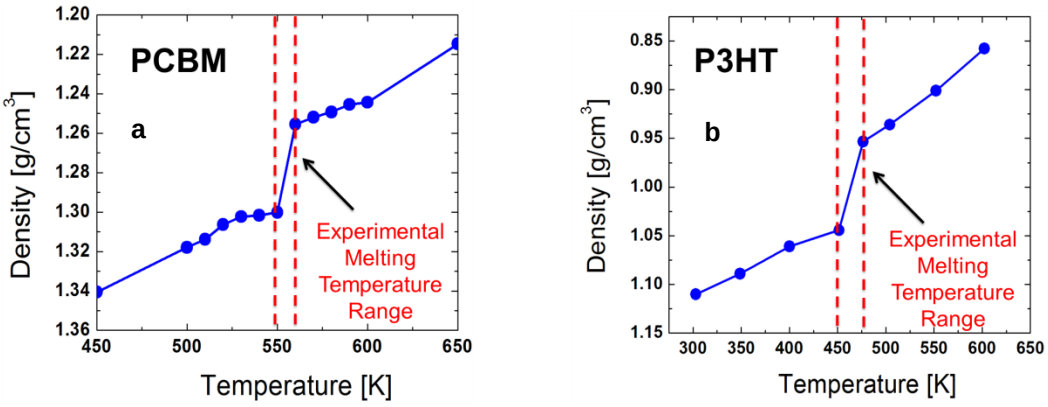

Figure 19. Heating curve of a) crystalline PCBM and b) crystalline P3HT at 6,653 g/mol show melting temperatures range closely resemble that of experimental data.

2.3.3. Validation of Coarse-grained Forcefield

Further validation of the coarse-grained forcefield was done by benchmarking the Radial Distribution Function (RDF) as computed by the coarse-grained against the corresponding calculations performed with atomistic forcefields (c.f. Figure 20). To this end, ensembles of 48 PCBM molecules and 12 regioregular P3HT molecules at M_w = 14,967 g/mol or degree of polymerization (DP) = 45 both at T = 600 K and P = 1 atm were equilibrated using both forcefields for 1,000 ps. MD simulations were performed on the final structures for another 500 ps, over which the RDF analysis of fullerene centroids and thiophene rings on different molecules of the respective

systems were carried out. Close agreement between atomistic and coarse-grained curves for both PCBM and P3HT (c.f. Figure 20) suggests that the essential features of the structures simulated using the atomistic forcefield are largely preserved by our coarse-grained forcefield.

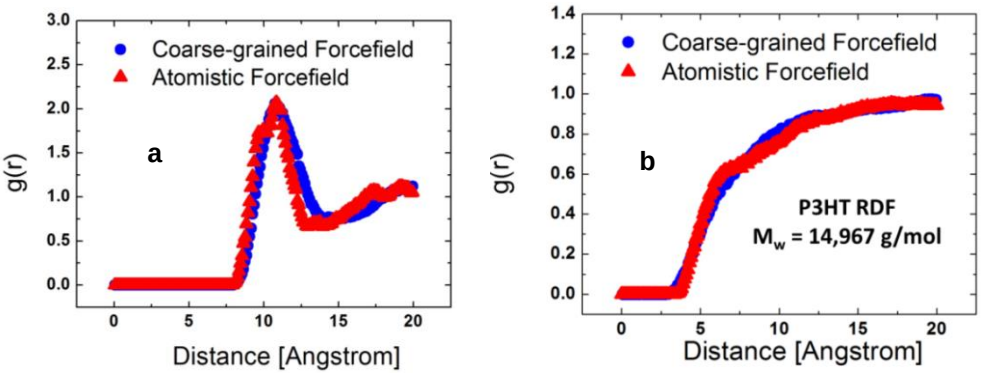

Figure 20. RDF of (a) 48 PCBM molecules and (b) 12 P3HT molecules at M_w = 14,967 g/mol or DP = 45 computed using both coarse-grained and atomistic forcefields at T = 600 K and P = 1 atm. Both systems underwent MD simulation for 1,500 ps with the last 500 ps reserved for RDF analysis. The close agreement between the results by both forcefield indicates that negligible accuracy loss was incurred by coarse-graining

For P3HT, we also compared the simulated melting temperature at M_w of 29,932 g/mol, 14,967 g/mol, 6,653 g/mol and 3,320 g/mol as obtained with the coarse-grained forcefield against result obtained with the atomistic forcefield[98] and reported experimental data[60, 106-108] (c.f. Figure 21). The procedure for melting temperature simulation using the coarse-grained forcefield is analogous to the corresponding calculation performed with the atomistic forcefield (c.f. Section 2.2.2.2). We first generate disordered structures of P3HT with the corresponding M_w by putting 8 straightened P3HT molecules along each crystal lattice a, b and c direction in a cubic unit cell (i.e. each unit cell contains 48 molecules) with dimension slightly greater than the contour length of individual molecules. These disordered starting structures were then annealed at 1,000 K and 100 atm to relax to a stabilised density which was typically achieved within 500 ps. The resulting structures were further equilibrated for 1,000 ps at T = 700 K and P = 1 atm. The persistence length of P3HT, averaged over the last 100 ps, for various M_w after annealing at 700 K yielded 2.5 nm ± 0.5 nm

which closely resembled experimental result of 2.4 nm ± 0.3 nm[109]. These structures are thus considered to be amorphous (except for the periodic boundary condition).

The final amorphous structures are then cooled down at a rate of 0.125 $K \cdot ps^{-1}$ or 1.25×10^{11} $K \cdot s^{-1}$ from 700 K to room temperature 300 K and the changes in volume as a function of temperature were recorded for each structure. With such a fast cooling rate, we expect the glass transition temperature to coincide with the thermodynamic melting temperature[98], thus melting temperature is recorded at the point where the change in slope occur in the volume versus temperature curve. The graph of simulated melting temperatures as a function of M_w (c.f. Figure 21) shows that coarse-grained forcefield agrees even more closely with experimental data than the atomistic forcefield. Based on this, the RDF analysis (c.f. Figure 20) and the properties-based coarse-grained forcefield derivation process, we are convinced that the coarse-grained forcefield presented in this work would replicate faithfully the energetics and structural evolution of the P3HT:PCBM system.

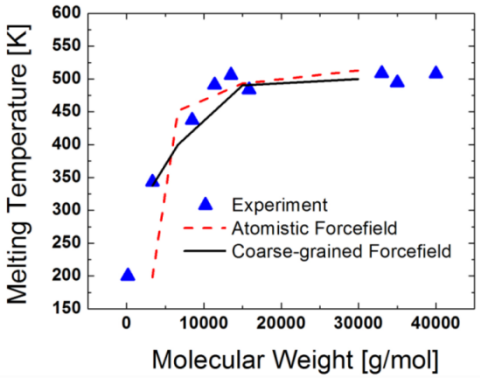

Figure 21. A comparison between simulated meting temperatures calculated using both coarse-grained and atomistic forcefields and experimental data at various M_w of P3HT shows that the dynamic of the system is more correctly reproduced by the coarse-grained forcefield

2.3.4. Time Scale

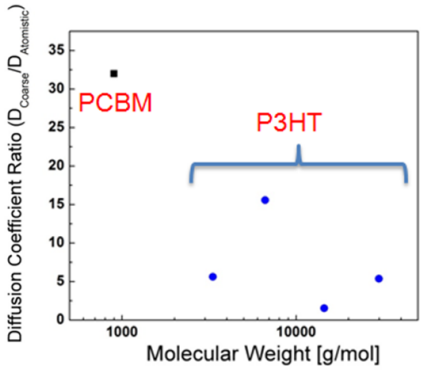

Figure 22. Simulated diffusion coefficient ratios as calculated using coarse-grained and atomistic forcefields analysed over 1,000 ps of NPT simulations at T = 600 K and P = 1 atm for 48 PCBM molecules and 12 P3HT molecules at M_w of 29,932 g/mol, 14,967 g/mol, 6,653 g/mol and 3,320 g/mol or DP of 90, 45, 20 and 10.

It is well-known that coarse-grained forcefields have faster dynamics compared to atomistic ones.[80, 110-112] This is because the coarse-graining makes polymer chains smoother and thereby artificially reduces the friction associated to the relative motion of different polymer chains.[111] Here, we assessed the difference in dynamics evolution between atomistic and coarse-grained forcefields by comparing the simulated diffusion coefficient of both PCBM and P3HT systems. NPT simulations at T = 600 K and P = 1 atm were carried out for 1000 ps for 48 PCBM molecules and 12 P3HT molecules at M_w of 29,932 g/mol, 14,967 g/mol, 6,653 g/mol and 3,320 g/mol or DP of 90, 45, 20 and 10. The ratio of the diffusion coefficient calculated using the atomistic and coarse-grained forcefields is presented in Figure 22. We can see that PCBM has a higher dynamics speed-up compared to P3HT, which is expected due to the higher degree of coarse-graining in PCBM. From Figure 22, we estimate the time scale of the coarse-grained forcefield to be about 10 times faster than that of the atomistic forcefield. Combining the faster dynamics with the reduced number of atoms as a result of coarse-graining, a typical P3HT:PCBM blend at a 1:1 weight ratio can be simulated at about 100 times lower computational cost.

2.3.5. P3HT:PCBM Interface

2.3.5.1. Crystallinity Analysis

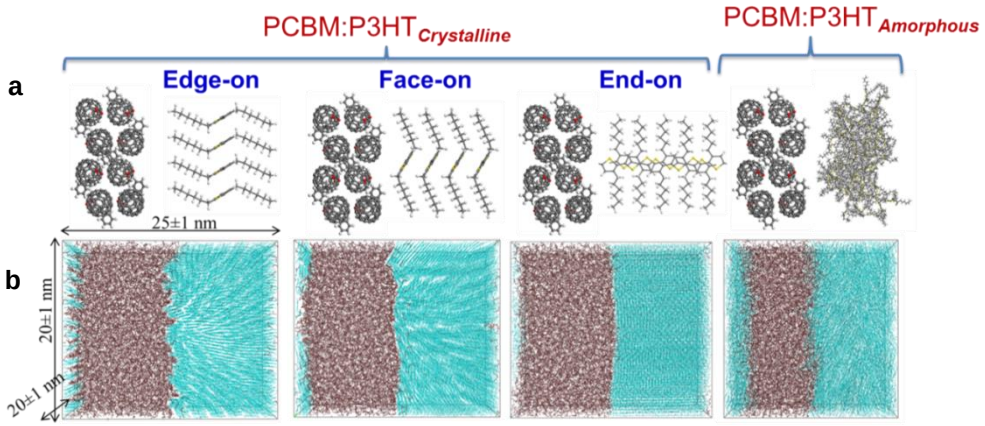

Figure 23. Illustration of the three different orientations of at the PCBM:P3HT$_{Crystalline}$ interface considered in this work (namely the edge-on, face-on, end-on based on the respective orientation of the polythiophene backbone) and PCBM:P3HT$_{Amorphous}$ using the (a) atomistic description for clarity and (b) their corresponding MD simulation snapshot after 10,000 ps at 450 K using the coarse-grained model. Red colour represents coarse-grained PCBM and cyan colour represents P3HT

Using the coarse-grained forcefield, we investigated the interface between P3HT:PCBM for crystalline and amorphous P3HT. For crystalline P3HT, three different crystal orientations at the interface namely face-on, end-on and edge-on were considered (c.f. Figure 23). For all cases the simulated unit cells were of 25±1 nm x 20±1 nm x 20±1 nm in dimension with a P3HT:PCBM weight ratio of 1:1. All structures underwent NPT simulation at T = 450 K for 10,000 ps with the first 1,000 ps as equilibration period. The choice of this time scale is appropriate because, as demonstrated in Figure 24, the system energy variation as a function of simulation time at different bilayer configurations converges after about 4,000 ps for the cases involving crystalline P3HT. For the case of amorphous P3HT:PCBM thermodynamic convergence of the interfacial energy cannot be reached at this timescale. For this system, a linear energy reduction is observed after 10,000 ps, which we attribute to the intercalation of PCBM into P3HT. This means that prolonged simulations will in this case lead to a more and more diffuse interface and consequently a less comparable estimate of the energetics at amorphous P3HT:PCBM interfaces.

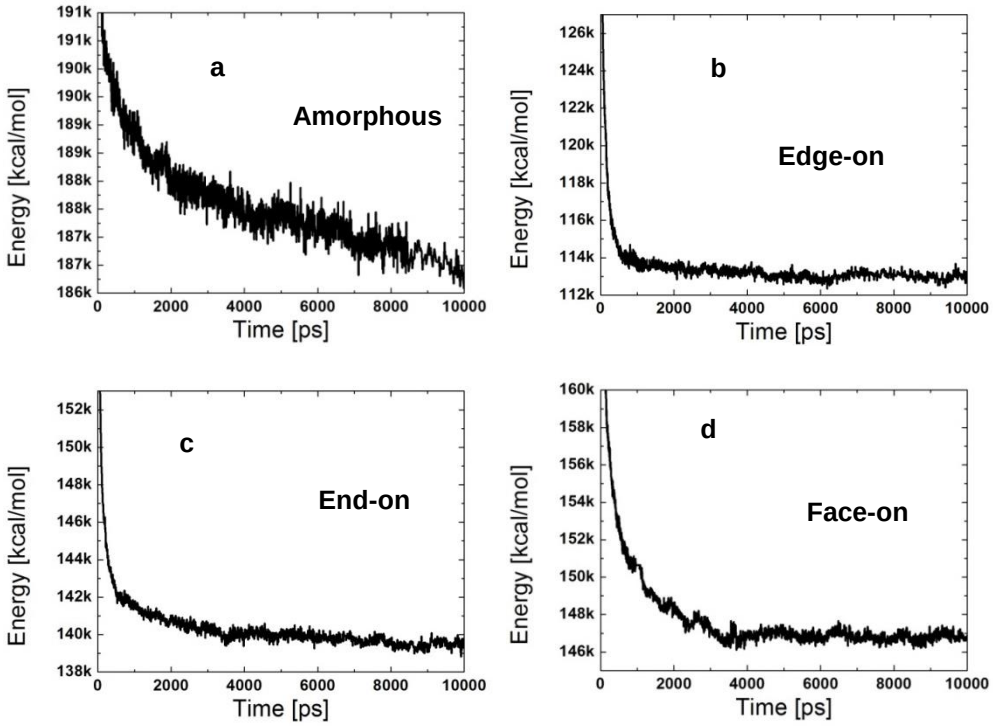

Figure 24. Energy profile of different P3HT:PCBM interfacial configurations a) Amorphous, b) Edge-on, c) End-on and d) Face-on as a function of simulation time. It is clear that for interfaces between crystalline P3HT and PCBM (b-d), convergence is achieved after about 4,000 ps. For amorphous P3HT:PCBM interface (a) a linear reduction of system energy is observed after 10,000 ps which is attributed to the intercalation of PCBM into amorphous P3HT. Analysis of the amorphous P3HT:PCBM interface at a much later time frame would have to be carried out over a more diffuse interface which reduces the accuracy of both interfacial energy calculation and PCBM intercalation analysis.

Figure 23b shows the snapshots of MD simulations for the corresponding P3HT orientations after 10,000 ps. It is clear from Figure 23b that the end-on configuration results in a smoother interface compared to the other two cases. Our calculations show that the end-on simulated interface has an average root-mean-square (rms) roughness value of 4.2 ± 0.16 Å while rms values for edge-on and face-on configurations are 7.1 ± 0.3 Å and 7.2 ± 0.5 Å, respectively. One of the reasons for the difference in interface roughness values is the presence of electric dipoles along the P3HT back-bone chains preventing π-stacked adjacent chains to slide against each other along the common chain direction. This means that for the edge-on and face-on cases, P3HT chains move more freely perpendicular to the P3HT:PCBM interface, hence creating a rougher surface. Furthermore, the face-on configuration exhibits the lowest interfacial energy compared to other configuration (c.f. Section 2.3.5.2), which

leads to a strong drive towards maximising the interfacial area, and hence to a further roughening.

To assess the crystallinity of either P3HT or PCBM in the system, we employed the orientational order parameter S, which measures how well each individual entity is aligned to an average direction. Typically, a value of $S \geq 0.3$ is considered to indicate crystalline regions.[113]

$$S = \frac{3}{2}\left\langle (\mathbf{u}\cdot\mathbf{n})^2 - \frac{1}{3}\right\rangle \qquad \text{where} \qquad \mathbf{n} = \frac{\langle \mathbf{u}\rangle}{|\langle \mathbf{u}\rangle|} \tag{3.14}$$

Here, the unit vectors **u** and **n** represent the orientation of an individual entity and the average orientation over all entities within the same volume element, respectively (c.f. Figure 25a). For P3HT we define **u** to be the orientation direction between adjacent thiophene rings beads and for PCBM the direction from the bead representing C_2H_2 group to the one representing the C_{60} cage of the same molecule (see Figure 25b,c). For P3HT, we further distinguish the intermolecular S_{inter}, which assesses how well-aligned different chains are with respect to each other, from the intramolecular S_{intra}, which assesses the correlation between the orientation of segments of the same chain, i.e. how straight the chains remain (c.f. Figure 25b). A value of S is calculated for each cubic grid of 3 nm edge length (unless otherwise stated) within the unit cell.

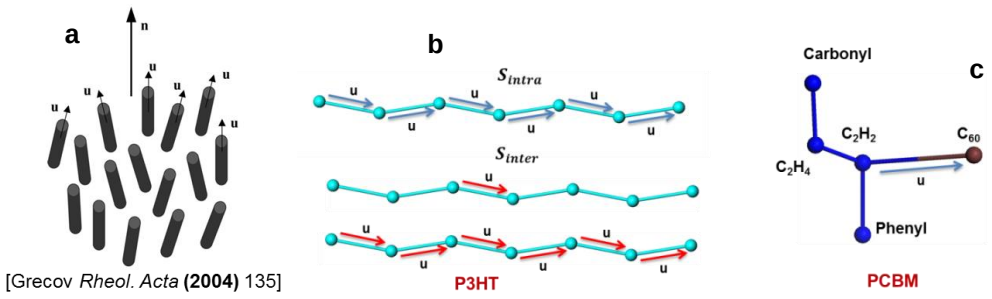

Figure 25. (a) Illustration of **u** *and* **n** *which are used in the calculation of the orientational parameter S. (b) For P3HT,* **u** *is defined as the direction from one thiophene ring to its neighbour within the same chain; for S_{intra} and S_{inter} only the* **u** *within the same chain and on different chains are considered, respectively. (c) For PCBM,* **u** *is defined as the direction from coarse-grained C_2H_2 to the C_{60} group within the same molecule.*

The variation of *S* as a function of simulation time reveals that PCBM quickly loses its orientational order at 450 K for all three edge-on, end-on and face-on configurations (c.f. Figure 26a). Accordingly, an RDF analysis of the C_{60} beads for the last 1,000 ps of the MD simulations for all three configurations shows a single sharp peak at ~ 10 Å for the nearest neighbour distance and diffuse peaks for larger distances (c.f. Figure 26b). This clarifies that PCBM loses its long range order at 450 K. Therefore, PCBM crystal orientations will not be considered in this work.

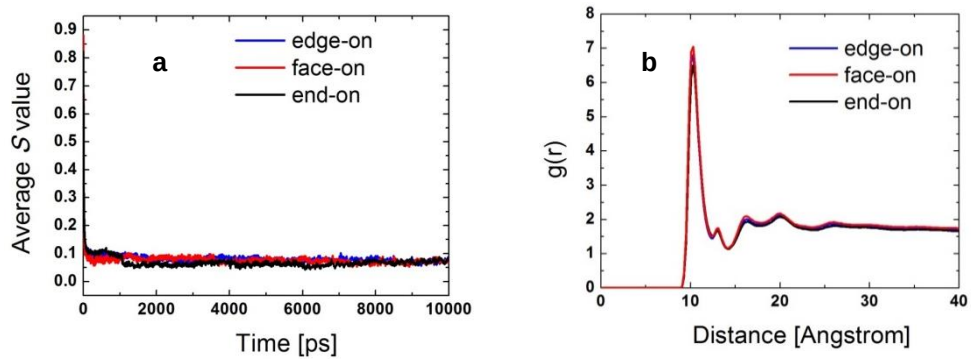

Figure 26. (a) Average S value of PCBM as a function of simulation time for all three P3HT configurations. Average S value reduces to about 0.1 after approximately 100 ps, this shows PCBM does not retain its orientational order at 450 K. (b) RDF analysis of C_{60} bead over the last 1,000 ps of simulation for all 3 P3HT configurations indicating that PCBM does not retain long-range order at 450 K. The three configurations: edge-on (blue), face-on (red) and end-on (black).

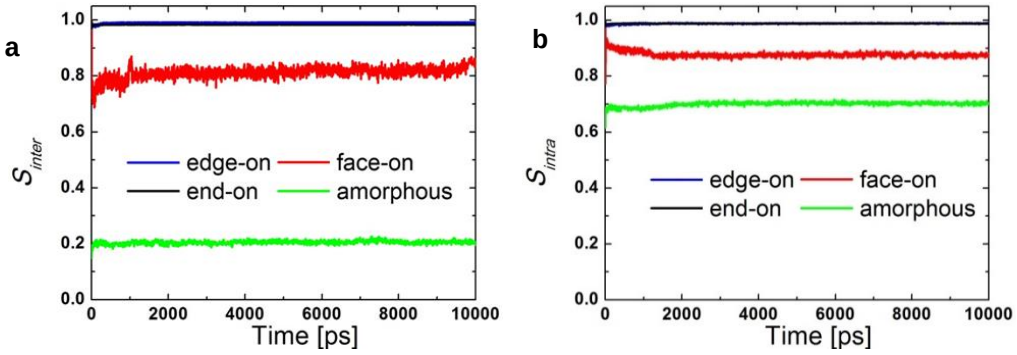

Figure 27. (a) S_{inter} and (b) S_{intra} value of P3HT as a function of simulation time for edge-on (blue), face-on (red), end-on (black) and amorphous (green) configurations. As expected, S_{inter} for the amorphous case is low (< 0.3), whereas S_{intra} is high (> 0.3) for all cases due to the high rigidity of P3HT chains.

Figure 27 shows the variation of S_{inter} and S_{intra} as a function of simulation time for edge-on, face-on, end-on and amorphous configurations. It is noticed that while S_{inter} remains low for the amorphous case (< 0.3), S_{intra} remains relatively large for all cases

(>> 0.3). This is reasonable since conducting polymer chains are relatively stiff (have a high Flory characteristic ratio value) due to the presence of conjugation.

For face-on and amorphous configurations, the crystallinity of P3HT shows a pronounced decrease with the distance from the interface (c.f. Figure 28a), while such trends were not observed on the simulated length scale for end-on or edge-on configuration. It should be noted that the apparent increase of the crystallinity for distances > 6 nm (i.e. half the P3HT layer thickness) is simply due to the proximity of the opposite P3HT:PCBM interface in the periodic structure model. Furthermore, the values of S_{inter} for the interfaces with face-on and amorphous configurations also vary with changing grid size (c.f. Figure 28b), suggesting differences in the orientational correlation length (≈ 3 nm for the amorphous P3HT layer, and ≥ 10 nm for the face-on P3HT layer) respectively. Thus the size of P3HT crystallites in the vicinity of low-energy P3HT:PCBM interfaces, are of the same order of magnitude as the simulated P3HT domain size (here ca. 12 nm) so that configurations at opposite interfaces to some extent will influence each other. In contrast, no dependence of S_{inter} on the grid size is observed for edge-on or end-on configurations.

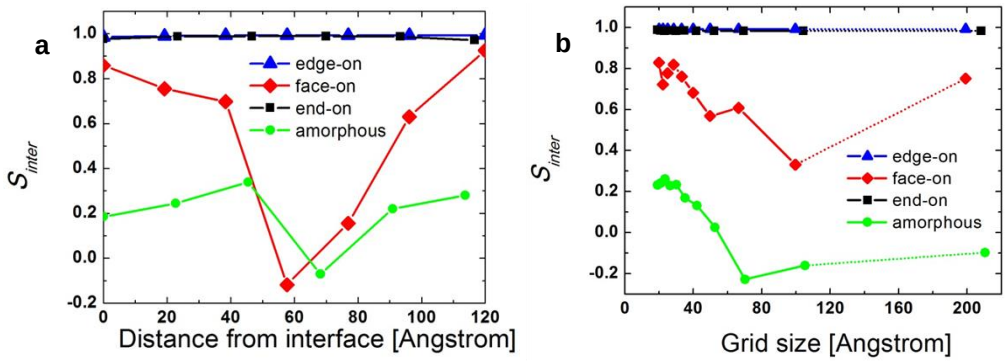

Figure 28 Variation of S_{inter} as a function of (a) distance from the interface and (b) grid sizes averaged over the last 100 ps. There is strong dependence in both (a) and (b) for face-on and amorphous interface configurations

2.3.5.2. Interfacial Energy

To better understand the changes of S_{inter} as a function of distance from the interface, we computed the interfacial energy of P3HT:PCBM in all configurations as the

difference between the system potential energy averaged over the last 200 ps and the sum of the potential energies of bulk P3HT and PCBM (The bulk potential energy values were determined analogously by simulations at 450 K for 1,000 ps and taking the average potential energy over the last 200 ps). The results shown in Table 7 indicate that the face-on configuration yields the most stable interface and that the interface energies for all crystalline phases are significantly negative indicating a driving force for phase separation. Only for the amorphous P3HT:PCBM interface the interface energy is marginally positive (or zero), indicating that phase separation into amorphous P3HT and PCBM phases does not constitute an energetic advantage. The pronounced negative interface energy for the face-on interface configuration suggests that a strong drive towards maximising interfacial area by forming a zig-zag interface, which will contribute to the decrease of S_{inter} with increasing grid size (c.f. Figure 28b). No such effect was observed for edge-on and end-on configurations possibly due to the less stable interface compared to face-on resulting in a smaller drive towards maximising of interfacial area.

P3HT orientations	**Interfacial energy (eV/nm^2)**
edge-on	-0.19 ±0.02
face-on	-1.34±0.03
end-on	-0.13±0.02
amorphous	0.01±0.01

Table 7. Simulated interfacial energy between P3HT and PCBM for various P3HT orientations.

It was demonstrated from ab-initio calculation of individual molecules that the face-on configuration is a local minimum of the P3HT:PCBM interfacial energy landscape.[114-116] Here with the aid of coarse-grained MD, we have confirmed for systems of typical dimensions found in the active layers of BHJ devices that face-on and amorphous P3HT:PCBM are the most stable and unstable configurations, respectively.

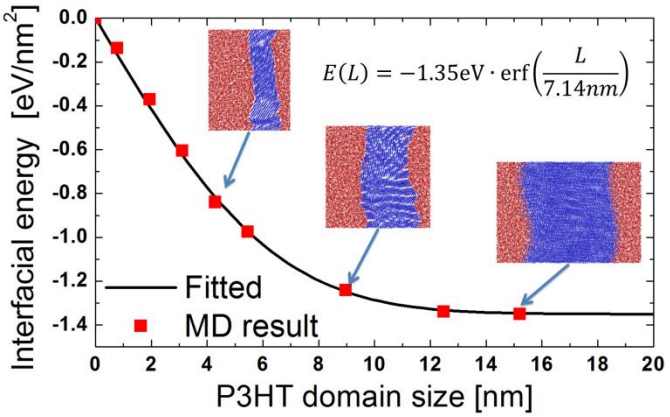

Figure 29. Changes of interfacial energy as a function of underlying P3HT thickness calculated using coarse-grained simulation (red symbols) and fitted using error function (black line)

It should be noted that the resultant negative energy value should not be mistaken as a driving force toward P3HT domain size minimization. This is because the results presented in Table 7 are only relevant for fixed P3HT domain thickness of approximately 12 nm. Shrinkage of P3HT domain could lead to increment of the interfacial energy such that for a P3HT domain size of 0 nm (pure PCBM), the interfacial energy should reach zero. An investigation of the interfacial energy as a function of P3HT domain thickness can be seen in Figure 29. For the calculations summarised in this graph, the PCBM layer thickness is identical to that of the calculations presented above (c.f. Table 7), while the P3HT layer thickness is systematically varied from 0 to 15 nm or 40 monolayers in the energetically most favourable face-on configuration. All structures went through 10,800 ps equilibration at 450 K, followed by a short 200 ps production run at 450 K, for which the average potential energy of the system is determined. Interfacial energies were taken as the difference between the system potential energy and the sum of the potential energies of bulk P3HT and PCBM systems similar to earlier discussion.

The curve from Figure 29 was fitted using an error function. This choice is inspired from the summation over reciprocal lattice in Ewald summation of Coulomb interactions (c.f. Section 2.2.1.1) (c.f. Equation 3.14).

$$E(L) = E_0(L) \cdot \mathrm{erf}\left(\frac{L}{\lambda^*}\right) = -1.35\ \mathrm{eV} \cdot \mathrm{erf}\left(\frac{L}{7.14\ nm}\right) \quad (3.14)$$

In Equation (3.14), $E(L)$ is the interfacial energy of the P3HT:PCBM bilayer, which depends on the underlying P3HT thickness L. It should be noted that the applicability of this functional form implies an interpretation of the variation in the interfacial energy as a nano-size effect due to the mutual interaction of space charge layers at opposite interfaces, if the distance between these interfaces is on the same length scale as the effective screening length λ^* of the local electric field at the interfaces. From Figure 29, it is clear that the optimal phase separated domain size is determined by the competition between the driving forces towards higher interfacial area (smaller domains) and higher interfacial energy per unit area (larger domains). To determine the optimal domain size obtainable from this energetics profile, MC simulation was employed and will be discussed separately in Section 2.4.).

2.3.6. Diffusion of PCBM into P3HT

Besides the interfacial configuration of P3HT:PCBM, the dynamics of the diffusion of PCBM into P3HT is also of great importance as it would shed light on molecular motion during bulk heterojunction phase separation and annealing. Previously, it has been reported from SIMS and thin film diffraction studies that there is no diffusion of PCBM into crystalline P3HT region[61] and diffusion of PCBM along P3HT grain boundaries takes place during annealing of the bilayer structure[74] leading to an observed pseudo-bilayer structure.[66] To better understand this phenomenon, we investigated the diffusion pathway of C_{60} into P3HT for the cases of face-on and amorphous P3HT by considering the changes of system energy as a coarse C_{60} probe is placed at regular interval position. The analysis was done for the final structures of face-on and amorphous cases after removal of PCBM molecules.

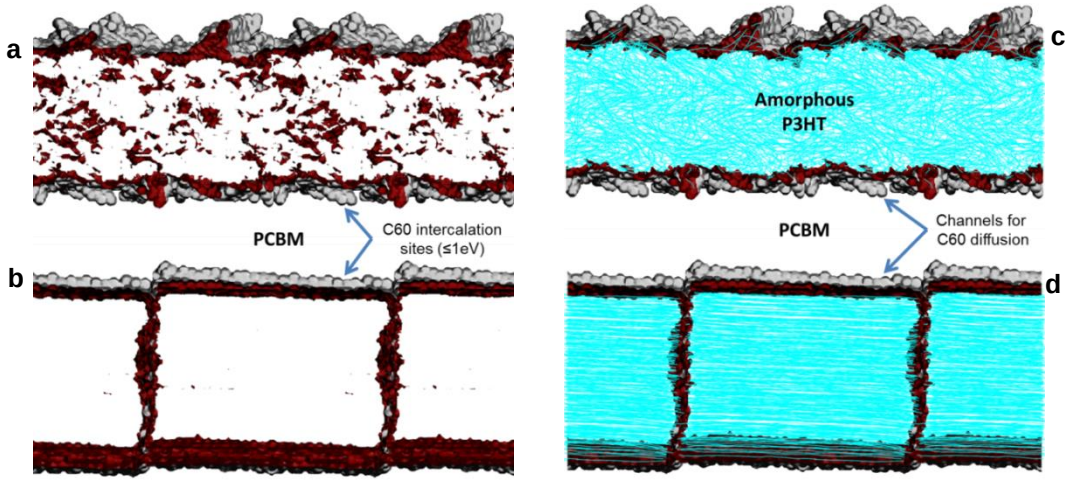

Figure 30. Isosurface of constant site energy (red regions) at 1 eV of C_{60} intercalation into crystalline (b and d) and amorphous (a and c) P3HT revealing possible low energy C_{60} intercalation sites (a and b) and channels for long-range diffusion (c and d) based on the final configuration of 20 ns MD simulations. Graphs (c and d) are obtained from (a and b) by retaining only those isosurface regions that form an infinite pathway (touching at least 2 opposite boundaries of the unit cell). While for the crystalline case there are continuous grain boundaries diffusion pathways across the P3HT layer, no analogue was found for the interface configuration with amorphous P3HT despite having a greater number of possible intercalation sites. Lines in cyan colour (c and d) denote P3HT chains (side-chains were omitted for clarity).

Figure 30a and b show the energy isosurface of 1 eV for the interfaces with face-on and amorphous P3HT, respectively based on the final configuration after MD simulation runs extended to 20 ns for these two cases. This value is chosen by considering the thermal fluctuations in the ensemble which could be approximated by a Gaussian distribution. The energy spread due to this fluctuation could then be written as $\delta E = \sqrt{C_V k_B T^2}$.[117] Here C_V is the heat capacity of C_{60} at constant volume, k_B is the Boltzmann constant and T is the temperature. By using C_V of 864 $J \cdot mol^{-1} \cdot K^{-1}$,[118, 119] δE can then be approximated to ~ 1 eV. Reasonable variations of this threshold value $hardly$ change the results in Figure 30.

From Figure 30, there are hardly any possible sites for C_{60} intercalation inside the crystallites of the crystalline structure as opposed to the amorphous case. The possible sites for C_{60} intercalation into crystalline P3HT are almost exclusively located where the chains end. Given that the model was constructed from fully crystalline P3HT structure, these chain ends mark the grain boundaries. To better assess if these

possible C_{60} intercalation sites would amount to a continuous diffusion pathway from the P3HT:PCBM interface, we retained only the isosurfaces that form a connected pathway touching at least two opposite surfaces of the unit cell (c.f. Figure 30c and d). It can be seen quite clearly that while face-on P3HT provide a connected pathway for C_{60} diffusion from the interface along grain boundary, diffusion length of C_{60} into amorphous P3HT occurs more in the sub-interface layer.

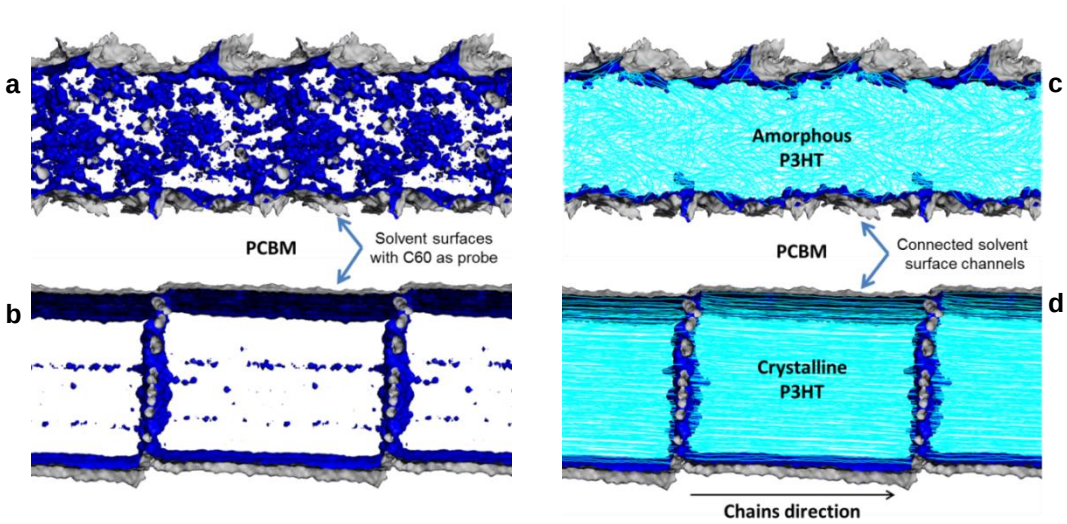

Figure 31. Solvent surface (blue) computed using coarse-grained C_{60} as probe for crystalline (b and d) and amorphous (a and c) P3HT based on the final configuration of 20 ns MD simulations.. (c and d) are obtained from (a and b) by considering only surface regions touching at least 2 opposite boundaries of the unit cell. The close resemblance of this to the energy-based calculation (c.f. Figure 30) suggests that PCBM diffusion inside the P3HT is related to local density. Lines in cyan colour (c and d) denote P3HT (side-chains were omitted for clarity).

The ability of C_{60} to diffuse into P3HT should be related to the amount of free volume in the structure. Our calculations showed that amorphous P3HT has a lower density than crystalline P3HT (~ 7% at 300 K and 6% at 450 K); hence more free volume is expected in amorphous P3HT which should also lead to an increased volume of possible pathways for C_{60} intercalation. To better understand this, we also plotted solvent surfaces in Figure 31a and b for the same face-on and amorphous structures as used in Figure 30. The solvent surface indicates the free volume regions within the P3HT phase that are large enough to host a C_{60} coarse-grained bead as the probe "solvent molecule". Similar to the energy-based calculations (c.f. Figure 30), we again explore, which of the isosurfaces form connected pathways (c.f. Figure 31c and

d). The results qualitatively agree with the energy calculations in confirming that C_{60} diffusion from the interface is possible along grain boundaries of crystalline P3HT due to lower density along these paths. While the isosurfaces of the energy-based and solvent probe calculations agree in their general features such as the location of pathways and (approximately) the possible sites for C_{60} intercalation, they are not identical because the energy-based calculations take into account the hardness of the VdW potential while the solvent probe only considers the VdW radius.

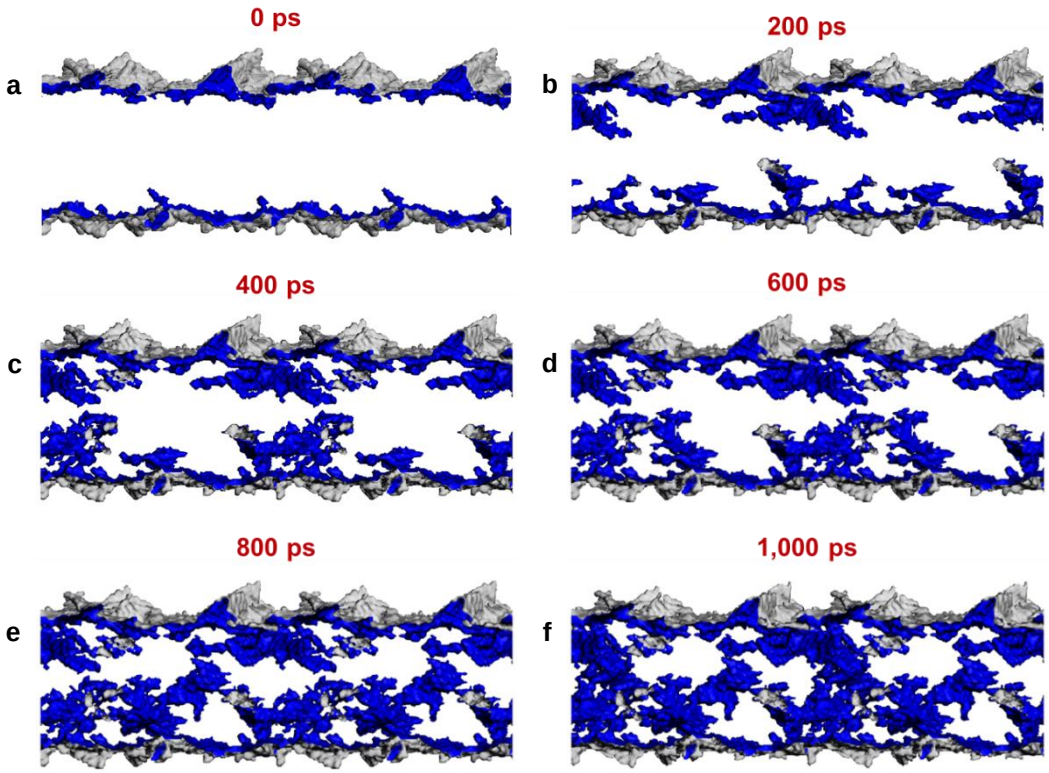

Figure 32. Diffusion pathway of C_{60} into amorphous P3HT obtained by superimposing C_{60} intercalation energy landscape over the last (a) 0 ps or 1 frame; (b) 200 ps or 20 frames; (c) 400 ps or 40 frames; (d) 600 ps or 60 frames; (e) 800 ps or 80 frames and (f) 1,000 ps or 100 frames of 10 ns MD simulations. The increasing amount of diffusion pathways as well as their penetration depth as we go from (a) to (f) suggests that C_{60} diffusion into amorphous P3HT is chain motion activation.

Furthermore, while for the analysed snapshot of the interface structure there are no connected pathways for C_{60} through the amorphous P3HT, there are certainly more possible sites for C_{60} within the amorphous P3HT regions. Thus more PCBM could be trapped in the amorphous P3HT regions. During annealing, chain motion could lead to migration of these sites, hence

transporting trapped PCBM deeper into amorphous P3HT regions. To verify this, we superimposed C_{60} intercalation energy landscapes at different time steps during the final 1,000 ps of our simulation to determine if a connected pathway could be formed. The results are shown in Figure 32 where it is clear that as more and more time-frames are added to the analysis, both the number of connected pathways and their penetration depths increase. After 1,000 ps or 100 frames, a percolating pathway was formed for C_{60} to diffuse from one interface to the opposite interface. This suggests that PCBM diffusion in amorphous P3HT is assisted by chain motion. A corresponding time-dependent analysis of transport pathways in crystalline P3HT does not find new percolating pathways so that long-range diffusion remains restricted to grain boundary regions.

By combining the PCBM diffusion into P3HT findings with the correlation between crystallinity and interfacial energy discussed above, we propose a phase-separation mechanism as follows: (1) Minimisation of system energy will take place via the nucleation of P3HT crystallites. (2)The growth of P3HT crystals will push adjacent PCBM molecules out of the crystalline P3HT regions. (3) Grain boundaries between P3HT crystallites will (as the amorphous phase) contain PCBM and act as diffusion pathways for the redistribution of PCBM to PCBM-rich regions.

It should be noted that while the findings presented so far have shed light on the physics influencing the phase separation process, resultant phase-separated morphology is not yet clear. To this end, we performed phase separation simulations using coarse-grained dynamics and MC methods which will be discussed in Section 2.3.7 and 2.4 respectively.

2.3.7.P3HT:PCBM Bulk Heterojunction Phase Separation

As mentioned, in OPV, the active layer morphology plays an important role in device performance. Typical OPV are made by thermal annealing of blended donor:acceptor mixture such that a phase separated bulk heterojunction could be obtained. In the previous sections, we have explored some of the guiding principles towards phase separation in P3HT:PCBM bulk heterojunction, yet the phase separated morphology has not been discussed. To solicit such a structure and its corresponding molecular resolution, which has been largely elusive to state-of-the-art characterisation techniques, we employed coarse-grained molecular dynamics simulation making used of the coarse-grained forcefield as derived and validated in Section 2.3.2 and 2.3.3.

Experimentally, a phase-separated bulk heterojunction present in most high performance P3HT:PCBM OPV are often obtained by thermal treatment of fully blended P3HT:PCBM mixture. To simulate this, we annealed a bilayer coarse-grained cell with 200 P3HT molecules each with M_W of 14,940 g/mol or consisting of 90 thiophene rings and 3280 PCBM molecules. The cell has an overall weight fraction of approximately 1:1 with a dimension of approximately $(20\ nm)^3$ at 300 K. The cell was first annealed at 2,000 K for 10,000 ps so that a thoroughly mixed bulk heterojunction could be obtained. Subsequently cooling at 300 K for 10,000 ps was administered; at the end of which a realistic density of 1.15 g/cm^3 was observed. The mixture was then annealed at 450 K to simulate experimental thermal treatment condition as discussed in previous sections. Snapshots of the simulations after 0ns (initial structure after annealing at 300 K), 16ns, 36ns and 66ns are shown in Figure 33 from which it is clear that while some limited clustering of P3HT (cyan beads) and PCBM (red beads) compared to the initial condition could be observed, discernible phase-separated morphology is yet to form. A more quantitative analysis of the phase separation evolution is shown in Figure 34a. T this end the cell is divided into grid elements of $(2nm)^3$. Elements with a P3HT weight fraction of >80% are considered to

be part of a P3HT domain. Adjacent grid elements that share at least 1 common interface and both have P3HT weight fraction >80% are considered to belong to the same domain. As seen in Figure 34a the volume fraction of all P3HT domains is about 10% of the simulated volume, up from 5% in the initial structure, with about 40% of all P3HT volume elements or 4% of the total volume clustered into the biggest P3HT domain, up from 0.3% in the initial structure.

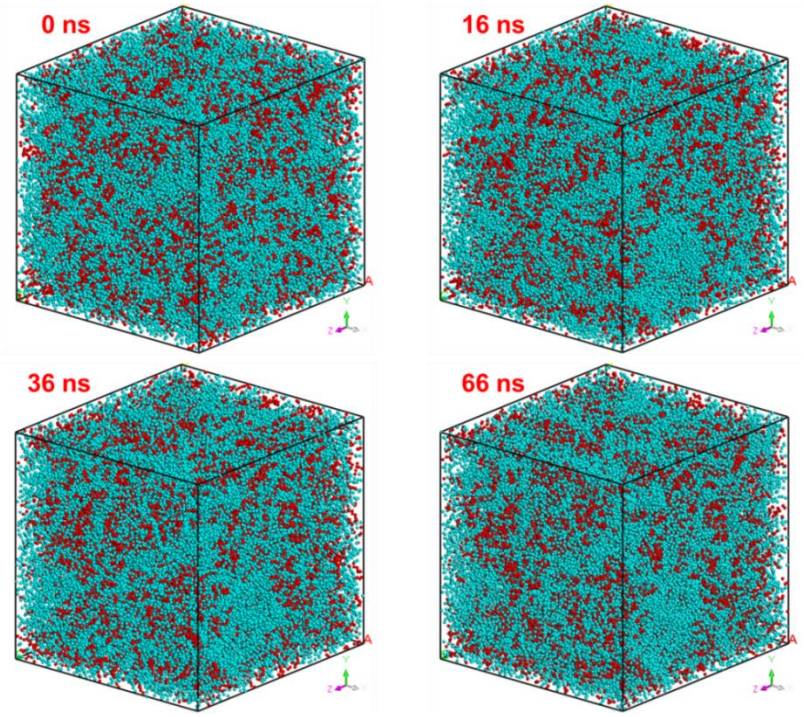

Figure 33. Snapshots of coarse-grained MD simulations of P3HT:PCBM bulk heterojunction (P3HT:cyan beads; PCBM:red beads) after thermal treatment of 450 K for 0ns, 16ns, 36ns and 66ns. While limited clustering of P3HT and PCBM can be observed, clear phase separated structure is expected to form with time-scale approximately 10 times of the current production run according to recent publication.[62] Since it is unrealistic for our existing hardware capability, MC simulation was employed to obtain the final phase-separated morphology relevant for continuum device level simulations.

The obtained 10% volume fraction of P3HT domains is far from the expected 50% for complete phase separation, which implies that the system has not yet reached equilibrium. This is confirmed in the curve of potential energy profile versus of simulation time in Figure 34b. In a recent publication, Carrillo et al.[62] estimated, on the basis of a massively coarse-grained dynamics simulations, that the P3HT:PCBM phase separation process takes place through 3 stages with stage 1 from 0-60ns, stage

2 from 60-160ns and stage 3 from 160 ns onwards. Since the coarse-grained forcefield utilized in Carrillo et al.'s work is about 4 times coarser than our forcefield, which corresponds to a faster dynamics (c.f. Section 2.3.4), we expect that the current run is still well within the first stage of the morphological evolution.

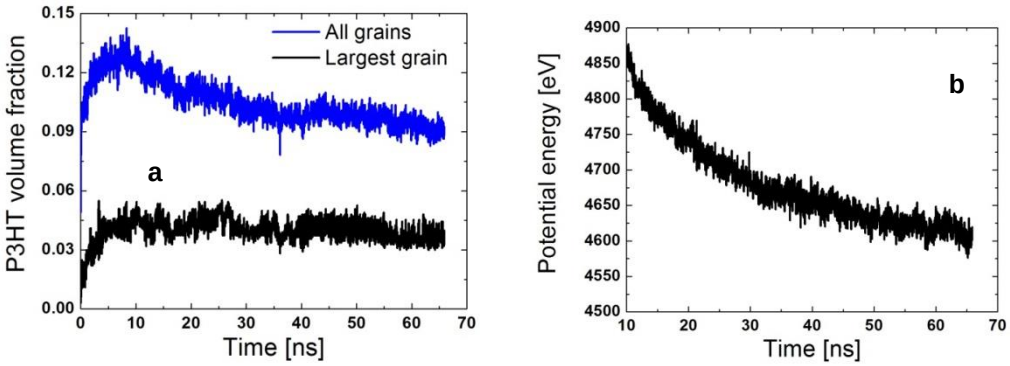

Figure 34. (a) Changes of volume fraction of P3HT domains as a function of simulation time (Blue line: all grains; Black line: the largest grain). This curve is calculated by dividing the unit cell into cubes of (2nm)^3 dimension. Grids with P3HT weight fraction of >80% are considered P3HT domains.
(b) Potential energy profile of P3HT:PCBM bulk heterojunction as a function of simulation time for the last 56 ns. The reducing potential energy even after 66 ns signifies that the system has not yet reached equilibrium.

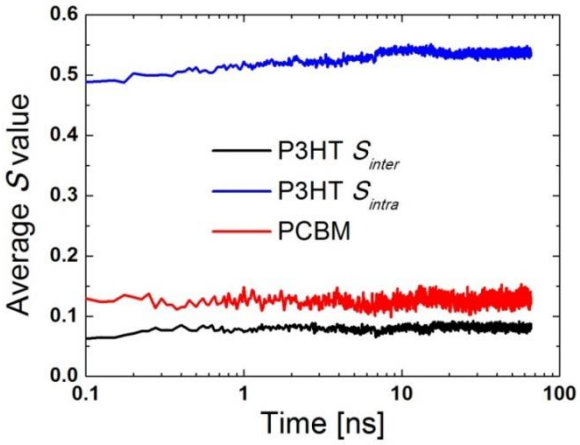

Figure 35. Changes of orientational order parameter S as a function of simulation time with black and blue line representing S_{inter} and S_{intra} respectively in P3HT and red line representing PCBM

While it is not feasible to achieve the time scale comparable to that of Carrillo et al.'s work (approximately 400 ns), partly due to the hardware capability limitation and the higher computational demand of our more detailed forcefield, the retention of the side chains on both P3HT and PCBM in our coarse-grained forcefield allows us to capture more faithfully the phase separation process especially in conjunction with the changes of crystallinity versus time which in Section 2.3.5 we established as one of

the most important factors. The profile of S_{inter} and S_{intra} and orientational order parameter for PCBM as a function of simulation time is shown in Figure 35. Here the only obvious variation is the increase of S_{intra} as a function of time. This means that the P3HT chains are straightening up during the simulation. Hypothetically, this process should be followed by P3HT crystallization in which S_{inter} will start to rise; PCBM concentration in the vicinity will decrease leading to formation of P3HT domains. However, since such a time scale to achieve significant phase separation has not been reached, due to aforementioned reasons, to solicit the morphology of P3HT:PCBM bulk heterojunction after the thermal annealing process, MC simulation was performed which made use of energetic information obtained from coarse-grained dynamics simulations. The detailed methodology and results are discussed in Section 2.4.

2.4. Monte Carlo Simulation[120]

2.4.1.Methodology

The purpose of MC simulation in this work is to reduce the computational effort required in obtaining the morphology of P3HT:PCBM bulk heterojunction. To this end, the simulation would focus on soliciting the final morphology based on the energetics information obtained from coarse-grained dynamics simulations and statistical distributions or system entropy. In short, MC simulation aims to minimize the Gibbs free energy of the system expressed following Equation 3.15, where G is the Gibbs free energy of the system; H and S are the system enthalpy and entropy respectively; T is the system temperature; k_B is the Boltzmann constant and Ω is the degeneracy of the current state.

$$G = H - TS = k_B T\, ln(\Omega) \tag{3.15}$$

In order to minimize the Gibbs free energy of the system, we first allow the system to evolve randomly into any trial state. The change of energy of the evolution would

determine if the trial state would be accepted according to Equation 3.16 where ΔE is the change of system energy caused by accepting the trial state as the new state and $rand$ is a random number in the interval [0,1].

$$\exp\left(\frac{-\Delta E}{k_B T}\right) > rand \tag{3.16}$$

The system of interest in this simulation is a (100 nm)^3 cube which is made up of (2 nm)^3 grid elements and periodic in the **x** and **y** directions only. This is to mimic actual OPV cells where the active layer thickness is about 100 nm whereas the lateral dimension could be of centimetres scale. Each of the grid elements in the cell is characterised by a number in [0,1] that is representative of the P3HT weight fraction in the grid element.

The evolution at each step of the calculation is done in the following steps:

1. Randomly select two grid elements, which have P3HT weight fraction values of A_0 and B_0.

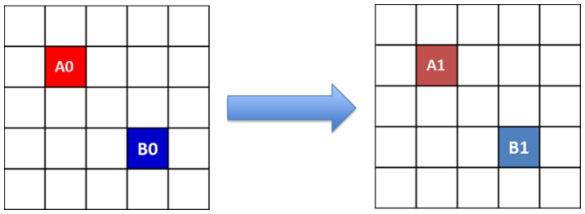

2. Assign two new random P3HT weight fraction values A_1 and B_1 to the chosen grid elements such that the following conditions are met:

$$\begin{cases} A_1 + B_1 = A_0 + B_0 \\ 0 \leq A_1 \leq 1 \\ 0 \leq B_1 \leq 1 \end{cases}$$

3. The change in system energy is then calculated according to the Equation (3.17) where $E(L)$ is computed using Equation (3.14) and A^i, B^i are the weight fraction values of the surrounding grid elements that share at least one face with the selected elements. The scaling factor of 4 is because each grid surface has a

dimension of (2 nm)^2 while $E(L)$ is the interfacial energy per square nanometre. $E(L)$ is raised to the third power in Equation (3.17) because its value has been computed (using coarse-grained dynamics) for the changes in domain size in a single direction. In our MC simulations, where the domain size changes may occur in all three **x**, **y** and **z** directions, $E(L)$ should be raised to the third power to accommodate such a difference.

$$\Delta E = 4\big(E(L)\big)^3 \left[\sum_i \left|A_1 - A^i\right| - \sum_i \left|A_0 - A^i\right| + \left(\sum_i \left|B_1 - B^i\right| - \sum_i \left|B_0 - B^i\right|\right)\right] \quad (3.17)$$

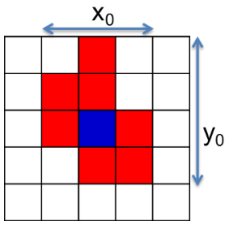

The domain size L in Equation (3.17) is estimated at each evolution step following the schematic on the left hand side in which the blue grid element is the chosen element and the red ones are the elements that belong to the same domain as the selected one. Draw three straight lines through the selected grid such that they are parallel to the **x**, **y** and **z** directions. Suppose the number of grid elements that are still in the same domain as the selected one are x_0, y_0 and z_0 corresponding to the drawn lines parallel to the **x**, **y** and **z** directions, respectively. The domain dimension is then approximated as $L = 2 \times \sqrt[3]{x_0 \cdot y_0 \cdot z_0}$. Again the factor of 2 used here is because each grid element is of 2 nm in width. While this may be not the most accurate method to estimate the domain size dimension, it is robust and computationally efficient, allowing us to achieve Gibbs energy minimized state in acceptable time scale that is otherwise not feasible with coarse-grained dynamics method.

The biggest advantage of MC simulation is its significantly reduced computational cost compared to typical coarse-grained dynamics method. The code is serial and can be executed on any personal computer with a minimal amount of memory required, yet convergence can be obtained in a matter of weeks compared to months or even years using coarse-grained dynamics method running in parallel on high-end

computing servers. The downside of the technique is the lack of molecular interaction details that would have been achievable with MD simulations. This is important especially when it comes to crystallization of P3HT, which (as we have shown with coarse-grained dynamics simulations) is pre-requisite to the phase separation process. P3HT crystallites, as most polymeric crystallites, are known to exhibit strong anisotropy. Thus P3HT crystals assume a typical thickness of approximately 20 nm and lateral dimensions of up to a few hundred nanometres.[101] For our MC simulation, however, phase separated domains follows isotropic domain coarsening which may not be representative of typical morphology found in the active layer of bulk heterojunction OPV.

2.4.2. Results and Discussions

2.4.2.1. Morphology Evolution

Using the MC method as discussed we studied morphological evolution in P3HT:PCBM bulk heterojunction at different initial conditions. This includes fully blended initial morphology at different P3HT weight ratio of 0.2, 0.35, 0.5, 0.65 and 0.8; and bilayer P3HT:PCBM at 0.5 P3HT weight ratio. An illustration of these initial conditions can be seen in Figure 36. Initial P3HT weight fractions of the individual grid elements were set to follow Gaussian distribution with the average value matching that of the weight ratio under investigation and a standard deviation of 0.05 (except for bilayer case) in order to simulate the high entropy states that can be expected to manifest in blended structures. The temperature at which the morpholgical evolutions took place was set at 450 K for all MC simulations (c.f. Equation 3.16) because this is the temperature at which the interfacial energy profile, the backbone of this MC simulation, was calculated (c.f. Figure 29).

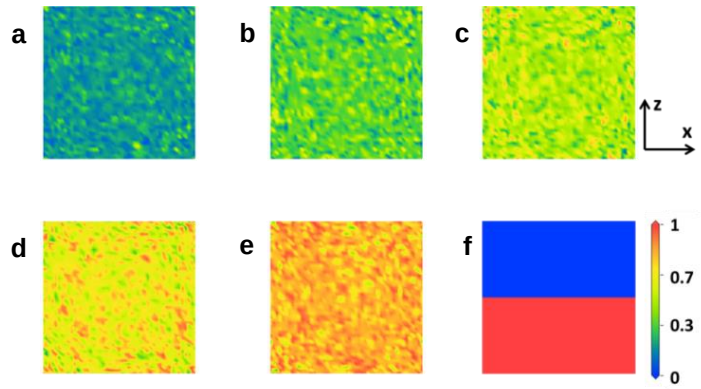

Figure 36. Different initial morphologies of P3HT:PCBM blend studied using MC simulations include fully mixed morphology with P3HT weight fraction of (a) 0.2, (b) 0.35, (c) 0.5, (d) 0.65 and (e) 0.8; and (f) bilayer P3HT PCBM at 0.5 P3HT weight ratio. Colours represent P3HT weight fraction according to the right-hand side legend.

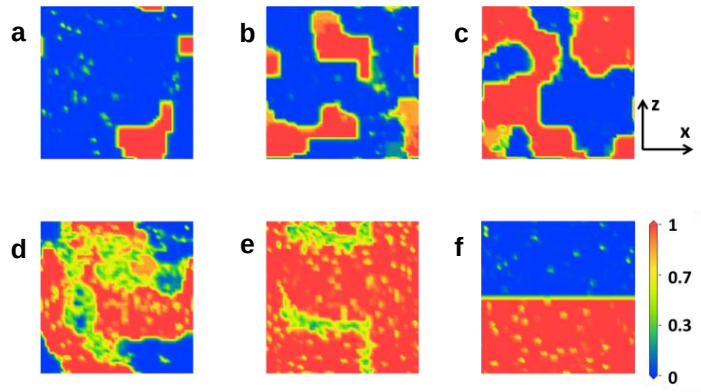

Figure 37. Morphologies of P3HT:PCBM blend at blend ratios of (a) 0.2, (b) 0.35, (c) 0.5, (d) 0.65 and (e) 0.8; and (f) bilayer P3HT PCBM at 0.5 P3HT weight ratio after 1,500 million MC cycles. Effective phase separation of ~ 98% of total cell volumes was observed for all cases.

The cross-section areas of P3HT:PCBM blends at different weight ratios after 1,500 million MC simulation cycles are shown in Figure 37. An inspection of the complete volume shows that the blend ratio of 1:1 produces balanced percolating volumes for both donor and acceptor. In contrast, blends with P3HT weight ratio of 0.2 and 0.8 form small isolated islands, hence are expected to lead to suboptimal charge percolation conditions. From Figure 38a showing the evolution of phase separated P3HT volume as a function of simulation cycles, it is clear that after 1,500 million cycles near-complete phase separation has been achieved. In fact, approximately 98% of total cell volumes are recorded to be of "pure" P3HT or PCBM phase (i.e. ≥80% pure) for all blend ratios after 1,500 million cycles. Figure 38b shows the evolution of the biggest P3HT domain as a function of simulation cycles which suggests that for

P3HT weight fraction ≥0.5, the biggest P3HT domain comprises almost all of the phase-separated P3HT. In fact the percentages of phase-separated P3HT joining the biggest domain are >98% for P3HT weight fraction of ≥0.5, 58% and 0.5% for P3HT weight fractions of 0.35 and 0.2 respectively. Results for PCBM phase are similar and hence not presented here.

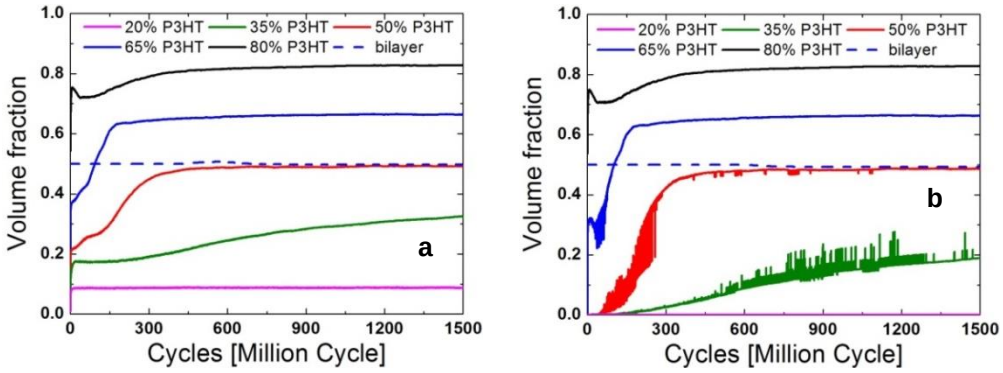

Figure 38. Evolution of (a) total volume fraction of P3HT domains (i.e. of elements with P3HT weight fractions ≥0.8) and (b) volume of largest P3HT domain as a function of simulation cycle number for different P3HT weight ratios and for the P3HT:PCBM bilayer at 0.5 P3HT weight ratio.

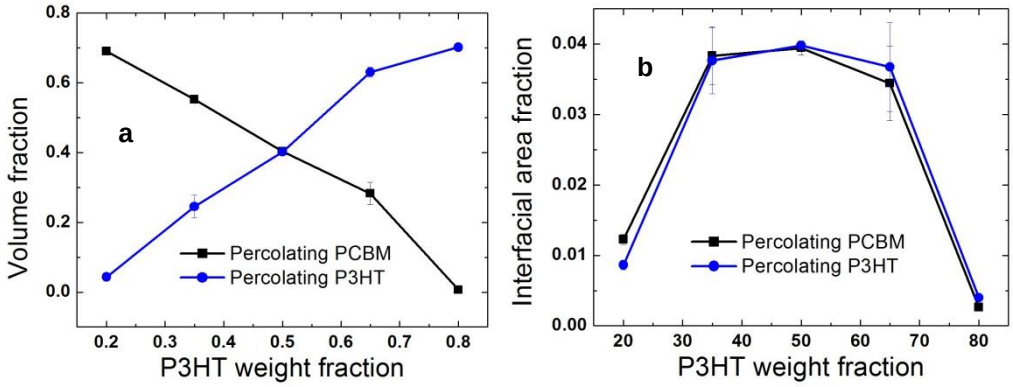

Figure 39. (a) Volume fraction of percolating volume and (b) P3HT:PCBM interfacial areas of percolating domains for both P3HT and PCBM as a function of P3HT weight fraction.

While it is desirable that most of the phase separated P3HT volumes are congregated into a single P3HT domain at large P3HT weight fraction (≥0.5), an increase in the percentage of percolating volume for both donor and acceptor is needed to improve charge transport and charge collection, as well as to reduce charge recombination and ultimately enhanced device efficiency. While the presence of a single bicontinuous domain would increase the chances of forming distributed percolating pathways in the blend, it may not result in such morphology. On the other hand, large interfacial

areas between donor and acceptor phases are also desirable for enhanced exciton separation rate and short-circuit current (J_{SC}). To assess the blend suitability for OPV performance, we computed the percolating volume and interfacial areas of percolating domains for both donor and acceptor as a function of P3HT weight ratio (c.f. Figure 39). These graphs are averaged over 3 different runs and the error bars for each blend ratio configuration are also presented.

The graph of percolating volume as a function of P3HT weight fraction (c.f. Figure 39a) suggests that a balanced percolating volume is found in both the acceptor and donor phase at P3HT weight fraction of 0.5. On the other hand, a maximal interfacial area between percolating donor and acceptor (c.f. Figure 39b) is achieved at P3HT weight fraction from 0.35-0.65. This suggests that a blend ratio of 1:1 is optimal for P3HT:PCBM blend relevant for bulk heterojunction OPV. This result is in good agreement with coarse-grained MD simulations where a blend ratio of 1:1 result in a balanced percolation ratio for both P3HT and PCBM.[84] Analogous results obtained from experimental techniques, however, are not available at the time of this report as it is still beyond the state-of-the-art experimental capacity.[84]

Similar analysis done on bilayer system yields a percolating volume fraction of 0.49 and an interfacial area of percolating volume fraction of ~ 0.007 for both P3HT and PCBM. This means that while balanced charge percolation is achieved for both donor and acceptor, low interfacial area between percolating domains makes bilayer P3HT:PCBM a weak solar absorber and an inefficient photovoltaic device. This conclusion, however, is only applicable to the case of single crystal P3HT layers as the MC simulation assumes that each P3HT domain is fully crystalline (by employing the interfacial energy of the face-on crystalline P3HT:PCBM interfaces). Experimentally, most annealed bilayer P3HT:PCBM would assume bulk heterojunction morphology due to the diffusion of PCBM along amorphous P3HT regions.[61, 74] Hence, we expect that bilayer P3HT:PCBM device with a high level of

crystallinity within the respective layers would not form desirable bulk heterojunction structure upon thermal treatment and is not an ideal candidate for photovoltaic applications.

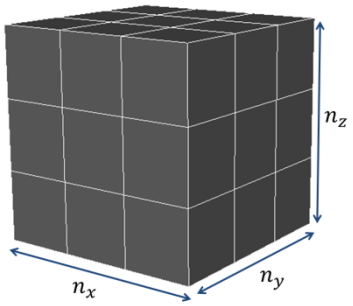

In addition to the percolating pathways, sizes of phase separated domains also play a role in the device performance. As exciton diffusion length of P3HT is known to be approximately 10 nm,[121] domain size of 10-15 nm would induce effective exciton dissociation and charge collection (as for this thickness range an excitation generated at a random position has a ca. 40-60% chance of reaching an interface within 10 nm when travelling in a random direction). Larger domains lead to high probability of exciton decays while smaller domains would minimize the formation of charge percolating pathways. To compute the size of the separated domains formed during the MC simulations, we consider the following scenario:

Suppose we have a three dimensional rectangular grid which made up of cubic grid elements of size a nm. The extent of the grid in **x**, **y** and **z** directions are represented by n_x, n_y, and n_z (this is illustrated in the picture on the right). The volume and surface area of the rectangle grid can be expressed as followed:

$$Volume = a^3(n_x n_y n_z)$$

$$Surface\ area = 2a^2(n_x n_y + n_y n_z + n_x n_z)$$

Suppose that the size of such a three dimensional rectangle is determined by the smallest extension in **x**, **y** and **z** directions. Thus the size[b] of the rectangle (representing the domain thickness) can be expressed as followed:

[b] Note that 'size' in this context refers to the domain thickness or the distance from one domain wall to the opposite one from this point to the end of the chapter unless otherwise

$$size = a\alpha$$

where

$$\alpha = \min(n_x, n_y, n_z)$$

Suppose that we have the following relation with k as a constant:

$$size = \frac{Volume}{Surface\ area} \cdot k$$

$$\Rightarrow k = 2\alpha\left(\frac{1}{n_x} + \frac{1}{n_y} + \frac{1}{n_z}\right)$$

$$\Rightarrow size = \frac{Volume}{Surface\ area} \cdot 2\alpha\left(\frac{1}{n_x} + \frac{1}{n_y} + \frac{1}{n_z}\right) \quad (3.18)$$

In this work, Equation (3.18) was employed to compute the size of the phase-separated domains. From Equation (3.18), it is clear that for 3-dimensional ($n_x \approx n_y \approx n_z$), 2-dimensional ($n_x \ll n_y; n_y \approx n_z$) and 1-dimensional ($n_x \approx n_y$; $n_y \ll n_z$) structures, $k =$ 6, 2 and 4 respectively. To estimate the size for the phase separated domains obtained from MC simulation, first we need to determine their dimensions then k is estimated by using Equation (3.19) in which d is the dimension of the domain.

$$k = d^3 - 3d^2 + 6 \quad (3.19)$$

Equation (3.19) is obtained by fitting the k value for $d =$ 1, 2, 3 and an additional condition that a turning point should be observed at $d =$ 2 against a third power polynomial. To understand the last condition, we first take the right- and left-hand limit of k (without loss of generality supposed that $\alpha = n_x$).

$$\lim_{d \to 2+} k = 2\alpha\left(\frac{1}{n_x} + \frac{1}{n_y} + \frac{1}{n_z}\right) = 2\left(1 + \frac{n_x}{n_y} + \frac{n_x}{n_z}\right)$$

stated. This value is relevant for the shortest distance that the excitons must travel before it reaches the interface.

Since $d > 2$ this means that n_x gets progressively larger with respect to n_y and n_z. Thus:

$$\frac{n_x}{n_y} > 0 \; and \; \frac{n_x}{n_z} > 0$$

$$\Rightarrow k > 2$$

The left-hand limit of k:

$$\lim_{d \to 2-} k = 2\alpha\left(\frac{1}{n_x} + \frac{1}{n_y} + \frac{1}{n_z}\right) = 2\left(1 + \frac{n_x}{n_y} + \frac{n_x}{n_z}\right)$$

Since $d < 2$ this means, without loss of generality, that as d shrink towards 1-D n_y gets progressively smaller compared to n_x:

$$\frac{n_x}{n_y} > 0 \; and \; \frac{n_x}{n_z} = 0$$

$$\Rightarrow k > 2$$

Since both the left- and right-hand limits of $k(d = 2)$ are larger than 2, it is necessary that $k(d = 2)$ must be a minimum. The dimensions of the phase separated domains are obtained by first selecting a random grid element within the domain followed by determining the number of grid elements within the same domain as a function of distance from the selected grid element. The process is repeated until about 1% of the total number of grid elements has been sampled. The results of grid elements as a function of distance from the chosen grid element are then collectively summed together where the slope of the respective log-log plot is used to determine the domain dimension (c.f. Figure 40a and b).

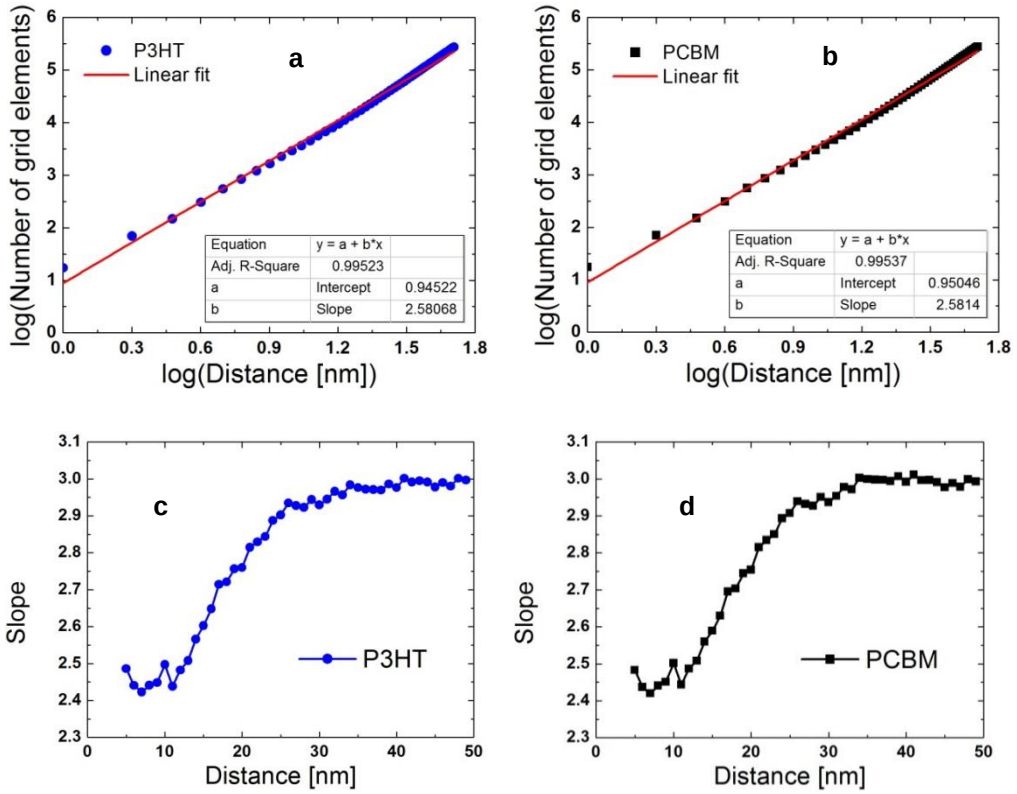

Figure 40. The log-log plot of the number of grid elements in the largest domain as a function of distance from the domain centroid for (a) P3HT and (b) PCBM. Both plots were computed from the 1,500 million cycles of the 1:1 blend ratio run. Upon closer inspection it can be observed that 2 distinct slopes could be obtained from the log-log curve for (c) P3HT and (d) PCBM domains. Thus to determine the dimension of the respective domains, an iterative algorithm was employed in which an initial trial dimension value is assumed.

Figure 40a and b shows the log-log distribution as well as the linear fit across all data points for both P3HT and PCBM computed from the corresponding largest domains relevant for case of 1:1 blend ratio after 1,500 million cycles of MC simulations. Upon close inspection of the log-log curve, it becomes clear that there are three discernable regimes: the lower dimension regime which manifests at small distances (< 15 nm), a higher dimension regime which is observed at large distances (> 30 nm) and an intermediate which is the transition between the lower and higher dimension regimes. Thus in order to determine the domain size, an iterative algorithm was employed. The algorithm starts by assuming a trial dimension in order to compute the hypothetical domain size according to Equation (3.18) which is then compared with the graph of dimension versus distance (c.f. Figure 40c and d) to obtain new dimension value. The process is repeated until convergence is achieved.

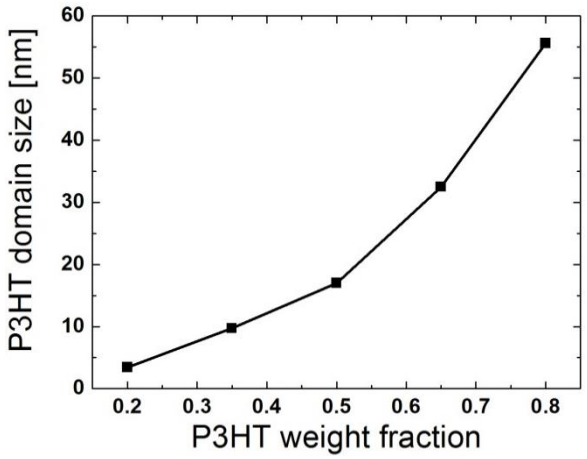

Figure 41. Graphs of changes of domain size of largest P3HT domain as a function of P3HT weight fraction computed for MC simulation snapshot after 1,500 million cycles.

Using the computed dimension value described above, we can then identify the size of largest domain for P3HT as a function of blend ratio relevant for the phase separated MC simulation snapshot (after 1,500 million cycles) (c.f. Figure 41). Since P3HT weight fractions from 0.35 to 0.50 yield P3HT domain of 9.7 – 17 nm close to the ideal values discussed above. Note that while the P3HT domain size at weight ratio of 0.35 appears to be more favourable than at weight ratio of 0.50 (9.7 nm at 0.35 vs. 17.0 nm at 0.5), PCBM domain size at 0.35 is much larger than the optimal range (28.5 nm at 0.35 vs. 16.0 nm at 0.5).Hence, in order to achieve domain size close to the optimal range for both donor and acceptor, blend ratio of 1:1 is preferred. P3HT weight ratio of 0.2, 0.65 and 0.8 yield domain sizes of 3.4 nm, 32.5 nm and 55.6 nm respectively which are too small (for the case of 0.2) or too large (for the case of 0.65 and 0.8). Combining this result and the percolating pathway analysis presented above, we conclude that optimal P3HT:PCBM OPV should be made by thermal annealing of blended P3HT:PCBM at blend ratio 1:1.

2.4.2.2. P3HT Seed Crystals

So far we have discussed the control macroscopic morphology in P3HT:PCBM device via tuning of blend ratio. However, by just changing the blend ratio, it is not possible to accurately control the microscopic layout of the active layer morphology.

Experimentally, columnar phase-separated structures can be engineered by mixing stoichiometric cross-linking agents into the blend which would form a scaffold for PCBM molecules.[23] This method, however, depends on the chemistry of the polymeric donor materials since appropriate cross-linking agent must be available that does not interfere with the performance of the device in both light absorption and charge transport efficiency. Alternatively, the active layer morphology can be carefully controlled using expensive atomic layer deposition technique which not only raises the manufacturing cost but also does not improve the overall efficiency.[122]

Here we try to investigate the feasibility of employing induced P3HT seed crystallites prior to the thermal annealing process as a mean to control the resultant active layer morphology. This is done by creating P3HT seed crystals (by giving certain grid elements initial value of 1) in various patterns at the bottom contact while keeping the overall blend ratio of 1:1 which, as we has shown previously, can produce morphology of good percolation volume, high interfacial areas of percolating domains and phase separated domains of optimal sizes. Beside the seed crystal regions, other grid elements assume values following Gaussian distribution as discussed in previous MC simulation runs.

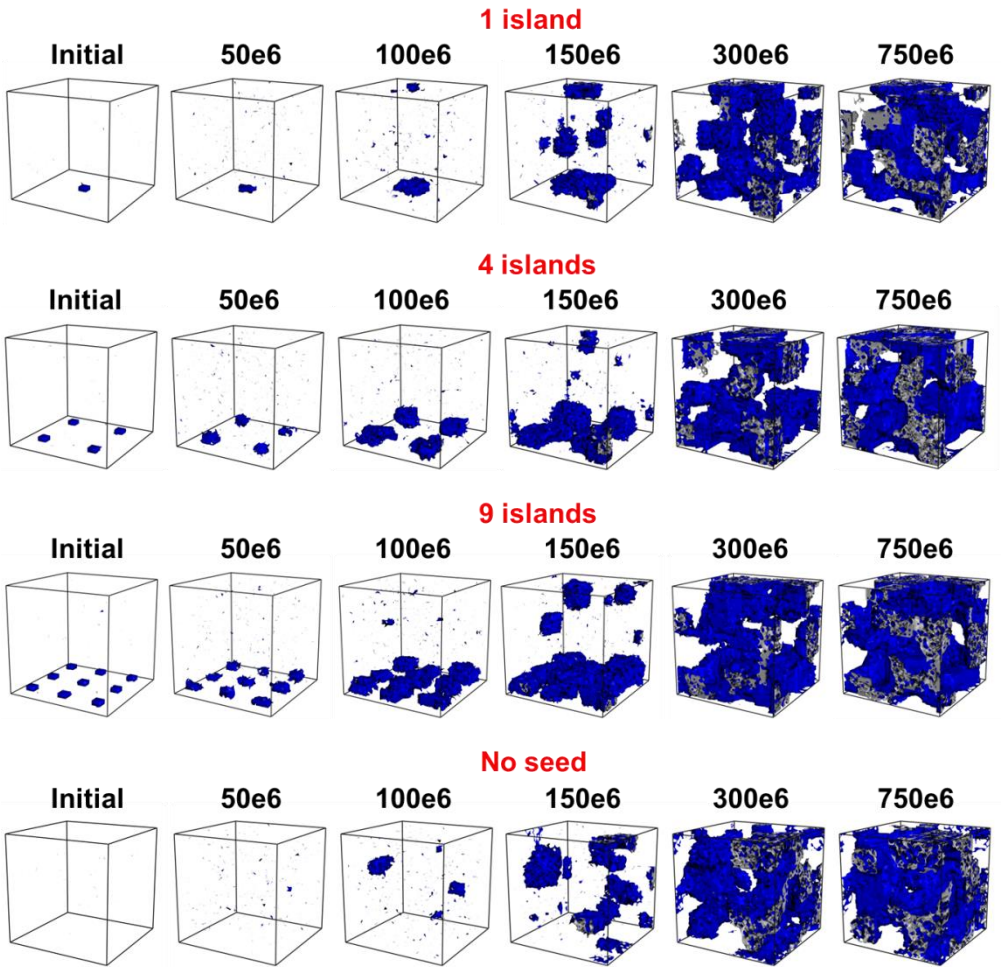

Figure 42. Illustration of P3HT domains evolution at different MC simulation cycles (initial condition, 50, 100, 150, 300 and 750 million cycles) for the case of 1 seed, 4 seeds, 9 seeds and no P3HT seed crystal.
All systems assume blend ratio of 1:1.

The snapshots of the MC runs at different cycles with initial P3HT seeding of 1 island, 4 islands and 9 islands patterns can be seen in Figure 42. The no seed case was also added for comparison. In all cases, the initial size of each island is $(10\ nm)^3$. We can see that for all cases, phase separation in early stages is much more rapid around the seeding regions as nucleation is not needed. Nevertheless, after 750 million cycles, the morphologies of the seeded and non-seeded cases at first sight appear similar. Figure 43 shows alternative line seeding patterns each with width of 10nm and height of 10nm. Similar to the island seeding case, it during the early stages phase separation is more rapid in vicinity of the seeds. As the simulation progresses,

resultant morphologies of both seeded and non-seeded case appear similar by visual inspection.

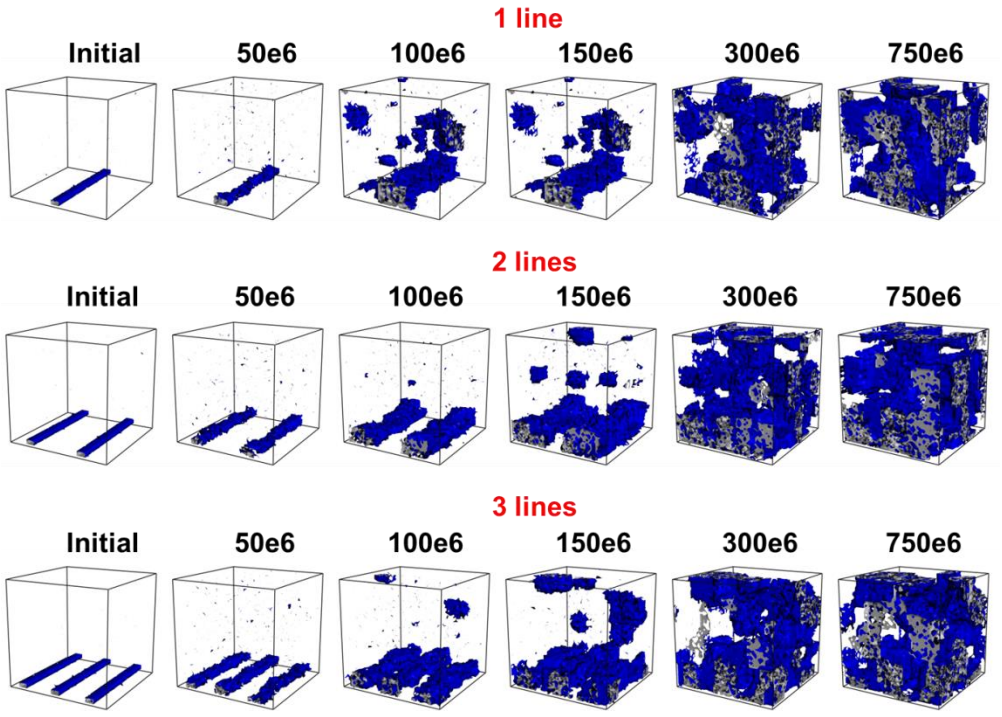

Figure 43. Illustration of P3HT domains evolution at different MC simulation cycles (initial condition, 50, 100, 150, 300 and 750 million cycles) for the case of 1 line, 2 lines and 3 lines of P3HT seed crystal.
All systems assume blend ratio of 1:1.

	Seed packing density	P3HT volume fraction	P3HT domain size	P3HT domain dimension	Percolating volume P3HT	Interfacial area of percolating P3HT
No seed	0	0.48	13.90	2.58	0.49	0.049
1 line	0.1	0.48	19.15	2.71	0.48	0.044
2 lines	0.2	0.48	20.17	2.78	0.48	0.049
3 lines	0.3	0.48	19.00	2.75	0.48	0.044
1 island	0.01	0.48	13.62	2.52	0.47	0.046
4 islands	0.04	0.49	13.66	2.50	0.49	0.048
9 islands	0.09	0.49	20.08	2.76	0.49	0.048

Table 8. P3HT phase separated volume, domain size, dimension, percolating volume and interfacial area of percolating domains for the seeded (with 1 line, 2 lines, 3 lines and 1 island, 2 islands, 3 islands) and non-seeded case. All systems assume 1:1 blend ratio. Strong resemblances (except for the domain size) between the seeded and non-seeded cases are observed for all listed parameters.

The key phase-separated morphology parameters of the seeded and non-seeded case are compared in Table 8. Except for the domain size and dimension, there are strong

resemblances between seeded and non-seeded cases in term of P3HT phase-separated volume, percolating volume and interfacial area of percolating volume. On the other hand, different seed patterns produce near identical results except for the domain sizes. This suggests that seeding does improve the overall charge percolation in the active layer due to the slightly larger domain sizes and higher fractional domain dimensionality especially in the cases of denser seed patterns (line seeding and 9 islands or seed packing density of ~10%). Increment of seed packing density beyond 10% does not seem to lead to any further enhancement of domain size. Since seeding pattern does not seem to play a critical role (as compared between line and island seeding), uniformly distributed seed packing density of appears ~10% required to achieve the enhancement of domain size and charge transport pathway dimensionality. In addition, the more rapid phase separation as seen in the early stages of the simulations and the resultant larger phase-separated domains of the seeded cases compared to the non-seeded one indicate that there should be higher concentrations of P3HT at the bottom contact where the seed crystals were placed. To investigate this, we conducted a depth profiling of P3HT weight fraction along the z-axis (which is the non-periodic axis that is perpendicular to the contact planes) for both the seeded and non-seeded cases. The results are shown in Figure 44.

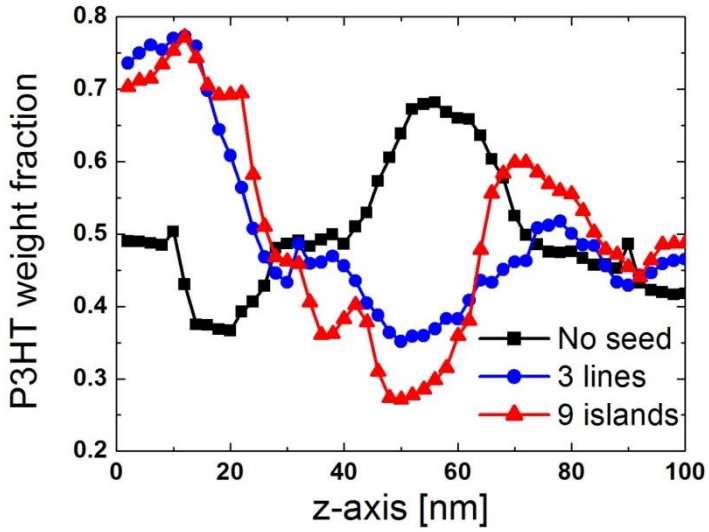

Figure 44. P3HT weight fraction profiling along the z-axis of the active layer for the non-seeded and seeded (3 lines and 9 islands) cases. The profile suggests a tri-layer morphology which is found in both seeded and non-seeded cases. While it is possible for a morphology flip in the non-seeded case (from donor:acceptor:donor to acceptor:donor:acceptor) due to the isotropy of the system, it is much harder in the seeded case. This is due to rapid crystal growth in vicinity of the seed during initial stage which would provide pining of the bottom layer phase. This means determined tri-layer morphology can be engineered.

The depth profiling (c.f. Figure 44) shows discernable tri-layer morphology distributions along the z-axis for both the seeded and non-seeded cases. For the non-seeded case, nucleation occurs at a random position and in the displayed simulations high P3HT concentrations are observed in the middle of the cell while low P3HT concentrations (or high PCBM concentrations) are detected nearer to the contacts. For all the seeded cases a maximum of the P3HT concentration is preserved at the surface.[c] Nevertheless, in all cases, tri-layer morphologies (donor:acceptor:donor or acceptor:donor:acceptor) are observed. P3HT concentration profiling along the x-axis and y-axis do not yield any discernable stratification. Such phase segregations along the z-axis is due to the system energy minimisation according to the interfacial energy profile (c.f. Figure 29) leading to the maximisation of both the interfacial area and the domain size. By having tri-layer morphology along z-axis, domain size is maximised due to the prospect of infinitely long domains. Furthermore, interfacial areas between donor:acceptor is enhanced due to the concentrated interface regions located in the

[c] In Figure 44, only the results of "3 lines" and "9 islands" are shown for clarity of comparison against the non-seeded case. The same calculations performed on other seeded systems yield similar results and are not reported here.

vicinity of the top and bottom contacts. Note that for the non-seeded cases this morphology only becomes more evident for extensive simulations (~ 3,500 million cycles), long after the presented parameters such as domain size, percolation volume, etc. stabilise. In actual experimental setup, this means extended thermal treatment may be needed before such structure can be observed. However, if seed crystals are present before the annealing process, such tri-layer morphology is achievable after much shorter simulations (~ 800 million cycles). Thus if the production of such a tri-layer morphology is desirable (as we shall see later on), seeding proves superior due to the expected much shorter required annealing time.

Due to the isotropy of the simulation (donor and acceptor are interchangeable in the calculation because they follow the same interfacial energy profile), the tri-layer morphology in the non-seeded case is switchable between donor:acceptor:donor and acceptor:donor:acceptor morphology. This is undesirable in OPV devices where high concentration of donor material is expected near the bottom contact (hole transport layer) in the conventional device architecture (c.f. Figure 4a). This random swapping of morphology between possible tri-layer configurations reduces the chance of forming the ideal phase at the bottom contact and the reproducibility of the device efficiency. Inducing small P3HT seed crystals at the bottom contact before the annealing process overcomes this problem by reliably pinning a P3HT phase domain to the bottom side of the active layer. As seen in Figure 42 and Figure 43. The rapid P3HT domain growth in the vicinity of the P3HT seed crystals ensures that the active layer at the bottom contact is predominantly P3HT throughout the simulations. As a result all seeded cases assumed a donor:acceptor:donor morphology.

On the other hand, the tri-layer morphology itself minimizes the chance of forming a desirable concentration gradient where high concentration of donor and acceptor material should be found at opposite contacts (high donor concentration at the bottom contact and high acceptor concentration at the top contact for conventional OPV

architecture). One way to theoretically overcome this problem would be by dissecting the tri-layer blend into half which in all cases (especially the "3 lines" and "9 islands" seeded cases) possess a desirable concentration gradient relevant for high performance OPV as discussed above.

Thus, we suggest, based on the result obtained from MC simulations, that a P3HT:PCBM OPV active layer should be fabricated with blend ratio of 1:1, induced uniformly distributed P3HT seed crystals (packing density of ~10%) and a thickness of approximately 200 nm (twice the usual active layer thickness). This is followed by thermal annealing and dissection of the active layer into half, the remnant of which would have good concentration gradient, domain sizes, and domain percolation suitable for OPV applications. Alternatively, we can seed PCBM crystal at the top contact (in addition to seeding P3HT crystals at the bottom contact). Since crystal growth in the vicinity of the seed crystals is much more rapid since nucleation is not needed, active layer regions near the contacts would then have the desirable phases. This method requires more in-depth evaluations from both experimental and theoretical approaches.

2.5. Chapter Summary

In this chapter we have studied the physics underlying the morphological evolution process of P3HT:PCBM bulk heterojunction and proposed ways to control or produce optimal active layer morphology. The analysis was carried out using a multi-scale modelling approach starting from atomic scale MD, DFT to coarse-grained MD and finally MC simulations which approach experimental device level dimension. We first adapted reported atomistic forcefields by benchmarking them against our accurate DFT calculations. The adapted forcefields were validated against experimental melting temperatures and density. Coarse-grained forcefields are then derived based on the atomistic ones employing a coarse-graining scheme determined

from the all-atoms MD simulations. Using the coarse-grained forcefields, we calculated the interfacial energy between P3HT:PCBM as a function of underlying P3HT layer thickness and used it as a basis for MC simulations.

Coarse-grained forcefield was utilised for studies of P3HT:PCBM interface at different P3HT orientations. Crystalline P3HT are shown to form more stable interface with PCBM while face-on is most energetically favourable among the crystalline P3HT configurations. This is consistent with our finding that P3HT crystallinity is more prominent in the vicinity of a P3HT:PCBM interface. By studying the system energy changes as coarse-grained C_{60} bead is inserted into P3HT layers, we concluded that PCBM diffusion into crystalline P3HT is confined to grain boundary diffusion while PCBM diffusion into amorphous P3HT is via chain activation. This led us to suggest a phase separation model of P3HT:PCBM bulk heterojunction which starts with nucleation crystallisation of P3HT followed by diffusion of PCBM along the P3HT grain boundary and amorphous regions into the PCBM-rich regions.

MC simulations allow us to study the morphology evolution in $(100\ nm)^3$ cell which extends infinitely in the **x** and **y**, hence, is a faithful replica of the active layer in typical experimental OPV devices. The study of different blend ratios reveal 1:1 as the most optimal choice due to the favourable domain sizes, balanced volume and interfacial area of percolating domains for both donor and acceptor. Phase separated active layer is also shown to favour tri-layer morphology along the z-axis. Besides enhancing the domain size, P3HT seed crystals at the bottom contact are found pin the P3HT domain to the bottom contact ensuring that the active layer would follow a donor:acceptor:donor tri-layer morphology. The seeding pattern does not seem to have any critical influence on the morphology. Based on these results, we suggested P3HT:PCBM OPV active layer to be made with 1:1 blend ratio, induced uniformly distributed P3HT seed crystal (with packing density of ~10%) and thickness of ~200

nm. This should be followed by thermal treatment and dissection of the active layer into half, the remnant of which would have domain size, domain percolation and P3HT concentration gradient ideal for OPV application. Alternatively both P3HT and PCBM seed crystals can be incorporated into the bottom and top contact respectively prior to thermal annealing. Since crystal growth is more rapid in vicinity of the seed crystals we expect alternate seeding from both top and bottom contact would induce favourable concentration gradient within the active layer. This method needs a more careful assessment from both experimental and theoretical point of view.

The framework established in this section combining DFT, MD, coarse-grained MD and MC simulations can be used for similar morphology evolution studies of active layer in other OPV systems.

CHAPTER 3: Charge Transport in Conjugated System

3.1. Literature Review

One major disadvantage of organic semiconductors is the suboptimal charge transport capability as compared to their inorganic counterpart (c.f. Section 1.2.2). Nevertheless, finding a suitable chemical composition that could boost device performance proves to be difficult due to the lack of readily available theoretical frameworks which stems from poor understanding of the device physics. Unlike inorganic semiconductors which are typically fully crystallised, organic semiconductors consist of both nanocrystalline and amorphous regions whose actual morphology is a complex function of temperature, pressure, molecular weight, region-regularity and so on, hence, preventing meaningful application of established theories.[123] One approach to model such a system is through empirical continuum theories such as the Gaussian Disorder Model (GDM) derived from the Master Equation of the drift and diffusion framework as proposed by Bässler[124] which gives insight of morphology and transport properties by fitting against experimental results. Given its versatility, the GDM model has been utilised extensively in the literature[125-127], yet it has limited capability in predicting the performance of polymers that are yet to be made due to the needs to fit the parametric expression with experimental data. To this end, a first-principles framework is needed.

In 1959, Holstein proposed a polaronic motion model applicable to one-dimensional organic crystal[128, 129] which was extended by Perroni et al. (2011) for studies of charge transport in three-dimensional crystals.[130] The most discussed first-principles model, however, is the Su, Schrieffer and Heeger (SSH, 1980) model which describes the vibrational modes in the simplest conjugated polymer polyacetylene (c.f. Figure

45a) by considering harmonic behaviour of σ bond, kinetic energy of nuclei and coupling of π orbitals which perturb linearly as a function of bond length.[131] By applying SSH Hamiltonian to a different setup where the harmonic σ bond length is replaced by the displacement of charge carrier hopping sites from equilibrium position and π orbitals couplings with couplings between adjacent hopping sites, Troisi and Orlandi computed the charge mobility of a schematic organic semiconductors as a function of temperature (c.f. Figure 45a).[65] In another attempt, by combining SSH with Kubo formulation[132], Cataudella et al. were able to compute the carrier mobility in crystalline rubrene[d]-based transistors.[133] Nevertheless, these models are not capable of modelling conjugated systems of complex compositions and morphologies.

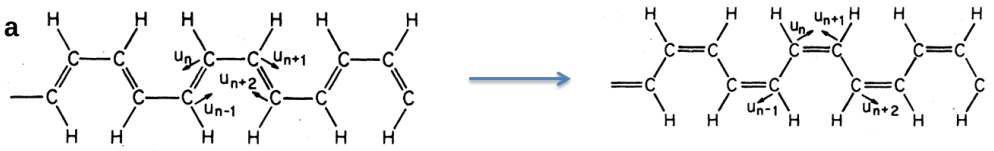

Figure 45. Illustration of first-principles models dealing with charge transport in conjugated polymer: a) Su, Schrieffer and Heeger (SSH) model used to described vibrational mode in polyacetylene; and b) Troisi and Orlandi model which employed SSH formulation but applied to a different context for study of charge transport.

In recent publications, Troisi et al.[114, 116, 134-136] reported the use of MD simulations, TD-DFT and Marcus-Levich-Jortner formulation[137-139] in studying the rate of charge hopping at a donor:acceptor interface. While this method allows for the study of structural variations on charge transport and consequently device performance, it is

[d] Chemical structure of rubrene is as shown here 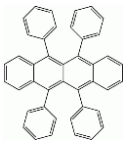

confined to the donor:acceptor interface and so far could not be used to model at macroscopic level. Furthermore, as the effect of electric field was neglected, device modelling was not possible.

To model light absorption in OPV, many research groups have employed Time Dependant Density Functional Theory (TD-DFT) technique.[140-142] While this technique is applicable to any material given that the atomic positions are known, it is computationally demanding even for small systems making modelling of an amorphous polymer highly improbable. Another less demanding alternative is through the extension of SSH model which, again, is restricted to fully crystalline structures.

In our work, we seek to establish a first-principles model based on simple Hückel orbital calculations[143] with the electronic and morphologies information derived from DFT and MD simulations. Marcus theory[144] will be used as the sole charge transport mechanism. To complete a one-dimensional device model, we employed the Two-Dimensional Electron Gas (2-DEG) model to simulate charge injection and extraction processes from the electrodes. This approach is not only robust and versatile but it can also be extended to three-dimensional structures and theoretically can be used to model conjugated systems of any composition and morphology. To validate our model, we will compare simulated results of dark current-voltage (J-V) curve and light absorption with experimental result of P3HT:PCBM system, which surfaces the strengths and limitations of the model.

3.2. The Model[54]

3.2.1. Charge Transport Calculation

3.2.1.1. Orbital Calculation

We start by first assuming a Linear Combination of Atomic Orbitals (LCAO) framework for the conjugated system. This allows us to adopt the Hückel method

originally developed in the framework of LCAO to treat conjugated molecules. The essence here is to link the π orbital of conjugated ith $|p_i\rangle$ along the conjugated backbone to the molecular orbital $|\psi_n\rangle$ of energy level n. Within the framework of Hückel method, this means solving the eigenvalue problem

$$\begin{aligned} HC &= CE \\ \rightarrow H &= CEC^{-1} \quad , \end{aligned} \tag{4.1}$$

where

$$|\psi_i\rangle = \sum_j C_{ji}|p_j\rangle \tag{4.2}$$

and

$$\langle p_i|p_j\rangle = \delta_{ij} \tag{4.3}$$

$$\langle p_i|H|p_j\rangle = H_{ij} \tag{4.4}$$

Here, H is the Hamiltonian with the diagonal entries representing the atomic orbital energy and the off diagonal elements representing the coupling energies. E is a diagonal matrix which stores energy levels of molecular orbitals. In conventional Hückel calculations, all atomic orbital energies and coupling energies are set to be the same. This picture is too simplistic considering the fact that conjugated sites are not identical. To incorporate the effect of varying chemical composition and geometry, DFT was employed for calculation of molecular orbital wavefunctions and energies level i.e. E and C which also have the added advantage of including electron-electron interaction whose effects are largely neglected in the conventional Hückel treatment. Results of E and C are inserted back to Equation (4.1) for determination of the Hamiltonian and henceforth the values of atomic orbital and coupling energies.

3.2.1.2. Incorporating the Applied Electric Field

As mentioned earlier, one of the strengths of the model is the ability to incorporate the effect of the applied electric field. To this end, we assume that the potential drop across the entire molecules can be divided into the corresponding potential drop V_i

across the ith conjugated atom assuming a linear potential drop across an individual chain. This perturbs the atomic potential energy while leaving the coupling energy unchanged. The resulting modification of the Hamiltonian is shown in Equation (4.5).

$$H_{ii} = \langle p_i|H|p_i\rangle = a_i + qV_i \tag{4.5}$$

Here, a_i represents the atomic orbital energy of ith conjugated atom in equilibrium condition and q is the electronic charge.

3.2.1.3. Charge Transport

In this work, charge transport is modelled based on the framework of Marcus theory which needs to be integrated into the already discussed extended Hückel orbital calculation. In order to do this, we first notice that the collection of eigenvectors (i.e. C) forms a set of orthogonal basis since the Hamiltonian is Hermitian. C can then be further normalised so that $|\psi_n\rangle$ form a set of orthonormal basis. This allows us to express the atomic orbital $|p_i\rangle$ as

$$|p_i\rangle = \sum_j C_{ij}|\psi_j\rangle \tag{4.6}$$

According to Marcus theory, the rate of electron transfer from the ith to the jth conjugated atom can be expressed as

$$k_{i\to j\neq i} = \frac{1}{\hbar}\sqrt{\frac{\pi}{\lambda_{i\to j}k_BT}}\left|\langle p_i|H|p_j\rangle\right|^2 \exp\left(-\frac{\left(\lambda_{i\to j}+\Delta G_{ij}\right)^2}{4\lambda_{i\to j}k_BT}\right) \tag{4.7}$$

In Equation (4.7), T is the temperature; k_B is the Boltzmann constant; $\langle p_i|H|p_j\rangle$ is the coupling energy; λ_{ij} is the reorganisation energy and $\Delta G_{i,j}$ is the energy difference between ith and jth conjugated site or simply the difference in atomic orbital energy.

$$\Delta G_{ij} = H_{jj} - H_{ii} \tag{4.8}$$

The reorganisation energy, λ, is defined as the energy change as the electron moves from the lowest energy position to the designated position assuming that there is no

change in the potential field the electron is experiencing. Since Marcus's framework assume harmonic potential type, λ can be expressed as

$$\lambda_n = \frac{1}{2} m_e {\omega_n}^2 (\Delta x)^2 \ , \tag{4.9}$$

where n represents the energy level of the system; Δx is the distance between two corresponding conjugated sites; m_e is the electron mass and ω_n is the angular frequency. Making use of the result of quantum harmonic oscillator in electric field, ω_n can be written as

$$\omega_n = \langle \psi_n | \omega | \psi_n \rangle = \frac{1}{\hbar} \left(\frac{\partial E}{\partial n} \right)_{E_n} \tag{4.10}$$

When applying Equation (4.9) to calculate the charge transport rate according to Equation (4.7), we need to be able to express λ in term of $|p_i\rangle$ the atomic orbital basis. This can be easily done by expressing $|p_i\rangle$ as a linear combination of $|\psi_n\rangle$ following Equation (4.6):

$$\begin{aligned} \lambda_{i \to j} &= \frac{1}{2} m_e \left(\Delta x_{i \to j} \right)^2 \langle \omega^2 \rangle_j \\ &= \frac{1}{2} m_e \left(\Delta x_{i \to j} \right)^2 \langle p_j | \omega^2 | p_j \rangle \\ &= \frac{1}{2} m_e \left(\Delta x_{i \to j} \right)^2 \sum_n C_{j,n}^2 {\omega_n}^2 \ , \end{aligned} \tag{4.11}$$

where $\Delta x_{i \to j}$ is the distance between two corresponding conjugated sites. So far, we have only dealt with intra-chain electron transport. Inter-chain transport, on the other hand, can be treated by simply expanding the presented method and will be discussed in greater details in the next section.

3.2.2.Light Absorption

Typically light absorption is discussed within the framework of Franck-Condon principle whereby it is said to have occurred when the corresponding electronic transitions took place between overlapping state. Although Marcus theory describes electron transfer between two reaction coordinates, it uses the same principle

dictating that electrons need to be excited to the overlapping state between corresponding reaction coordinates. The energy barrier associated with such an excitation can be deduced directly from Equation (4.7).

$$E_{barrier} = \frac{(\lambda + \Delta G)^2}{4\lambda} \tag{4.12}$$

Since wave packets that deliver higher or smaller energy than $E_{barrier}$ are unable to excite electrons to the overlapping states, the absorbed wavelengths can be expressed using Equation (4.13), where c is the speed of light, h is the Planck's constant; λ_{wave} is the wavelength of the incident wave.

$$\lambda_{wave} = \frac{hc}{E_{barrier}} = \frac{4hc\lambda}{(\lambda + \Delta G)^2} \tag{4.13}$$

3.2.3. One-Dimensional (1-D) Device Model

To construct a realistic 1-D device model, we need to consider two additional factors, namely (i) the geometry of conjugated systems especially of systems with long conjugation backbones or large M_W and (ii) the interface between the conjugated system and a metal-like electrode. Here the former is dealt with by considering two limiting cases of predominantly (i) intra-chain or (ii) π-π charge transport (c.f. Figure 46). The two cases are applicable for both amorphous and crystalline conjugated systems. We assume that the potential drop across the identical conjugated systems is the same for the case of intra-chain transport and likewise for the chain-chain gaps in both cases. For each case the chain-chain gaps are assumed to be identical as seen in Fig. 45.

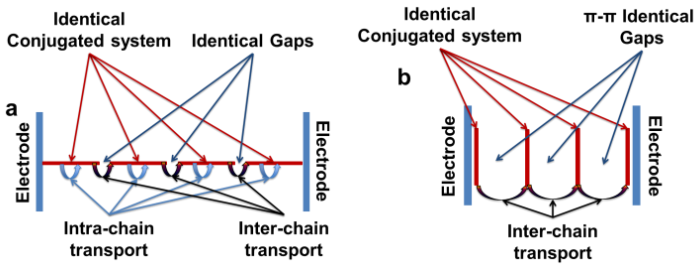

Figure 46. Schematic diagram of the 1-D device model with two limiting cases a) predominantly intra- chain transport, b) π-π charge transport.

In the first case of predominant intra-chain transport (Figure 46a), inter-chain transport is modelled by first assuming that the angular frequency ω is invariant between the intra and inter chain transport. Next we replace intra-chain distances $\Delta x_{i\to j}$ with Δx^{chain}, which represents the chain-chain identical gap, and the off-diagonal component $\langle p_i|H|p_j\rangle$ in Equation (4.7) with C^{chain}, which represents the coupling energy between the adjacent chains.

$$k^{chain} = \frac{1}{\hbar}\sqrt{\frac{\pi}{\lambda_{i\to j}^{k\to l} k_B T}}\left|C^{chain}\right|^2 \exp\left(-\frac{\left(\lambda^{chain} + \Delta G_{ij}\right)^2}{4\lambda^{chain} k_B T}\right) \tag{4.14}$$

Where

$$\lambda^{chain} = \frac{1}{2} m_e \left(\Delta x^{chain}\right)^2 \sum_n C_{j,n}^2 {\omega_n}^2 \tag{4.15}$$

For the second case of π-π charge transport, inter-chain transport is treated in the exact same way as intra-chain case described above. However, the Hamiltonian was modified such that all diagonal entries were zeroes, indicating that they are in equilibrium or the chemical potential is uniform; the off-diagonal entries were replaced with π-π coupling energy $C^{\pi-\pi}$; and the Δx was replaced with π-π gaps or $\Delta x^{\pi-\pi}$. The new coupling and spatial separation terms can be determined by DFT and MD simulation respectively as we will discuss in more detail in Section 3.3.2.

However, Equation (4.7) and (4.14) only address the electron transfer rate. A conversion to actual current flowing in the system is necessary for dark J-V calculation. This is done by considering all the possible pathways from one electrode

to the other. For each pathway, minimum transfer rate k_{min} will be the limiting factor determining the amount of current flowing through the channel. Current density equation is summarised in Equation (4.16), where q is the electronic charge and A is the cross-sectional area.

$$J = \frac{I}{A} = \frac{q \sum_{pathways} k_{min}}{A} \tag{4.16}$$

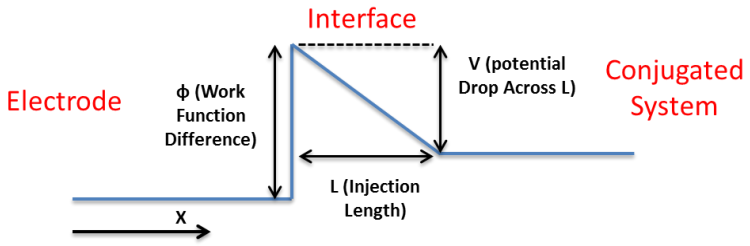

*Figure 47. Schematic diagram of interface model between electrode and conjugated system, where **ϕ** is the work function difference or charge injection energy barrier, **L** is the injection length, and **V** is the potential drop across L. The interface region was modelled using 2-DEG Hamiltonian.*

To model charge injection from the electrode into the conjugated system, we first consider the setup consisting of three distinct regions namely the electrode, the interface and the conjugated system (c.f. Figure 47). In this model, the injection length L is taken to be approximately similar to the conjugation length of a single molecule. This can easily be changed when a more rigorous study of the interface is available.

The Hamiltonian of the interface region is defined in Equation (4.17). Where m_e and E are the mass and kinetic energy of the electron respectively; F is the constant electric field strength; and ψ is the wavefucntion.

$$-\frac{\hbar^2}{2m_e}\frac{\partial^2\psi}{\partial x^2} + (Fx - E)\psi = 0 \tag{4.17}$$

The solution to Equation (4.17) is available elsewhere.[145] By adopting this solution and considering free electron motion in both the electrode and conjugated system region, we can then write down the solution of the electron wavefunction in each of the three regions (c.f. Equation (4.18)).

$$\begin{aligned}\psi_{Electrode} &= Ae^{ikx} + Be^{-ikx} \\ \psi_{Interface} &= C\int_0^{\infty} \cos\left(\frac{u^3}{3} + u\xi(E,x)\right)du \\ \psi_{Conjugated} &= De^{ikx}\end{aligned} \tag{4.18}$$

Here A, B, C and D are unknown parameters and ξ is defined in Equation (4.19) with ϕ, L and V defined in Figure 47.

$$\xi(E,x) = \left(\frac{\phi - E}{V}L - x\right)\left(\frac{2m_eV}{L\hbar^2}\right)^{\frac{1}{3}} \tag{4.19}$$

As the wavefunction must be smooth and continuous at the boundaries between different regions, the probability of electron tunnelling from the electrode region into the conjugated system region can be evaluated using Equation (4.20).

$$T(E) = \left|\frac{D}{A}\right|^2 = \left(\frac{2f(E,0)f(E,L)}{f^2(E,0) + f^2(E,L)}\right)^2 \tag{4.20}$$

with

$$f(E,t) = \frac{\partial}{\partial x}\left(\int_0^{\infty} \cos\left(\frac{u^3}{3} + u\xi(E,x)\right)du\right)\Bigg|_{x=t} \tag{4.21}$$

By treating the electrode as metal-like, the current density flowing into the conjugated system region can be calculated by adopting the Drude model equation (c.f. Equation (4.22)).

$$J = \sigma F = \frac{1}{3}qv_F^2F\mu_d m_e\int_{E_f}^{\infty} T(E)g(E)f(E)dE \tag{4.22}$$

where

$$g(E) = \left(8\pi\sqrt{2}\right)\left(\frac{m_e}{h^2}\right)^{3/2}\sqrt{E}$$

$$f(E) = \frac{1}{1 + \exp\left(\frac{E - E_f}{kT}\right)}$$

Here $g(E)$ is the density of states; $f(E)$ is the Fermi-Dirac distribution; μ_d is the electron mobility; v_F is the Fermi velocity or the average velocity of conducting electron. All these are properties of the metal-like electrode. In this work, the

integrals in Equation (4.18), (4.21) and (4.22) will be evaluated numerically using Gaussian Quadrature.

3.3. Application to P3HT:PCBM Solar Cell

3.3.1. Experimental Procedure

P3HT/PCBM bulk heterojunction solar cells were prepared on pre-patterned ITO substrates. The ITO substrates were thoroughly cleaned using a detergent solution under flowing tap water. This procedure was followed by successive sonication treatment in deionised water, acetone and isopropanol for 15 min each. The substrates were then dried in an oven for 3 hours. The substrates were then subjected to UV-Ozone treatment for 15 minutes and then the PEDOT:PSS was spin-coated at 5000 rpm for 50s to obtain an approximately 50 nm thin layer. Prior to the PEDOT:PSS deposition, the solution was filtered through a 0.45 μm cellulose filter. The PEDOT:PSS coated substrates were annealed in an inert atmosphere (N_2) for 20 min at 140°C. A solution of 15 mg/ml regioregular P3HT and 12 mg/ml PCBM in oDCB was stirred and heated at 60°C overnight inside a glove box (less than 1 ppm moisture and O_2) before being cooled to room temperature and spin-cast onto the PEDOT:PSS-coated ITO substrates. To complete the device a cathode consisting of 0.5 nm LiF / 80 nm Al was evaporated through a shadow mask, resulting in an active device with an area of 9 mm^2. Each ITO substrate contained 6 devices.

3.3.2. Simulation Parameters Derivation

Before validating the model with experimental result of P3HT:PCBM device, various parameters need to be determined. These include geometric arrangements of P3HT molecules, coupling and atomic orbital energies. The former was studied by MD method using the optimised forcefield as discussed in Section 2.2.2.2. Here the geometric arrangements of interest include the spatial separations of terminal conjugated carbon atoms located in separate chains and the disordered arrangements

of amorphous P3HT. While the former is used as the identical gaps in the predominantly intra-chain transport picture (c.f. Figure 46a), the latter is further analysed by DFT for a quantitative evaluation of coupling and atomic orbital energies. In this work, coupling energy is calculated energy splitting method.[146, 147] On the other hand, the parameters set for the case of crystalline P3HT (except for distance between chain ends) were obtained by assuming Brinkmann's reported crystal structure determination[101].

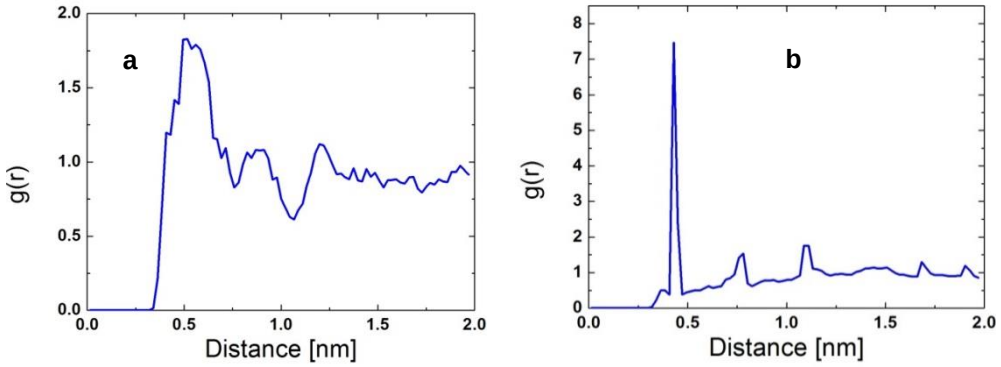

Figure 48. Radial distribution function of a) terminal conjugated carbon atoms in P3HT ensemble consisting of 12 molecules of M_W =3320g/mol (or 20 thiophene rings) at 300 K and 1 atm, b) sulphur atoms on different molecules in amorphous-like P3HT ensemble of 2 molecules of M_W = 1328 g/mol (or 8 thiophene rings) at 300 K and 1 atm

To obtain the spatial separations of terminal conjugated carbon atoms, N-P-T ensemble of 12 P3HT molecules, each of 3320 g/mol M_W (or 20 thiophene rings), was calibrated at 700 K and 1atm for 800 ps. It was then cooled down to 300 K at a rate of 0.1 K/ps. The ensemble is then allowed to stay at 300 K and 1atm for another 750 ps before radial distribution analysis is done on all of the terminal carbon atoms present. The result (c.f. Figure 48a) indicated that the most prominent shortest distance between terminal carbon atoms or the chain-chain gap in the predominantly intra-chain transport picture (c.f. Figure 46a) is 5.17 Å. This approximation can be used for both amorphous and crystalline P3HT modelling.

The π-π gaps on the other hand are determined in a relatively different manner. For crystalline P3HT, this value is 4.17 Å which is the sulphur-sulphur distance on two nearest thiophene rings located on different molecules assuming Brinkmann's

reported crystal structure as abovementioned. For amorphous P3HT, we will be using a different P3HT ensemble with 2 molecules of 1,328 g/mol (or 8 thiophene rings) calibrated at 1000 K and 1 atm for 1000 ps. Since this system will later on be analysed by DFT method, any system larger than this will be computationally unrealistic for our resources. After the calibration step, we quench the ensemble directly to 300 K and keep it there for 750 ps. This was done to ensure that the resulting structure resemble the disorder features in amorphous P3HT. Radial distribution analysis on sulphur atoms between different molecules allows us to estimate the π-π gap of amorphous P3HT. From Figure 48b the spatial separation is determined to be about 4.29 Å. All MD simulations were performed with the Forcite Plus engine of Accelrys Materials Studio.[148]

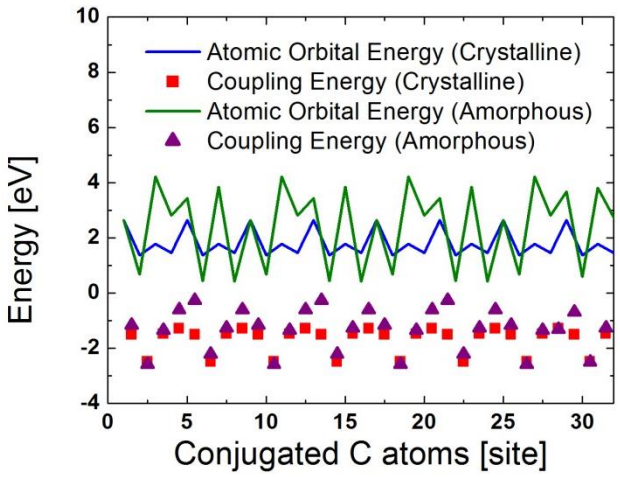

Figure 49. Atomic orbital energy (lines) and coupling energy (symbols) of amorphous and crystalline P3HT molecules as a function of conjugated carbon atom sites.

Figure 49 displays the coupling and atomic orbital energies of amorphous and crystalline P3HT as a function of conjugated carbon atom sites obtained directly from DFT calculation. In the amorphous case, large M_W P3HT is modelled by retaining the DFT results for conjugated carbon atoms at the terminal thiophene ring pairs, while for the inner thiophene ring pairs we use the values, pair-wise, of the two central thiophene rings in the eight rings DFT model mentioned above. In crystalline P3HT on the other hand, all the adjacent thiophene rings pairs are expected to assuming the

same value as computed from Brinkmann's crystal structure determination (in the Brinkmann model the chains are approximated as being of infinite length). Other required parameters including the chain-chain coupling energy $\boldsymbol{C^{\pi-\pi}}$ and $\boldsymbol{C^{chain}}$ (c.f. Section 3.2.3), were determined to be 0.52 eV and 0.01 eV, respectively by DFT.

	ITO	Al
Carrier Concentration	2×10^{20} cm^{-3}	1.8×10^{23} cm^{-3}
Carrier mobility	73.35 $cm^2/(V\cdot s)$	10.42 $cm^2/(V\cdot s)$
Work function	4.7 eV	4.2 eV

Table 9. Electrode material parameters of ITO and Al used in the 1-D device model.

To complete the 1-D device model, we will be adopting Indium Tin Oxide (ITO) and Aluminium (Al) as the simulated electrodes sandwiching the conjugated system layer so as to match our fabricated cell (c.f. Section 3.3.1). The parameters for ITO and Al used in this work were adopted from literature and listed in Table 9.[149-152]

3.3.3. Charge Transport and Dark J-V Curve

As mentioned in Section 3.2.3, two charge transport modes, namely π-π transport and predominant intra-chain transport, are considered in this work. However, simulation using the discussed model suggests that the former is much more prominent as evident from Figure 50. This finding has three consequences. First P3HT crystals with face-on orientation with the electrode or substrate will possess much higher mobility, which is consistent with previous experimental findings.[153, 154] Second, the summation over all charge transport pathways in Equation (4.16) can be simplified into a summation over the π-π transport pathways only. For the 1-D device model this means that only the limiting case of π-π transport mode (c.f. Fig 1b) needs to be considered. Nevertheless, this is a useful insight when the model is extended to 2-D or even 3-D. Third, since π-π transport mode does not depend on chain length, we believe that the experimentally observed charge mobility gain in large M_W systems are due to the higher driving force toward crystallinity which then induces more effective π-π couplings.

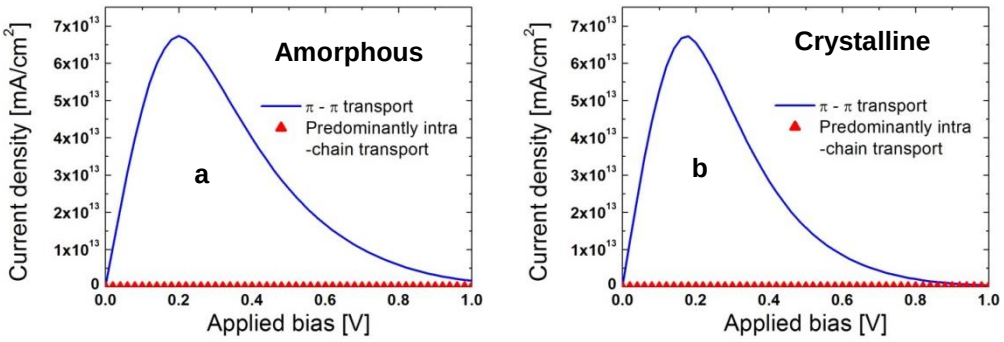

Figure 50. Dark J-V curve (without electrodes) of predominantly intra-chain and π-π transport modes for the case of a) amorphous and b) crystalline P3HT.

It is worth mentioning that Figure 50 is distinctly different from the dark J-V behaviour seen in Figure 51, because the electrodes were neglected in the former. From here we can see that the threshold current effect (c.f. Figure 51) is brought about by the mismatch in Fermi level between the electrodes and the conjugated system. The tremendously large current density was brought about by the assumption that the sample was 100% ordered and no charge scatterings were considered. Also the striking similarity of Figure 50a and b was caused by the simplified 1-D consideration which reduces the cases of crystalline and amorphous P3HT to essentially identical geometries that differs only marginally in terms of coupling energy and inter-chain distance.

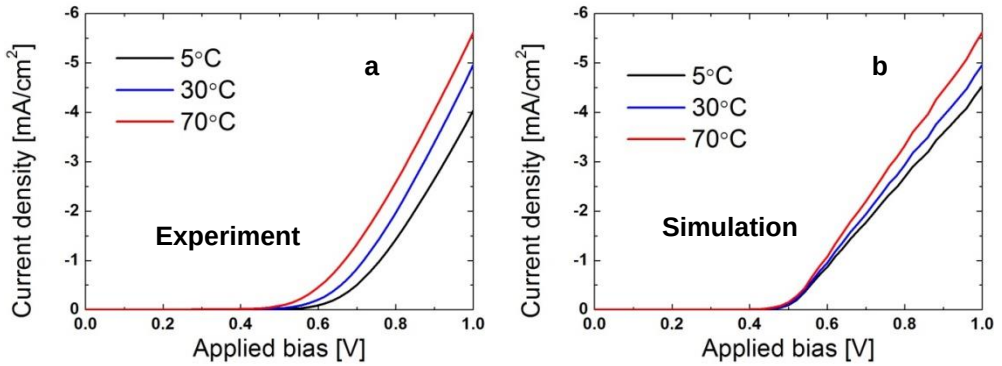

Figure 51. Dark J-V curves at different temperatures as determined from a) experiment and b) simulation.

Figure 51 shows the J-V curves from 0 V to 1 V at 5°C, 30°C and 70°C obtained using both experiment and simulation for an active layer of 80 nm (corresponding to 100 s spin casting at a speed of 200 rpm). For the simulation runs, M_W of 48,000

g/mol was assumed for all P3HT chains in the device. P3HT, ITO and Al layer thicknesses were chosen to be 80 nm, 50nm, and 50nm respectively to match the manufactured cell. Figure 51 shows a relatively close agreement between simulation and experiment when it comes to J-V variation with temperature. Nevertheless, there are distinct features in the experimental curves that have not been replicated in the simulation. First the large curvature, especially at about 0.6V when the current significantly rises, is less pronounced in the simulated curves. Second, experimentally there seems to be minimal changes to the J-V slope at high voltage (>0.8V), when the temperature rises while changes in slope is the main feature in the simulation results. Third, the experimental curves are considerably smoother compared to the simulation runs, where fluctuations in the curves result from the subtle changes in the Hamiltonian each time the voltage is altered. These differences give us insightful information into the shortcomings of the current model. It is also worth mentioning that here PCBM is implied to act as part of the electrode.

3.3.4.Light Absorption

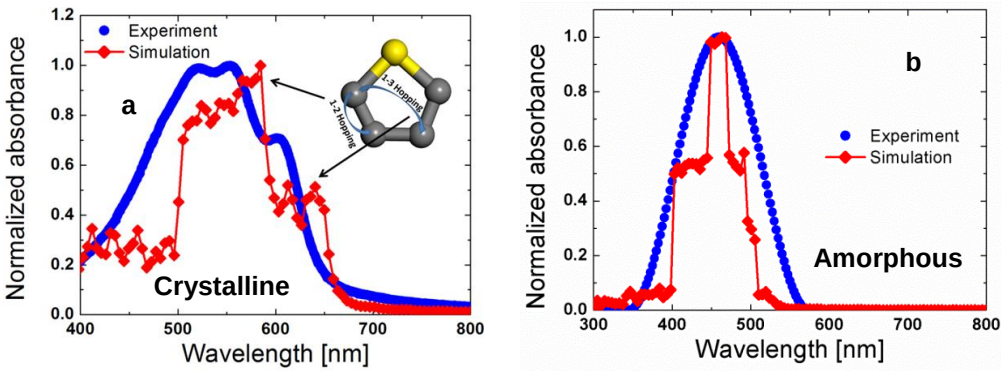

Figure 52. Normalized light absorption spectrum of (a) crystalline P3HT and (b) amorphous P3HT. The broad peak at 500 – 540 nm and the 600 nm shoulder in the crystalline case is attributed to 1-2 hopping and 1-3 hopping respectively. For the amorphous case, inclusion of 1-3 absorption does not change the simulated spectrum because the additional absorption falls within the range of the 1-2 hopping spectrum.
Experimental absorption data for crystalline P3HT (b) is adopted from literature.[155]

Besides dark-current voltage, the simulated light absorption spectrum was also compared against experimental spectra for both amorphous and crystalline P3HT (Figure 52). To replicate the M_W distribution of the P3HT sample, which ranges from 32,000 g/mol to 64,000 g/mol, we employ a pool of 100,000 P3HT molecules following a M_W normal distribution with mean value of 49,800 g/mol and a standard deviation of 5000 g/mol. Contrary to the case of dark J-V, light absorption was mainly associated with intra-chain electron transfer. The energy barriers associated with π-π inter-chain transport are relatively low making the absorption wavelength much higher than the range of interest (the solar spectrum). In the light absorption calculations shown above (c.f. Figure 52a and b), the spectrum range relevant for solar radiation is attributed to the 1-2 and 1-3 intra chain hopping which is illustrated in the inset of Figure 52a. More specifically, the diffused peaks a 500nm and the shoulder at 600nm for crystalline P3HT are attributed to the 1-2 and 1-3 intra chain hopping, respectively. For amorphous P3HT, both processes contribute to the same absorption peak at 450 nm. It is worth mentioning that the simulated results in Figure 52 already consider the effect of peak smearing which is caused by the coupling energy of the corresponding hopping sites. This is because electronic coupling

between hopping sites enlarges the energy window of the overlapping states leading to a range of possible excitation energy from incident photons. This also means that for higher order charge hopping (1-4, 1-5 and so on), regardless of the energy barrier, the progressively smaller coupling energy as the hopping sites become further apart implying that considerably smaller contributions to the overall absorption spectrum can be expected. In cases of crystalline and amorphous P3HT, higher order charge hoppings (1-4, 1-5 and so on) thus do not significantly contribute to the absorption spectrum due to the negligible coupling energy.

The close resemblance between the simulated and experimental absorption spectrum of crystalline and amorphous P3HT suggests that the current model is sufficiently robust and accurate for preliminary probing of light absorption capability of new conjugated organic semiconductors. This would aid in molecular design of new donor materials relevant for high performance OPV.

3.4. Morphological Effects on Charge Transport in P3HT:PCBM[156]

3.4.1. Extension of Current Model

While we have established a model for charge transport in conjugated semiconductors and validated them against experimental results for the case of P3HT:PCBM, we have not discussed the effects of the active layer morphology on the charge transport phenomena. Given that the morphology of OPV is non-conventional and that it plays a crucial role in determining the device performance, understanding how the morphology would influence charge transport is therefore important. To this end, we need to incorporate PCBM, which so far has been treated as part of the electrode, explicitly into the model formulation. This was done utilising the finding from Section 3.3.3 that inter-molecular transport is dominant in P3HT:PCBM OPV devices. We define the Hamiltonian such that the diagonal entries are the molecular orbital energy and the off-diagonal entries are the coupling energy between the

respective molecules. This is analogous to the case of π-π charge transport discussed in Section 3.2.3. The difference here is that we would have two distinct regions representing P3HT and PCBM (instead of only P3HT for the case discussed in Section 3.2.3) in a bilayer 1-D model as can be seen in Figure 53. In this 1-D model, the device assumes a thickness of 100 nm typical of an OPV device with P3HT and PCBM layers each spanning 50 nm.

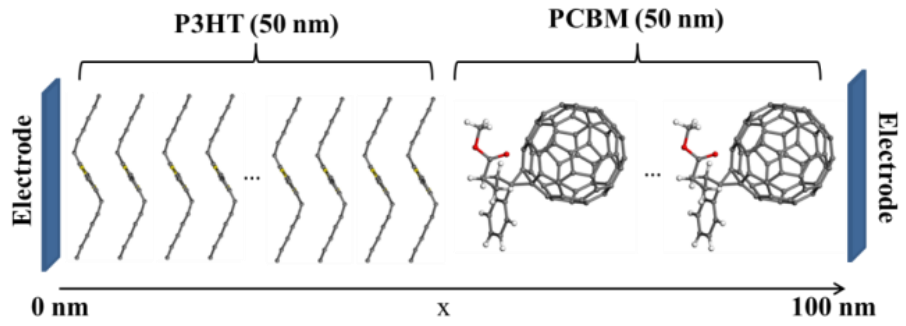

Figure 53. Schematic layout of 1-D bilayer P3HT:PCBM charge transport model. Here we adopted a bilayer morphology with an active layer thickness of 100 nm and P3HT layer thickness of 50 nm.

Analogous to the previous treatment for the simplified model of Section 3.2.3, the diagonal elements are the same within the P3HT and PCBM regions respectively. However, there would be an energy mismatch at the P3HT:PCBM interface which is analogous to the energy difference between P3HT's HOMO and PCBM's LUMO. Another difference in this formulation compared to the previous model is the absence of an electrode. This means that the results presented in Section 3.4 are directly relevant to charge transport within the active layer and are more useful for in-depth analysis and optimization of this layer. While electrode and active layer interface is crucial to the device performance, it is not the focus of this project and thus will not be explored in greater details here.

Similar to Section 3.3, the molecular orbital and coupling energies were computed using DFT method while morphological information were obtained from both atomistic and coarse-grained dynamics simulations. This will be discussed in Section 3.4.2.

3.4.2.Parameters

3.4.2.1. Back-mapping from Coarse-grained to Atomistic Model

In contrast to the model discussed in Section 3.2.3[54] here the morphological information was obtained using both coarse-grained[64] and atomistic forcefields.[79, 98] To obtain a set of plausible interface configurations, the final MD snapshot of the face-on bilayer configuration (which we had shown as by far the most stable configuration) of the coarse-grained model obtained from previous simulations was utilized (c.f. Section 2.3.5.2) so that larger interfacial areas with smaller periodic boundary interference can be achieve. However, since DFT calculations need to be done on atomistic models, a back-mapping algorithm from coarse-grained to atomistic model is required. A general algorithm to convert from coarse-grained to atomistic model is described below:

1. Atomistic P3HT meres and PCBM molecules are placed inside the snapshot such that the centroid of thiophene rings and fullerene cage coincide with the corresponding coarse-grained beads.

2. For P3HT, the orientation of the thiophene rings is aligned so that the ring face contains the backbone chain of the coarse-grained model and the atomistic side chain models have minimal distance to the two beads of the coarse-grained representation of the side chain.

3. We then rotate the PCBM molecules such that the side chains would attain the closest distance from their corresponding coarse-grained beads.

4. The coarse-grained beads are deleted and the system is geometry- optimized using the atomistic forcefield.

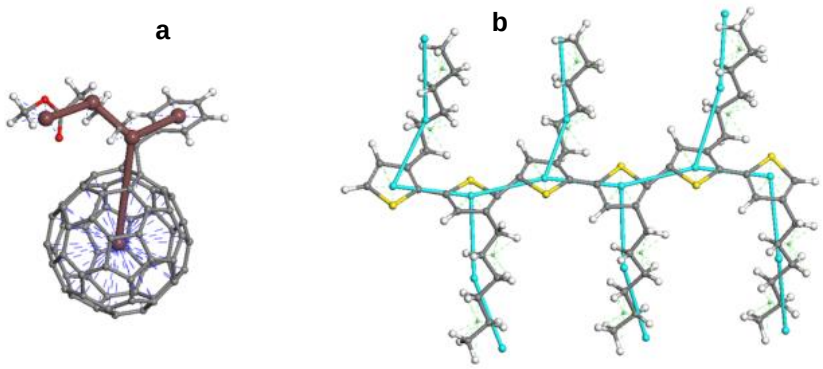

Figure 54. Illustration of back-mapping from coarse-graining to atomistic model for (a) PCBM and (b) P3HT. The brown segment in (a) and cyan in (b) represents the coarse-grained model whereas the rest represent the corresponding atomistic model.

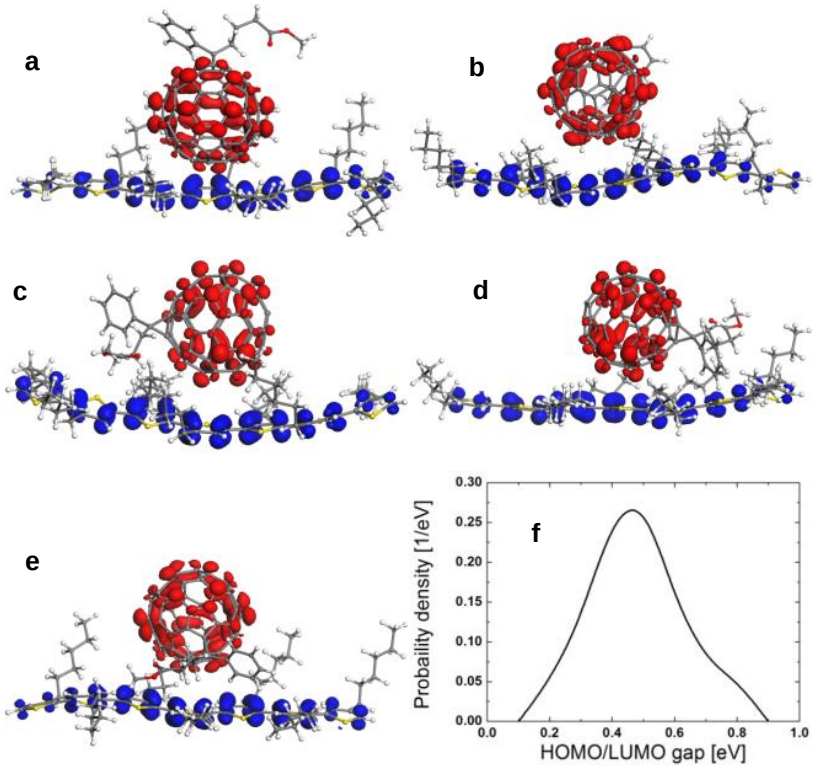

Figure 55. Five randomly chosen PCBM:P3HT configurations out of 50 interfacial arrangements obtained by back-mapping from coarse-grained simulations and geometry optimised using atomistic forcefield, followed by DFT optimisation of the truncated structures. The computed HOMO (blue) and LUMO (red) distributions are also shown. (f) The distribution of HOMO/LUMO energy gap of these 50 structures showed a mean value of 0.53 eV with a peak at 0.48 eV.

A demonstration of this back-mapping procedure is shown in Figure 54. The atomistic model obtained by back-mapping is then relaxed for 20 ps at 450 K before the 50 closest pairs of PCBM and P3HT molecules from the relaxed interface model are identified. It should be noted that we have also carried out density functional theory (DFT) geometry optimizations of the these 50 PCBM:P3HT molecule pairs,

but in all cases the DFT geometry optimisations of the isolated molecules lead to a similar state (minimal spread in HOMO LUMO gap and coupling of less than 5%) that do no longer correlate to the respective orientation of P3HT and PCBM in the simulated device morphology; hence the MD optimized structures were employed for all DFT calculations.

In the original coarse-grained simulations and the subsequent atomistic relaxation each P3HT molecule consists of 60 thiophene rings (corresponding to a molecular weight of 9,960 g/mol). To keep the computational effort manageable the P3HT chains are truncated to the 7 thiophene rings closest to the PCBM molecules. The arrangements of 5 randomly chosen truncated configurations out of these 50 pairs can be seen in Figure 55(a-e). DFT calculations of the truncated configurations were conducted to solicit the HOMO/LUMO level and coupling energy at the interface.

3.4.2.2. Coupling Energy

The coupling energy calculations employed in this work follow the energy splitting method[146, 147] and the resulting energy values are summarized in Table 10. For ordered[e] P3HT, we assume a non-interdigitated and staggered crystalline form in line with the reported single crystal diffraction data.[101] For the coupling energy calculations we considered a system with 2 molecules each consisting of infinite length while the unit cell only holds 8 thiophene rings. For disordered P3HT, the same unit cell was first heated at 1,000 K for 1,000 ps before annealing at 300 K for 1,000 until the system density stabilized at which point a realistic density (~ 1.1 g cm^{-3}) was observed.

[e] Please note that we refer to fully crystalline and amorphous structures as ordered and disordered respectively in this case. This is because constructed 'amorphous' structure still exhibits periodic boundary condition, hence, in the strict sense, it is still fully crystalline. This is in contrast to Sections 3.2 and 3.3 where data pertaining to amorphous state was obtained by calculation in the gas phase. The reason for such a change is because intermolecular coupling energy cannot be determined reliably in the gas phase.

	Coupling energy (eV)
P3HT-P3HT (Ordered)	0.56 ± 0.01
P3HT-P3HT (Disordered)	0.11 ± 0.02
PCBM-PCBM (Ordered)	0.22 ± 0.01
PCBM-PCBM (Disordered)	0.21 ± 0.01
P3HT-PCBM	0.078 ± 0.11

Table 10. Coupling energy of various terms determined from DFT calculations.

For PCBM, experimental crystal structure of PCBM in ortho-dichlorobenzene (oDCB)[97] with oDCB removed was used as the starting configuration. For the calculation of coupling energy, we only considered a single unit cell consisting of 4 PCBM molecules. For deriving disordered structure, we followed an analogous procedure to that discussed above for disordered P3HT. First the system was heated at 1,000 K for 1,000 ps followed by annealing at 300 until the density stabilized at which point a realistic density (~ 1.3 g cm^{-3}) was observed. Both the PCBM and P3HT systems then underwent atomistic MD simulation with NPT ensemble at 300 K and 1 atm for 3,000 ps, 10 random structures were taken from the last 1,000 ps and their energy was computed by DFT. The 5 most stable among them are then used for the P3HT:P3HT and PCBM:PCBM coupling energy analysis.

For the case of P3HT:PCBM coupling, all 50 configurations obtained from back-mapping of the coarse-grained model and optimised with atomistic MD simulation as discussed earlier (c.f. Figure 55 (a-e)) were considered. It's worth mentioning that for P3HT:PCBM coupling, the resulting average value listed in Table 10 refers to the coupling between the HOMO of P3HT and the LUMO of PCBM. Other conceivable coupling terms (i.e. HOMO of P3HT : HOMO of PCBM LUMO of P3HT – PLUMO of PCBM, LUMO of P3HT: HOMO of PCBM) are at least three orders of magnitude smaller, hence, would not contribute significantly to the transport process and will not be included in the framework of the current model.

3.4.2.3. Geometry Parameters

To determine the intra-layer spacing in P3HT and PCBM as well as the inter-layer P3HT-PCBM spacing, radial distribution function (RDF) analysis was performed on the coarse-grained dynamics simulation at 300 K. For the intra-layer spacing within the donor and acceptor layer individually, we constructed ordered and disordered cells of P3HT and PCBM each with dimension of approximately 1,000 nm^3 and anneal them for 3,000 ps at 300 K and 1 atm. For ordered P3HT, the unit cell contains 78 molecules each with 30 thiophene rings or a molecular weight of 9,960 g/mol; for disordered P3HT, 48 molecules each with molecular weight 14,940 g/mol. For both ordered and disordered PCBM, the unit cell holds 840 molecules. Disordered structures were obtained by annealing corresponding ordered structures at 1,000 K for 2,000 ps followed by 3,000 ps at 300 K. Starting conformation of crystalline P3HT and PCBM was obtained following the procedure as discussed in Section 3.4.2.2.

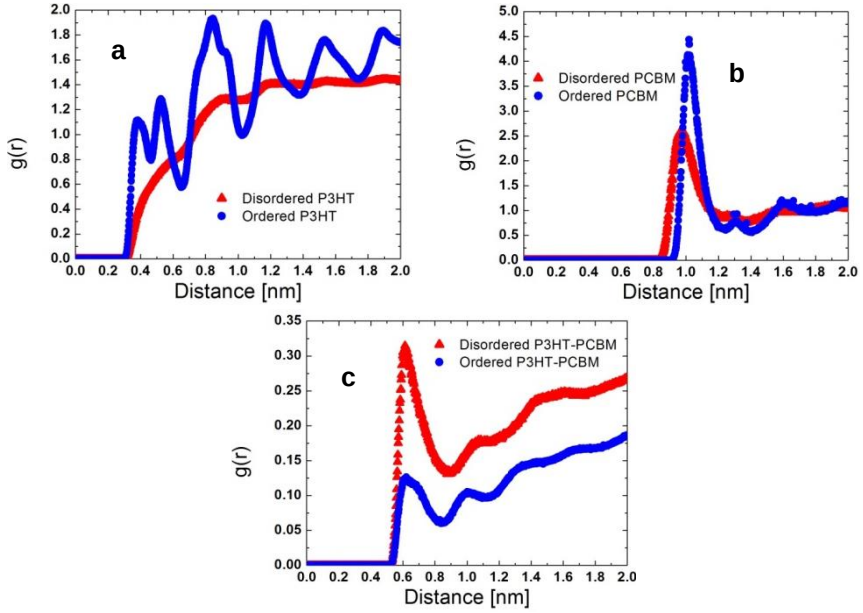

Figure 56. RDF analysis of (a) thiophene rings centroids in disordered (red triangle) and ordered (blue circle) P3HT and (b) fullerenes centroids in disordered (red triangle) and ordered (blue circle) PCBM. (c) RDF of thiophene rings centroids and fullerene centroids in coarse-grained P3HT:PCBM bilayer. The first major peaks from (a,b) and (c) were used as the intra-layer and inter-layer spacing 1-D device model respectively.

After annealing at 300 K for 3,000 ps, the last 1,000 ps was subjected to RDF analysis. The first major peak in the intermolecular thiophene rings centroids and fullerenes centroids RDF were identified with the intra-layer spacing of P3HT and

PCBM, respectively (c.f. Figure 56 (a-c)). For the case of disordered P3HT, due to the presence of strong peak overlap, the first minimum of the second derivative was chosen as the inter-layer spacing.

The inter-layer spacing was determined by relaxing the face-on and amorphous P3HT:PCBM bilayer model (which previously had been equilibrated over 10,000 ps at 450 K) 2,000 ps at 300 K, followed by a 1,000 ps production run as the basis of the RDF analysis. From this RDF analysis we can extract the distance between the thiophene ring centroids of P3HT and the fullerene centroids of PCBM (c.f. Figure 4 (c)). The results obtained from RDF analysis are summarized in Table 11.

Category	Sub-category	Parameters names	Symbol	Value
Geometry parameters	Intra-layer spacing	Ordered P3HT		3.87 Å
		Disordered P3HT		4.27 Å
		Ordered PCBM		10.2 Å
		Disordered PCBM		9.69 Å
	Inter-layer spacing	Ordered P3HT - PCBM		6.39 Å
		Disordered P3HT - PCBM		6.23 Å
	Layers thickness	P3HT		50 nm
		PCBM		50 nm
Ambient condition		Temperature	T	300 K
Physical constant		Boltzmann Constant	k_B	$8.617 \cdot 10^{-5}$ eV·K^{-1}
		Electronic charge	q	$1.602 \cdot 10^{-19}$ C
		Electronic mass	m_e	$9.109 \cdot 10^{-31}$ kg
		Reduced Plank's constant	$\hbar$	$6.582 \cdot 10^{-16}$ eV·s

Table 11. List of parameters and their values (expect coupling energy which is shown in Table 1) used in the 1-D device model presented here.
For light absorption calculations, intra-molecular coupling and atomic energy level of P3HT parameters are available in Section 3.3.2.

3.4.3. Charge Transport Efficiency

To better understand the charge transport mechanism in P3HT:PCBM, in this Section we applied the discussed framework to the simplified 1-D device model (c.f. Figure 53). Furthermore, we observed that the PCBM – PCBM coupling energy and intra-layer spacing are very similar for ordered and disordered PCBM (c.f. Table 10 and

Table 11). Thus for subsequent charge transport calculations, average coupling energy and intra-layer spacing values of 0.22 eV and 9.95 Å were used for PCBM.

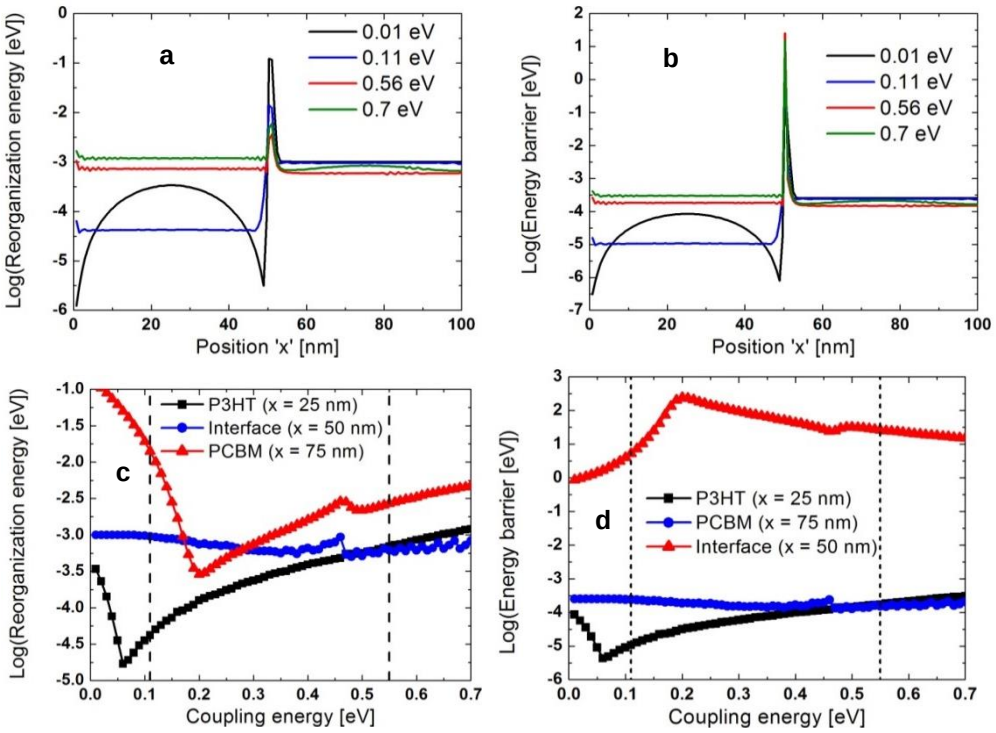

Figure 57. Log of (a and c) reorganization energy and (b and d) energy barrier of inter-molecular charge hopping (a and b) as a function of position along the 1-D device, with P3HT spanning from 1nm – 50nm and PCBM from 50-100 nm or (c and d) as a function of P3HT coupling energy. Graphs (a and b) are plotted at different hypothetical P3HT – P3HT coupling energy of 0.01 eV (black line), 0.11 (blue line), 0.56 eV (red line) and 0.7 eV (green line). The graphs (c and d) are plotted for P3HT (black), PCBM (blue) and interface (black) regions. Here, the dotted lines mark the calculated coupling energy for ordered and disordered P3HT.

First we look at the reorganization energy as a function of distance along the 1-D device. At very low P3HT coupling energy (0.01 eV) pertaining to the case of gas phase or no adjacent P3HT molecules, the reorganization energy at the interface reaches 0.12 eV (c.f. Figure 57a), which is in agreement with reported excited states DFT calculations value for P3HT:PCBM interface at gas phase of 0.06 eV – 0.18 eV.[116] It's also interesting to note that the reorganization profile as a function of position along the 1-D device changes as we move from the low coupling region (~0.1 eV) to the high coupling region (~0.5 eV). The plot for the reorganization energy at the middle of P3HT (x = 25 nm), PCBM (x = 75 nm) and interface (x = 50 nm) regions as a function of P3HT coupling energy (c.f. Figure 57c) reveals a

minimum reorganization energy occurring at 0.06 eV and 0.19 eV for P3HT and interface cases respectively which also marks the changes in reorganization energy profile against position along the 1-D cell (c.f. Figure 57a). It is interesting to note that as the turning point occurs, the reorganization energy in PCBM also slowly decreases from 10^{-2} eV to 6×10^{-3} eV and then stays relatively constant. Thus the change from order to disorder in the P3HT layer only weakly affects the charge transport behaviour in the PCBM layers.

The reorganization profiles also show very close resemblance to the charge transport energy barrier (c.f. Equation (4.12)) profiles (c.f. Figure 57b and d). In Figure 57d, the interface energy barrier reaches a maximum at 0.20 eV while P3HT energy barrier reaches a minimum at 0.07 eV. The close correspondence of P3HT and interface profiles for both reorganization energy and energy barrier suggests that interfacial transport behaviour is strongly influenced by the coupling energy or morphology of the underlying P3HT layers.

Furthermore, since the energy barrier within the P3HT layer (at 25 nm) reaches a minimum of 0.07 eV (c.f. Figure 57d), this suggests that within the disordered regime (coupling energy ~ 0.11 eV) charge transport efficiency increases as a function of coupling energy but within the ordered regime (coupling energy ~0.56 eV) the reverse is true. To test this hypothesis, we computed the dark J-V curve of P3HT:PCBM device assuming a bilayer 1-D morphology as discussed (c.f. Figure 53). Ten J-V curves were computed at hypothetical interfacial HOMO/LUMO gap values of 0.1 eV – 1 eV at 0.1 eV interval for both ordered and disordered P3HT cases. Results shown in Figure 58 a,b show some remarkable features.

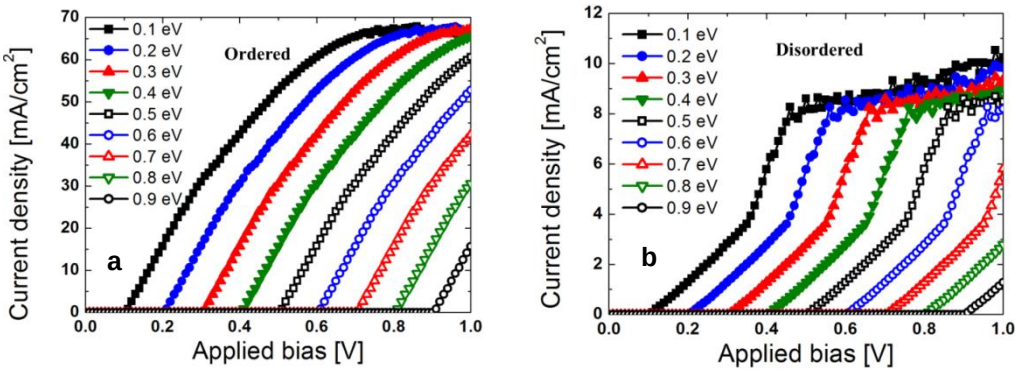

Figure 58. Dark current-voltage curve of (a) ordered and (b) disordered P3HT:PCBM at different hypothetical interfacial P3HT's HOMO and PCBM's LUMO energy mismatch ranging from 0.1 eV – 0.9 eV.

For the disorder J-V curve, four distinct regions can be discerned: (1) at very low bias (when the applied bias is much less than the interface's HOMO/LUMO mismatch) no current is flowing through the device; (2) when the applied bias exceeds that of the mismatch level, current starts to rise. In regimes (1) and (2) the current is limited by the interfacial electron hopping from P3HT to PCBM. (3) When the bias is raised to 0.25 V above the onset, the slope increases due to the exponential dependence of the current on the energy mismatch. The exponential effect is softened because the limiting current is now due to the P3HT molecules adjacent to the interface instead of the hopping from P3HT to PCBM at the interface. (4) At 0.37 V above the onset, the slope is reduced again. This is caused by the low coupling energy in the disordered P3HT region, which reduces the generated current. For the ordered J-V curve, again four regions can also be identified: (1) at an applied bias below that of the interfacial energy mismatch, there is no resulting current; (2) at applied bias beyond the interfacial energy mismatch, the onset of dark current appears with the interfacial hopping from P3HT to PCBM as the limiting current; (3) the changes in limiting current region from the interface to the PCBM molecules adjacent to the interface at about 0.23 V above the onset causes the reduction in slope of the J-V curve; (4) at about 0.4 V above the onset the curve reaches a plateau where the current is limited by the PCBM region, because this region has a lower coupling energy compared to that of the ordered P3HT region. The two distinct differences in the J-V curves of

ordered and disordered P3HT stem from the fact that their currents are limited by the PCBM and disordered P3HT regions, respectively.

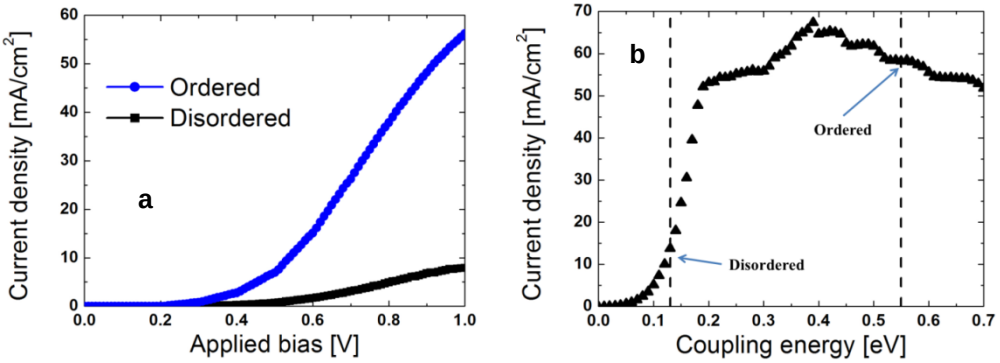

Figure 59. (a) Dark current-voltage curve of ordered (blue) and disordered (black) P3HT:PCBM averaged over all HOMO/LUMO energy mismatch values according to their frequency distributions. (b) Changes of the average dark forward current at 1V applied bias as a function of P3HT coupling energy. Peak current density at 1V applied bias was observed at 0.39 eV P3HT coupling energy.

J-V curves (c.f. Figure 58a,b) were then mixed according to the HOMO/LUMO energy gap distribution (c.f. Figure 55f) in order to obtain the cumulative dark J-V curve, which should include the effect of thermal fluctuation on the morphology and consequently the electronic of the system. From the resulting cumulative J-V curve (c.f. Figure 59a), we can see that the maximum dark current obtained at 1V applied bias is about 56 mA·cm^{-2} and 8 mA·cm^{-2} for ordered and disordered P3HT respectively. These results are about 10 and 1.5 times higher than our experimental results (c.f. Figure 51a) in the case of ordered and disordered P3HT respectively. The deviation between calculated and observed results could be due to three reasons: (1) the actual device is a mix between ordered and disordered P3HT, hence in most cases the dark current obtained should be less than for a fully ordered structure. This can help to understand that the deviation is much larger for the case of ordered P3HT. (2) The effect of charge scattering is not included in our model. As it has been demonstrated that phonon scattering could reduce charge mobility by up to three times[157]; a considerably lower transport efficiency should be expected in an actual device. (3) As the model under consideration is 1-D, it implicitly assumes perfect charge percolation. In contrast isolated domains in the intricate donor/acceptor

network of real bulk-heterojunction OPV could further reduce transport efficiency. Furthermore, the cumulative J-V result also suggests that charge hopping efficiency in ordered P3HT is about 7 times higher than in the disordered state. Experimentally, it was observed that a fully amorphous P3HT layer could have an about 3 orders of magnitude smaller charge mobility than ordered P3HT.[153] However, in our DFT calculations, disordered P3HT still exhibits perfect long range order (due to periodic boundary condition), so a real system may exhibit longer percolation pathways and weaker coupling energy leading to a further reduction in mobility.

The plot of the average current density at 1V applied bias as a function of P3HT coupling energy (c.f. Figure 59b) shows that charge transport efficiency reaches its maximum at a P3HT coupling energy of 0.39 eV, which is substantially higher than the 0.07 eV turning point observed in the energy barrier graph (c.f. Figure 57d). This is because higher coupling energy induces higher charge hopping rate (c.f. Equation (4.7)). The combined effect of rising hopping rate and increasing energy barrier after the 0.07 eV turning point leads to an optimal charge transfer efficiency observed at 0.39 eV. This value, however, should not be universal since different donor/acceptor systems would have different sets of geometry parameters. Based on the presented framework, it is possible to optimize both the geometry and coupling strength to boost transport efficiency. The results obtained in Figure 59b were calculated with the P3HT intra-layer spacing of 4.07 Å, an average between the computed ordered and disordered spacing values (c.f. Table 10).

3.4.4.Leakage Currents

As can be seen from Figure 58, the onset of the dark J-V curve is determined by the interfacial HOMO/LUMO mismatch regardless of the underlying active layer morphology. This means that during illumination, a leakage current is expected which would reduce the device fill factor and, consequently, efficiency.[158] To reduce the

leakage current and improve device performance, we need to increase the onset of the dark J-V curve which can be done by increasing the HOMO/LUMO mismatch at the interface. Here we have investigated the relation between interfacial morphology and HOMO/LUMO mismatch and found that there is a strong correlation between the distance from the centroid of the phenyl group on the PCBM to the centroid of the nearest thiophene ring and the interfacial HOMO/LUMO mismatch (c.f. Figure 60). This is reasonable since the close proximity between the phenyl group and the thiophene ring would enhance the chemical interaction, hence enlarging the HOMO/LUMO gap. It is interesting to note that an analogous analysis of fullerene cages does not yield any discernible trend. This suggests that reduction of leakage current can be tailored by reducing the distance between the phenyl group and the thiophene ring at the interface. Nevertheless, a deeper analysis of the effect of molecular orientation at the interface is needed and beyond the scope of this project.

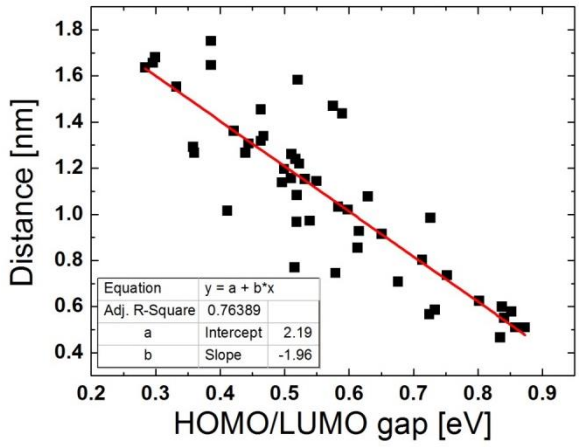

Figure 60. Variation of interfacial HOMO/LUMO mismatch as a function of the smallest distance between centroids of 6-member rings on PCBM and thiophene rings on P3HT.

3.5. Chapter Summary

In this chapter we have discussed charge transport in an OPV system studied within the framework of our model based on extended Hückel method and Marcus theory. The approach was validated with experimental results of light absorption and dark current voltage behaviour in P3HT:PCBM OPV. Conclusions regarding the device physics drawn from our study include that intra-molecular 1-2 and 1-3 hoppings are the dominant contributions to absorption peaks in P3HT and the overlapped energy required to optimize charge transport in P3HT:PCBM OPV. We have also seen how morphological tuning at the interface could lead to reduced leakage current and, consequently, improved photovoltaics performance, for instance the reduction in distance between phenyl group and thiophene ring at the interface should lead to a desirable lower leakage current in P3HT:PCBM based devices. The model is general enough that it could be applied to other OPV systems utilizing similar conjugated polymers: fullerene derivatives system or even all polymer systems and can be employed as a robust tool to probe new OPV systems with respect to their tentative performance prior to materials synthesis and device fabrication.

While we also included thermal fluctuation and morphological information into the model via various geometry parameters such as donor:acceptor spatial separation at the interface and intra layer spacing for both P3HT and PCBM, the model under investigation in this work is still limited to the 1-D device model. This means that charge percolation that could become important in a 3-D extended network of donor:acceptor bulk heterojunction were not covered by the model. Despite the many insightful conclusions that have been drawn from the studies, extending the model to higher dimension could be useful in further understanding the correlation between the active layer morphology and the device charge transport performance.

CHAPTER 4: Project Summary and OPV Outlook

4.1. Project Summary

In this work, we have studied the morphology of the active layer in bulk heterojunction P3HT:PCBM OPV using a combination of DFT, MD, coarse-grained MD and MC simulation techniques. We started by adapting the atomistic forcefield available in literature and benchmarked them against accurate first-principles DFT calculations. Coarse-graining was then performed by representing each rigid group of atoms with a bead following rigidity analysis of MD simulations in molten state. This coarse-graining allowed us to bring down the number of simulated atoms to a tenth in a typical 1:1 weight ratio blend of similar size. Time scale analysis suggests that the coarse-grained forcefield enjoyed a further 10 times faster dynamics rate due to the smoother molecular surface compared to the atomistic version. Overall, the coarse-grained forcefield is thus about 100 times faster than the atomistic forcefield for a 1:1 weight ratio P3HT:PCBM blend of identical size.

Using the coarse-grained forcefield, we studied the interface between P3HT and PCBM at different P3HT orientations with ambient temperature of 450 K similar to experimental thermal treatment condition. The results suggest that higher crystallinity is to be expected nearer to the interfacial regions and that crystalline P3HT forms a more stable interface with PCBM compared to amorphous P3HT while face-on configuration is most stable. Furthermore, the intercalation analysis of C_{60} into P3HT suggests that PCBM diffusion into amorphous P3HT is due mainly to side chain activation while limited to boundary diffusion in case of crystalline P3HT. From these findings we propose a 3-step phase separation model in P3HT:PCBM bulk heterojunction as followed: (1) Minimisation of system energy will take place via the

nucleation of P3HT crystallites. (2)The growth of P3HT crystals will push adjacent PCBM molecules out of the crystalline P3HT regions. (3) Grain boundaries between P3HT crystallites will contain PCBM and act as diffusion pathways for the redistribution of PCBM to PCBM-rich regions.

To effectively model the final phase-separated structure of P3HT:PCBM with manageable computational effort, P3HT:PCBM interfacial energy changes as a function of underlying P3HT layer was simulated using the coarse-grained model. The resulting profile follows an error function-dependence and the parametrised profile was then fed into MC simulations utilizing systematically varied starting conditions (different P3HT weight fraction of fully mixed structure and a bilayer structure). The cells chosen for MC simulation are $(100nm)^3$ in volume and periodic in **x** and **y** directions, thus are representative of an 100 nm thick active layer in a typical fabricated OPV device. We then studied the phase separation process of a P3HT:PCBM blend at different P3HT weight ratios (0.2, 0.35, 0.5, 0.65 and 0.8). After 1,500 million MC cycles, the system reaches a steady state where more than 98% of the cell volume is >80% phase-pure for all blend ratios. Further analysis indicates that the 1:1 blend ratio gives the optimal morphology in term of domain size, balancing percolating volume and interface areas of percolating domain for both P3HT and PCBM. We thus conclude that for a typical solution processed bulk heterojunction P3HT:PCBM, a blend ratio of 1:1 is recommended. To introduce a higher degree of active morphology control, deployment of P3HT seed crystals at the bottom contact prior to thermal annealing was suggested. Seed crystals allow slight enhancement of P3HT domain size and a formation of tri-layer donor:acceptor:donor morphology which is elusive in non-seeded cases (both donor:acceptor:donor and acceptor:donor:acceptor can form with equal probability). Seed packing density of ~10% is shown to be ideal for the enhancement of domain size and charge transport pathway dimensionality, thus we suggest a new P3HT:PCBM bulk heterojunction

deposition route which includes uniform seeding (at packing density of ~10%) at the bottom contact and a deposited film of ~200 nm thickness. This is followed by dissection of active layer into half. The remnant would have domain size, domain percolation and donor/acceptor concentration gradient suitable for OPV applications. Alternate seeding of P3HT and PCBM crystals at the bottom and top contact respectively is also expected to produce favourable concentration gradient within the active layer.

For charge transport, we formulated a transport model based on extended Hückel method and Marcus theory. This model was first used exclusively for modelling of charge transport in conjugated polymeric semiconductors. Applying the model to P3HT with metal-like electrodes we demonstrated that electric current flown in P3HT is a predominantly intra-chain transport while light absorption is associated to inter-chain transport. In addition, 1-2 and 1-3 hoppings were shown to be closely related to the peak at 500 nm and the shoulder at 600 nm observed experimentally in the absorption spectra of crystalline P3HT. Following this, we extend the model focus mainly on inter-molecular charge transport to effectively model the J-V curve flowing in the active layer. This was done by extending the Hamiltonian to include both the P3HT and PCBM layer in a bilayer cell. Morphology and electronics information are obtained from both dynamics (both coarse-grained and atomistic models) and DFT calculations. The results obtained from the model suggest that there is an optimal charge mobility associated with P3HT coupling energy of 0.4 eV which is mid-way between fully crystalline and amorphous case. Furthermore, the relative distance between thiophene ring on P3HT and phenyl group on PCBM was also shown to play a role on the interfacial HOMO/LUMO mismatch and the device leakage current with smaller distance led to bigger mismatch and smaller leakage current.

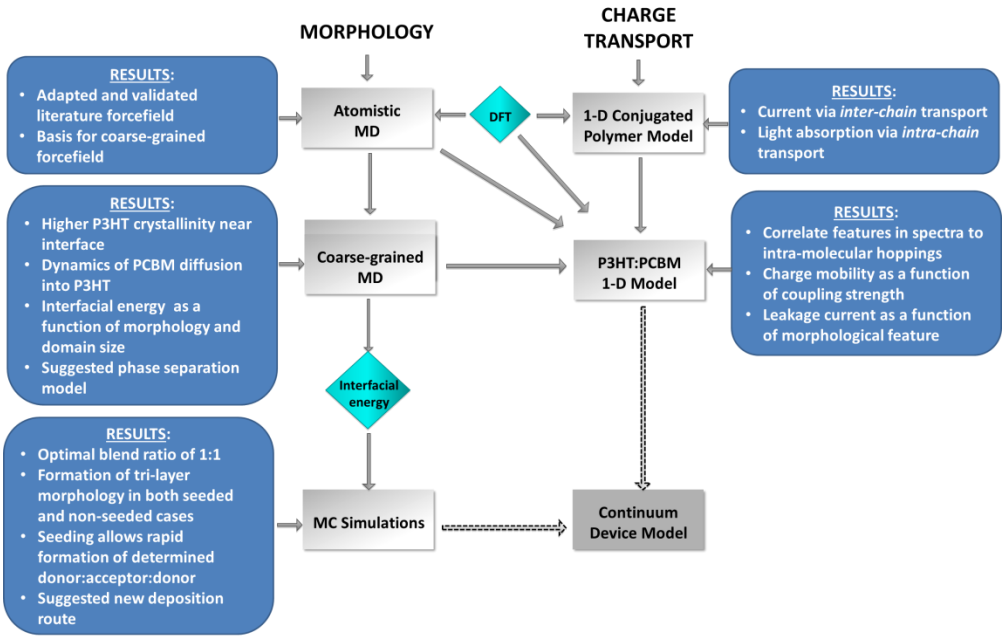

Figure 61. Flow chart of the work done as well as a short summary of the results obtained at each stage. The results shown here can be fed into continuum device model for more robust macroscopic device modelling. The methodology is general enough to be used for other OPV systems.

A summary of the work done in this thesis together with the key results are shown in Figure 61. The results shown here can then be fed into computationally efficient continuum level device simulations for promoting the understanding of device physics at the macroscopic scale. Furthermore, the generality of the methodology presented means that it can be applied to similar systems to aid in molecular designs relevant for high performance OPV.

4.2. Towards a Complete Theoretical Understanding

The results obtained from this work constitute just a first step towards a more complete understanding of OPV physics. Reaching the final goal of a continuous and consistent theory spanning from atomistic to device-level requires further expansion of the current work, which is laid out in this section.

First, we have successfully simulated the P3HT:PCBM blend morphology at the device level using MC technique (c.f. Section 2.4). The results obtained from which can be fed directly into continuum device simulations model available in literature.[159,

[160] MC simulations performed in this case were based solely on the interfacial energy profile obtained from coarse-grained MD simulations. Thus to derive analogous results for other donor:acceptor couples, it is now clear that a suitable approach would be to derive a domain-size dependent interfacial energy profile. In this work, we suggested that the interfacial energy profile should follow the functional form $E(L) = E_0(L) \cdot \mathrm{erf}\left(\frac{L}{\lambda^*}\right)$ (c.f. Equation 3.14) since such a property should be strongly dependent on the Coulomb interactions between various donor and acceptor layers. Based on this assumption the morphological evolution in OPV will be mainly controlled by two parameters, namely $E_0(L)$ (interfacial energy for bulk donor and acceptor) and λ^* (the effective screening length). Establishing a correlation of these two parameters with the chemical and physical properties, and possibly the chemical structures, of the respective materials, will allow to directly predict the morphology of the blend even before carrying out the experiment. Given that the domain size and dimension directly affect charge percolation, these parameters should hold paramount importance to the device performance.

On the other hand, the resultant tri-layer morphology seems to be a product of the interfacial energy profile functional form rather than the values of $E_0(L)$ and λ^*. This means that techniques used for controlling of morphology evolution in P3HT:PCBM blend is expected to be applicable to compatible systems. This implies that a plethora of results obtained for the renowned P3HT:PCBM systems is still valid should another similar OPV system prove to be more stable and yield better conversion efficiency.

Second, using the 1-dimensional charge transport model, we have established the interfacial conditions such that optimal charge transport and extraction can be achieved. Extension of the model to higher dimension is of great interest to OPV research since real devices are in 3-dimensional, hence, actual interface could be a lot

more complicated since they can take on complex shapes at possibly different blend which are not captured by the presented model. Furthermore, a link between interfacial coupling energy, HOMO/LUMO level and parameters relevant for interfacial energy profile ($E_0(L)$ and λ^*) still remains to be identified. If we can understand this link, its origin and how modifications at the molecular level could change them, then establishing a connection between device performance and morphology becomes much more achievable. This connection can then facilitate a seamless connection from respective donor:acceptor chemical structures all the way to expected device performance.

In short, the future extension of this work should focus on elucidating the correlation between interfacial coupling energy, HOMO/LUMO level, $E_0(L)$, λ^* and the chemical structures of donor and acceptor materials. This can be done with the help of a 3-dimensional charge transport based on the framework of the 1-dimensional charge transport described in this thesis. Since these four parameters characterize the morphology and charge transport properties, the complete understanding of them could drive a derivation of a more OPV specific continuum device model. Such a model would be very useful in systematically improving OPV performance by refining device fabrications, architecture and molecular design of new donor and acceptor materials.

4.3. OPV Outlook

Looking at laboratory scale OPV devices, it is easy to see the tremendous improvement in terms of efficiency within the past 5-6 years. Yet this is still not enough to make OPV a commercially viable and a force to be reckoned with in the renewable energy sector or even within the photovoltaics domain. This is partly due to the still limited efficiency, stability and the many difficulties faced by the renewable energy sector as a whole. While it has been argued that grid parity has

been reached in many countries[161], the currently enjoyed low solar panel cost could be due to over-capacity so that prices could spring back up, making photovoltaics a more costly option for power plants in the near future.[162] Furthermore, photovoltaic devices typically have low load factor (<40% compared to 90% in coal fire plant and >95% in nuclear plant)[163, 164], steep initial capital (due to low load factor)[165], high maintenance cost (regular cleaning is required in dusty ambient condition)[165] and performance degradation with high temperature (which makes photovoltaics less productive in hot weather).[166] As a result, despite the exponential increase in installed photovoltaics capacity observed worldwide[161], we do not expect it to overcome any traditional energy sources in the near future.

On the other hand, because of steep competition in the renewable energy sector especially from silicon-based solar cell, OPV have been occupying a humble market share[49] and would remain so for the many years to come due to the following reasons: (1) the pervasiveness of Si-based solar panels in the photovoltaics sector thanks to the developed technologies, high efficiency and guaranteed life span of up to 25 years;[161] (2) the market is currently facing over-capacity of solar panels which means that price of silicon-based solar panel would remain low for a foreseeable future, hence creating little chance for alternative photovoltaic technologies; (3) steep competitions from alternative renewable energy technologies such as wind energy, hydropower and solar thermal.[164, 167, 168] However, while it is not certain if OPV would ever become a major player in the renewable energy sector (or even in the photovoltaics sector), its ability to form flexible modules means it has potential applications in mobile devices where reduced thickness, flexibility and light weight of a power source may play a very important role. In building application, OPV thin films of approximately 100 nm thick could be incorporated into shaded glass with the generated electricity used for low power applications. Even in such cases a minimal life span of 5 years may be required of the device.

Thus while OPV is a potential candidate for low cost photovoltaics alternative with significantly smaller energy penalty, it is unclear if the technology would ever be in the mainstream energy generation sources unless some major breakthrough is to be achieved. Raising the overall efficiency and improving the device life span would be on top of the list. Alternatively, tandem cell could be used instead but this will raise the overall cost and reduced OPV attractiveness. In any case, OPV is still much in the initial development stage and would not be readily available in the market any time soon.

Despite this unsure outlook of commercial success of OPV, much effort has been committed globally to improve OPV commercial viability and this work is a part of it. Technically, OPV has some distinct advantages that allow them to be manufacture at a much faster rate, lower temperature and cheaper cost. Further work needs to be done to rectify some of its shortcomings and, thereby, making the technology more mature. To this end a solid theoretical framework is crucial and needs to be improved upon such that experimental work can be guided towards new materials, new device architecture and possibly new grid integration methods compared to silicon-based solar panels. The work done here may just be a "drop in the limitless ocean, but what is an ocean but a multitude of drops". Here we have successfully established a correlation between morphology and device performance as well as the guiding principle of device morphology and suggestions on how to engineer the most optimal active layer. Further work that seeks to establish the connection between microscopic properties (molecular energy levels, nano-scale morphology) and macroscopic properties (charge transport, device performance) should be encouraged so that a continuous theoretical framework can be established from most fundamental (molecular level) to most experimentally relevant (device level) which would no doubt form a backbone for OPV research and a conducive catalyst for a

breakthrough. Such results could also be carried over to its sister technology OLED which is doing really well commercially.

In a concluding remark, the author hopes that the work presented here would spark interest in further theoretical explorations of OPV especially focusing on bridging the gap between molecular level and device level (a model that was very successfully done on silicon-based solar cell). If such a goal is to be achieved, it should become clear in no time if OPV technology is to overtake its inorganic counter-part as a main player in the photovoltaics market.

CHAPTER 5: List of Publications

Peer-Reviewed Journal Publications

To, T.T. and S. Adams, "Molecular understanding of charge transport in P3HT:PCBM organic solar cell". Computational Materials Science, 2014. **Submitted**

To, T.T. and S. Adams, "Modelling of P3HT:PCBM interface using coarse-grained forcefield derived from accurate atomistic forcefield". Physical Chemistry Chemical Physics, 2014. **16**(10): p. 4653-4663

To, T.T. and S. Adams, "Charge transport and light absorption in conjugated systems from extended Hückel method and Marcus theory". International Journal of Computational Materials Science and Engineering, 2012. **01**(02): p. 1250020

To, T.T. and S. Adams, "Accurate Poly(3-hexylthiophene) Forcefield from First-Principle Modelling". Nanoscience and Nanotechnology Letters, 2012. **4**(7): p. 703-711

Conference Proceeding

To, T.T.; Yap, J.H.; Rao, R.P. and S. Adams, "Phase Separated Morphology of P3HT:PCBM Bulk Heterojunction from Coarse-Grained Molecular Dynamics and Monte Carlo Simulation". 2013 MRS Fall Meeting proceedings, 2014. **1663**: DOI: 10.1557/opl.2014.87

International Conference Contributions

Oral Presentations

To, T.T. and S. Adams, *"Coarse-grained Modelling of P3HT:PCBM Interface as a Function of P3HT Polymer Chain Orientations"*. International Conference on Materials for Advanced technologies ICMAT 2013, 3 Jun - 5 Jul 2013, Singapore

To, T.T. and S. Adams, *"From Atomistic to Coarse-grained Modelling of Morphology Evolution in P3HT:PCBM Solar Cells"*. International Conference on Simulation of Organic Electronics and Photovoltaics SimOEP12, 11 - 14 Jun 2012, Valencia, Spain

Poster Presentations

To, T.T. and S. Adams, *"Molecular understanding of charge transport in P3HT:PCBM organic solar cell"*. 4th Trilateral Conference on Advances in Nanoscience 2013, 5 - 7 Dec 2013, Singapore

To, T.T.; Yap, J.H.; Rao, R.P. and S. Adams, *"Phase separated morphology of P3HT:PCBM bulk heterojunction from coarse-grained Molecular Dynamics and Monte Carlo simulations"*. Materials Research Society Fall Meeting 2013, 1 - 6 Dec 2013, Boston, United States

To, T.T. and S. Adams, *"Coarse-Grained Forcefield for P3HT:PCBM and its application to PCBM Diffusion into P3HT"*. Materials Research Society Spring Meeting 2013, 1 - 5 Apr 2013, San Francisco, United States

To, T.T. and S. Adams, *"Coarse-grained Forcefield for Efficient Analysis of Morphology in P3HT:PCBM Bulk Heterojunction Solar Cells"*. 5th MRS-S Conference on Advanced Materials, 20 - 22 Mar 2012, Singapore

To, T.T. and S. Adams, *"Charge transport and light absorption in conjugated systems from extended Hückel method and Marcus theory"*. 6th Conference of the Asian Consortium on Computational Materials Science ACCMS-6, 6 - 9 Sep 2011, Singapore

To, T.T. and S. Adams, *"Accurate P3HT Forcefield from Ab Initio Modelling"*. International Conference on Materials for Advanced Technologies ICMAT 2011, 26 Jun - 1 Jul 2011, Singapore

References

1. Akamatu, H.; Inokuchi, H.; Matsunaga, Y. *Nature* **1954,** 173, (4395), 168-169.
2. Chiang, C. K.; Druy, M. A.; Gau, S. C.; Heeger, A. J.; Louis, E. J.; MacDiarmid, A. G.; Park, Y. W.; Shirakawa, H. *J. Am. Chem. Soc.* **1978,** 100, (3), 1013-1015.
3. Chamberlain, G. A. *Solar Cells* **1983,** 8, (1), 47-83.
4. Choulis, S. A.; Kim, Y.; Nelson, J.; Bradley, D. D. C.; Giles, M.; Shkunov, M.; McCulloch, I. *Appl. Phys. Lett.* **2004,** 85, (17), 3890-3892.
5. Sakurai, K.; Tachibana, H.; Shiga, N.; Terakura, C.; Matsumoto, M.; Tokura, Y. *Phys. Rev. B* **1997,** 56, (15), 9552-9556.
6. Tang, C. W. *Appl. Phys. Lett.* **1986,** 48, (2), 183-185.
7. Markov, D. E.; Amsterdam, E.; Blom, P. W. M.; Sieval, A. B.; Hummelen, J. C. *J. Phys. Chem. A* **2005,** 109, (24), 5266-5274.
8. Yu, G.; Gao, J.; Hummelen, J. C.; Wudl, F.; Heeger, A. J. *Science* **1995,** 270, (5243), 1789-1791.
9. Wu, W.-R.; Jeng, U. S.; Su, C.-J.; Wei, K.-H.; Su, M.-S.; Chiu, M.-Y.; Chen, C.-Y.; Su, W.-B.; Su, C.-H.; Su, A.-C. *Acs Nano* **2011,** 5, (8), 6233-6243.
10. Deibel, C.; Dyakonov, V. *Rep. Prog. Phys.* **2010,** 73, (9), 096401.
11. Green, M. A.; Emery, K.; Hishikawa, Y.; Warta, W.; Dunlop, E. D. *Prog. Photovoltaics Res. Appl.* **2013,** 21, (5), 827-837.
12. Green, M. A.; Emery, K.; Hishikawa, Y.; Warta, W.; Dunlop, E. D. *Prog. Photovoltaics Res. Appl.* **2014,** 22, (1), 1-9.
13. Green, M. A.; Emery, K.; King, D. L.; Hishikawa, Y.; Warta, W. *Prog. Photovoltaics Res. Appl.* **2006,** 14, (5), 455-461.
14. Green, M. A.; Emery, K.; Hisikawa, Y.; Warta, W. *Prog. Photovoltaics Res. Appl.* **2007,** 15, (5), 425-430.
15. Green, M. A.; Emery, K.; Hishikawa, Y.; Warta, W. *Prog. Photovoltaics Res. Appl.* **2008,** 16, (5), 435-440.
16. Green, M. A.; Emery, K.; Hishikawa, Y.; Warta, W. *Prog. Photovoltaics Res. Appl.* **2009,** 17, (5), 320-326.
17. Green, M. A.; Emery, K.; Hishikawa, Y.; Warta, W. *Prog. Photovoltaics Res. Appl.* **2010,** 18, (5), 346-352.
18. Green, M. A.; Emery, K.; Hishikawa, Y.; Warta, W.; Dunlop, E. D. *Prog. Photovoltaics Res. Appl.* **2011,** 19, (5), 565-572.
19. Green, M. A.; Emery, K.; Hishikawa, Y.; Warta, W.; Dunlop, E. D. *Prog. Photovoltaics Res. Appl.* **2012,** 20, (1), 12-20.
20. Green, M. A.; Emery, K.; Hishikawa, Y.; Warta, W.; Dunlop, E. D. *Prog. Photovoltaics Res. Appl.* **2012,** 20, (5), 606-614.
21. Kaake, L. G.; Moses, D.; Heeger, A. J. *J. Phys. Chem. Lett.* **2013,** 4, 2264-2268.
22. Topp, K.; Borchert, H.; Johnen, F.; Tunc, A. V.; Knipper, M.; von Hauff, E.; Parisi, J.; Al-Shamery, K. *J. Phys. Chem. A* **2009,** 114, (11), 3981-3989.
23. Png, R.-Q.; Chia, P.-J.; Tang, J.-C.; Liu, B.; Sivaramakrishnan, S.; Zhou, M.; Khong, S.-H.; Chan, H. S. O.; Burroughes, J. H.; Chua, L.-L.; Friend, R. H.; Ho, P. K. H. *Nat Mater* **2010,** 9, (2), 152-158.
24. Peet, J.; Kim, J. Y.; Coates, N. E.; Ma, W. L.; Moses, D.; Heeger, A. J.; Bazan, G. C. *Nat. Mater.* **2007,** 6, (7), 497-500.
25. Slooff, L. H.; Veenstra, S. C.; Kroon, J. M.; Moet, D. J. D.; Sweelssen, J.; Koetse, M. M. *Appl. Phys. Lett.* **2007,** 90, (14), 143506.
26. Park, S. H.; Roy, A.; Beaupre, S.; Cho, S.; Coates, N.; Moon, J. S.; Moses, D.; Leclerc, M.; Lee, K.; Heeger, A. J. *Nat. Photonics* **2009,** 3, (5), 297-302.

27. Halls, J. J. M.; Walsh, C. A.; Greenham, N. C.; Marseglia, E. A.; Friend, R. H.; Moratti, S. C.; Holmes, A. B. *Nature* **1995,** 376, (6540), 498-500.
28. Yu, G.; Heeger, A. J. *J. Appl. Phys.* **1995,** 78, (7), 4510-4515.
29. Facchetti, A. *Mater. Today* **2013,** 16, (4), 123-132.
30. Polyera Polyera Achieves 6.4% All-Polymer Organic Solar Cells. http://www.polyera.com/newsflash/polyera-achieves-6-4-all-polymer-organic-solar-cells
31. Sapkota, S. B.; Fischer, M.; Zimmermann, B.; Würfel, U. *Sol. Energ. Mat. Sol. C.* **2014,** 121, (0), 43-48.
32. Kaduwal, D.; Zimmermann, B.; Würfel, U. *Sol. Energ. Mat. Sol. C.* **2014,** 120, Part B, (0), 449-453.
33. Zhu, R.; Chung, C.-H.; Cha, K. C.; Yang, W.; Zheng, Y. B.; Zhou, H.; Song, T.-B.; Chen, C.-C.; Weiss, P. S.; Li, G.; Yang, Y. *Acs Nano* **2011,** 5, (12), 9877-9882.
34. Tyler, T. P.; Brock, R. E.; Karmel, H. J.; Marks, T. J.; Hersam, M. C. *Adv. Energy Mat.* **2011,** 1, (5), 785-791.
35. Kaduwal, D.; Schleiermacher, H.-F.; Schulz-Gericke, J.; Kroyer, T.; Zimmermann, B.; Würfel, U. *Sol. Energ. Mat. Sol. C.* **2014,** 124, (0), 92-97.
36. Wong, K. H.; Ananthanarayanan, K.; Luther, J.; Balaya, P. *J. Phys. Chem. C* **2012,** 116, (31), 16346-16351.
37. Sun, Y.; Seo, J. H.; Takacs, C. J.; Seifter, J.; Heeger, A. J. *Adv. Mater.* **2011,** 23, (14), 1679-1683.
38. Jørgensen, M.; Norrman, K.; Krebs, F. C. *Sol. Energ. Mat. Sol. C.* **2008,** 92, (7), 686-714.
39. Paci, B.; Generosi, A.; Albertini, V. R.; Perfetti, P.; de Bettignies, R.; Leroy, J.; Firon, M.; Sentein, C. *Appl. Phys. Lett.* **2006,** 89, (4), 043507-3.
40. Wang, J.-C.; Lu, C.-Y.; Hsu, J.-L.; Lee, M.-K.; Hong, Y.-R.; Perng, T.-P.; Horng, S.-F.; Meng, H.-F. *J. Mater. Chem.* **2011,** 21, (15), 5723-5728.
41. Yeh, N.; Yeh, P. *Renew. Sust. Energ. Rev.* **2013,** 21, (0), 421-431.
42. Hwajeong, K.; Minjung, S.; Youngkyoo, K. *Europhys. Lett.* **2008,** 84, (5), 58002.
43. Jørgensen, M.; Norrman, K.; Gevorgyan, S. A.; Tromholt, T.; Andreasen, B.; Krebs, F. C. *Adv. Mater.* **2012,** 24, (5), 580-612.
44. Frederik C, K. *Sol. Energ. Mat. Sol. C.* **2009,** 93, (4), 465-475.
45. Espinosa, N.; García-Valverde, R.; Urbina, A.; Krebs, F. C. *Sol. Energ. Mat. Sol. C.* **2011,** 95, (5), 1293-1302.
46. Lungenschmied, C.; Dennler, G.; Neugebauer, H.; Sariciftci, S. N.; Glatthaar, M.; Meyer, T.; Meyer, A. *Sol. Energ. Mat. Sol. C.* **2007,** 91, (5), 379-384.
47. Krebs, F. C.; Spanggaard, H. *Chem. Mater.* **2005,** 17, (21), 5235-5237.
48. Roes, A. L.; Alsema, E. A.; Blok, K.; Patel, M. K. *Prog. Photovoltaics Res. Appl.* **2009,** 17, (6), 372-393.
49. Espinosa, N.; Hosel, M.; Angmo, D.; Krebs, F. C. *Energ. Environ. Sci.* **2012,** 5, (1), 5117-5132.
50. Masson, G.; Latour, M.; Rekinger, M.; Theologitis, I.-T.; Papoutsi, M. *Global Market Outlook for Photovoltaics (2013-2017)*; European Photovoltaic Industry Association (EPIA): 2013.
51. Mühlbacher, D.; Scharber, M.; Morana, M.; Zhu, Z.; Waller, D.; Gaudiana, R.; Brabec, C. *Adv. Mater.* **2006,** 18, (21), 2884-2889.
52. Scharber, M. C.; Mühlbacher, D.; Koppe, M.; Denk, P.; Waldauf, C.; Heeger, A. J.; Brabec, C. J. *Adv. Mater.* **2006,** 18, (6), 789-794.
53. Gregg, B. A.; Hanna, M. C. *J. Appl. Phys.* **2003,** 93, (6), 3605-3614.
54. To, T. T.; Adams, S. *Int. J. Comput. Mater. Sci. Eng.* **2012,** 01, (02), 1250020.
55. Center, R. R. D., Solar Radiation Spectrum. In 2003.

56. Ma, W.; Yang, C.; Gong, X.; Lee, K.; Heeger, A. J. *Adv. Funct. Mater.* **2005,** 15, (10), 1617-1622.
57. Padinger, F.; Rittberger, R. S.; Sariciftci, N. S. *Adv. Funct. Mater.* **2003,** 13, (1), 85-88.
58. Watts, B.; Belcher, W. J.; Thomsen, L.; Ade, H.; Dastoor, P. C. *Macromolecules* **2009,** 42, (21), 8392-8397.
59. Yang, X.; Loos, J. *Macromolecules* **2007,** 40, (5), 1353-1362.
60. Hopkinson, P. E.; Staniec, P. A.; Pearson, A. J.; Dunbar, A. D. F.; Wang, T.; Ryan, A. J.; Jones, R. A. L.; Lidzey, D. G.; Donald, A. M. *Macromolecules* **2011,** 44, (8), 2908-2917.
61. Treat, N. D.; Brady, M. A.; Smith, G.; Toney, M. F.; Kramer, E. J.; Hawker, C. J.; Chabinyc, M. L. *Adv. Energy Mat.* **2011,** 1, (1), 82-89.
62. Carrillo, J.-M. Y.; Kumar, R.; Goswami, M.; Sumpter, B. G.; Brown, W. M. *Phys. Chem. Chem. Phys.* **2013,** 15, (41), 17873-17882.
63. Yin, W.; Dadmun, M. *Acs Nano* **2011,** 5, (6), 4756-4768.
64. To, T. T.; Adams, S. *Phys. Chem. Chem. Phys.* **2014,** 16, (10), 4653-4663.
65. Troisi, A.; Orlandi, G. *Phys. Rev. Lett.* **2006,** 96, (8), 086601.
66. Heinemann Marc, D.; Ananthanarayanan, K.; Thummalakunta, L. N. S. A.; Yong Chian, H.; Luther, J. *Green* **2011,** 1, (3), 291.
67. Bavel, S. S. v.; Sourty, E.; With, G. d.; Loos, J. *Nano Lett.* **2008,** 9, (2), 507-513.
68. Chirvase, D.; Parisi, J.; Hummelen, J. C.; Dyakonov, V. *Nanotechnology* **2004,** 15, (9), 1317.
69. van Bavel, S. S.; Barenklau, M.; de With, G.; Hoppe, H.; Loos, J. *Adv. Funct. Mater.* **2010,** 20, (9), 1458-1463.
70. Giridharagopal, R.; Ginger, D. S. *J. Phys. Chem. Lett.* **2010,** 1, (7), 1160-1169.
71. Koppe, M.; Brabec, C. J.; Heiml, S.; Schausberger, A.; Duffy, W.; Heeney, M.; McCulloch, I. *Macromolecules* **2009,** 42, (13), 4661-4666.
72. Xue, B. F.; Vaughan, B.; Poh, C. H.; Burke, K. B.; Thomsen, L.; Stapleton, A.; Zhou, X. J.; Bryant, G. W.; Belcher, W.; Dastoor, P. C. *J. Phys. Chem. C* **2010,** 114, (37), 15797-15805.
73. Beal, R. M.; Stavrinadis, A.; Warner, J. H.; Smith, J. M.; Assender, H. E.; Watt, A. A. R. *Macromolecules* **2010,** 43, (5), 2343-2348.
74. Chen, D.; Liu, F.; Wang, C.; Nakahara, A.; Russell, T. P. *Nano Lett.* **2011,** 11, (5), 2071-2078.
75. Kohn, P.; Rong, Z.; Scherer, K. H.; Sepe, A.; Sommer, M.; Müller-Buschbaum, P.; Friend, R. H.; Steiner, U.; Hüttner, S. *Macromolecules* **2013,** 46, (10), 4002-4013.
76. Jorgensen, W. L.; Maxwell, D. S.; Tirado-Rives, J. *J. Am. Chem. Soc.* **1996,** 118, (45), 11225-11236.
77. Marcon, V.; Raos, G. *J. Phys. Chem. B* **2004,** 108, (46), 18053-18064.
78. Cheung, D. L.; McMahon, D. P.; Troisi, A. *J. Phys. Chem. B* **2009,** 113, (28), 9393-9401.
79. Cheung, D. L.; Troisi, A. *J. Phys. Chem. C* **2010,** 114, (48), 20479-20488.
80. Huang, D. M.; Faller, R.; Do, K.; Moulé, A. J. *J. Chem. Theory Comput.* **2009,** 6, (2), 526-537.
81. Huang, D. M.; Moule, A. J.; Faller, R. *Fluid Phase Equilib.* **2011,** 302, (1–2), 21-25.
82. Frigerio, F.; Casalegno, M.; Carbonera, C.; Nicolini, T.; Meille, S. V.; Raos, G. *J. Mater. Chem.* **2012,** 22, (12), 5434-5443.
83. Xue, J.; Hou, T.; Li, Y. *Appl. Phys. Lett.* **2012,** 100, (5), 053307-3.
84. Lee, C.-K.; Pao, C.-W.; Chu, C.-W. *Energ. Environ. Sci.* **2011,** 4, (10), 4124-4132.

85. Foiles, S. M.; Baskes, M. I.; Daw, M. S. *Phys. Rev. B* **1986,** 33, (12), 7983-7991.
86. Tersoff, J. *Phys. Rev. B* **1988,** 37, (12), 6991-7000.
87. Karasawa, N.; Goddard, W. A. *J. Phys. Chem.* **1989,** 93, (21), 7320-7327.
88. Berendsen, H. J. C.; Postma, J. P. M.; van Gunsteren, W. F.; DiNola, A.; Haak, J. R. *J. Chem. Phys.* **1984,** 81, (8), 3684-3690.
89. Hohenberg, P.; Kohn, W. *Phys. Rev.* **1964,** 136, (3B), B864-B871.
90. Kohn, W.; Sham, L. J. *Phys. Rev.* **1965,** 140, (4A), A1133-A1138.
91. Blöchl, P. E. *Phys. Rev. B* **1994,** 50, (24), 17953-17979.
92. Perdew, J. P.; Ernzerhof, M.; Burke, K. *J. Chem. Phys.* **1996,** 105, (22), 9982-9985.
93. Janesko, B. G. *J. Chem. Phys.* **2011,** 134, (18), 184105-8.
94. Geerlings, P.; De Proft, F.; Langenaeker, W. *Chem. Rev.* **2003,** 103, (5), 1793-1874.
95. Kresse, G.; Furthmüller, J. *Phys. Rev. B* **1996,** 54, (16), 11169.
96. Liu, S.; Lu, Y. J.; Kappes, M. M.; Ibers, J. A. *Science* **1991,** 254, (5030), 408-410.
97. Rispens, M. T.; Meetsma, A.; Rittberger, R.; Brabec, C. J.; Sariciftci, N. S.; Hummelen, J. C. *Chem. Commun.* **2003**, (17), 2116-2118.
98. To, T. T.; Adams, S. *Nanosci. Nanotechnol. Lett.* **2012,** 4, (7), 703-711.
99. Darling, S. B.; Sternberg, M. *J. Phys. Chem. B* **2009,** 113, (18), 6215-6218.
100. Mårdalen, J.; Samuelsen, E. J.; Gautun, O. R.; Carlsen, P. H. *Solid State Commun.* **1991,** 77, (5), 337-339.
101. Kayunkid, N.; Uttiya, S.; Brinkmann, M. *Macromolecules* **2010,** 43, (11), 4961-4967.
102. Rahimi, K.; Botiz, I.; Stingelin, N.; Kayunkid, N.; Sommer, M.; Koch, F. P. V.; Nguyen, H.; Coulembier, O.; Dubois, P.; Brinkmann, M.; Reiter, G. *Angew. Chem.* **2012,** 124, (44), 11293-11297.
103. Arosio, P.; Moreno, M.; Famulari, A.; Raos, G.; Catellani, M.; Meille, S. V. *Chem. Mater.* **2009,** 21, (1), 78-87.
104. Alexiadis, O.; Mavrantzas, V. G. *Macromolecules* **2013,** 46, (6), 2450-2467.
105. Moynihan, C. T.; Easteal, A. J.; Wilder, J.; Tucker, J. *J. Phys. Chem.* **1974,** 78, (26), 2673-2677.
106. Zen, A.; Saphiannikova, M.; Neher, D.; Grenzer, J.; Grigorian, S.; Pietsch, U.; Asawapirom, U.; Janietz, S.; Scherf, U.; Lieberwirth, I.; Wegner, G. *Macromolecules* **2006,** 39, (6), 2162-2171.
107. Zhao, J.; Swinnen, A.; Van Assche, G.; Manca, J.; Vanderzande, D.; Mele, B. V. *J. Phys. Chem. B* **2009,** 113, (6), 1587-1591.
108. Joshi, S.; Pingel, P.; Grigorian, S.; Panzner, T.; Pietsch, U.; Neher, D.; Forster, M.; Scherf, U. *Macromolecules* **2009,** 42, (13), 4651-4660.
109. Heffner, G. W.; Pearson, D. S. *Macromolecules* **1991,** 24, (23), 6295-6299.
110. Faller, R. *Polymer* **2004,** 45, (11), 3869-3876.
111. Depa, P.; Chen, C.; Maranas, J. K. *J. Chem. Phys.* **2011,** 134, (1), 014903-8.
112. Tschöp, W.; Kremer, K.; Batoulis, J.; Bürger, T.; Hahn, O. *Acta Polym.* **1998,** 49, (2-3), 61-74.
113. Ghosh, S. K. *Il Nuovo Cimento D* **1984,** 4, (3), 229-244.
114. Liu, T.; Cheung, D. L.; Troisi, A. *Phys. Chem. Chem. Phys.* **2011,** 13, (48), 21461-21470.
115. Xie, X.; Ju, H.; Lee, E. C. *J Korean Phys Soc* **2010,** 57, (1), 144-148.
116. Liu, T.; Troisi, A. *J. Phys. Chem. C* **2011,** 115, (5), 2406-2415.
117. Gould, H.; Tobochnik, J., *Statistical and Thermal Physics: With Computer Applications*. Princeton University Press: 2010.
118. Matsuo, T.; Suga, H.; David, W. I. F.; Ibberson, R. M.; Bernier, P.; Zahab, A.; Fabre, C.; Rassat, A.; Dworkin, A. *Solid State Commun.* **1992,** 83, (9), 711-715.

119. Olson, J. R.; Topp, K. A.; Pohl, R. O., Specific Heat and Thermal Conductivity of Solid Fullerenes. In *Phonon Scattering in Condensed Matter VII*, Meissner, M.; Pohl, R., Eds. Springer Berlin Heidelberg: 1993; Vol. 112, pp 42-43.
120. To, T. T.; Yap, J. H.; Rao, R. P.; Adams, S. *MRS Proceedings* **2014,** 1633, DOI: 10.1557/opl.2014.87.
121. Shaw, P. E.; Ruseckas, A.; Samuel, I. D. W. *Adv. Mater.* **2008,** 20, (18), 3516-3520.
122. Greene, L. E.; Law, M.; Yuhas, B. D.; Yang, P. *J. Phys. Chem. C* **2007,** 111, (50), 18451-18456.
123. Brédas, J.-L.; Cornil, J.; Beljonne, D.; dos Santos, D. A.; Shuai, Z. *Acc. Chem. Res.* **1999,** 32, (3), 267-276.
124. Bässler, H. *Phys. Status Solidi B* **1993,** 175, (1), 15-56.
125. Sasabe, H.; Tanaka, D.; Yokoyama, D.; Chiba, T.; Pu, Y.-J.; Nakayama, K.-i.; Yokoyama, M.; Kido, J. *Adv. Funct. Mater.* **2011,** 21, (2), 336-342.
126. Kergoat, L.; Herlogsson, L.; Braga, D.; Piro, B.; Pham, M.-C.; Crispin, X.; Berggren, M.; Horowitz, G. *Adv. Mater.* **2010,** 22, (23), 2565-2569.
127. Juricacute, I.; Batisticacute, I.; Tutiscaron, E. *Phys. Rev. B* **2010,** 82, (16), 165205.
128. Holstein, T. *Ann. Phys.* **1959,** 8, (3), 325-342.
129. Holstein, T. *Ann. Phys.* **1959,** 8, (3), 343-389.
130. Perroni, C. A.; Nocera, A.; Ramaglia, V. M.; Cataudella, V. *Phys. Rev. B* **2011,** 83, (24), 245107.
131. Su, W. P.; Schrieffer, J. R.; Heeger, A. J. *Phys. Rev. B* **1980,** 22, (4), 2099.
132. Kubo, R. *J. Phys. Soc. Jpn.* **1957,** 12, 570.
133. Cataudella, V.; De Filippis, G.; Perroni, C. A. *Phys. Rev. B* **2011,** 83, (16), 165203.
134. Liu, T.; Troisi, A. *Adv. Mater.* **2013,** 25, (7), 1038-1041.
135. Caruso, D.; Troisi, A. *Proceedings of the National Academy of Sciences* **2012,** 109, (34), 13498-13502.
136. McMahon, D. P.; Cheung, D. L.; Troisi, A. *J. Phys. Chem. Lett.* **2011,** 2, (21), 2737-2741.
137. Jortner, J. *J. Chem. Phys.* **1976,** 64, (12), 4860-4867.
138. Marcus, R. A. *Faraday Discussions of the Chemical Society* **1982,** 74, (0), 7-15.
139. Barbara, P. F.; Meyer, T. J.; Ratner, M. A. *The Journal of Physical Chemistry* **1996,** 100, (31), 13148-13168.
140. Petit, L.; Adamo, C.; Russo, N. *J. Phys. Chem. B* **2005,** 109, (24), 12214-12221.
141. Perpète, E. A.; Wathelet, V.; Preat, J.; Lambert, C.; Jacquemin, D. *J. Chem. Theory Comput.* **2006,** 2, (2), 434-440.
142. Casida, M. E. *Journal of Molecular Structure: THEOCHEM* **2009,** 914, (1–3), 3-18.
143. Coulson, C. A.; O'Leary, B.; Mallion, R. B., *Hückel theory for organic chemists*. Academic Press: 1978.
144. Marcus, R. A. *Rev. Mod. Phys.* **1993,** 65, (3), 599.
145. Galperin, Y. M., Introduction to Modern Solid State Physics. In 2008.
146. Hsu, C.-P. *Acc. Chem. Res.* **2009,** 42, (4), 509-518.
147. Voityuk, A. A.; Rosch, N. *J. Chem. Phys.* **2002,** 117, (12), 5607-5616.
148. Forcite Plus, Accelrys Inc., San Diego, CA **2008**, http://accelrys.com/products/datasheets/forcite-plus.pdf.
149. Youn, J. K.; et al. *J. Phys. D: Appl. Phys.* **2009,** 42, (7), 075412.
150. Park, Y.; Choong, V.; Gao, Y.; Hsieh, B. R.; Tang, C. W., *Work function of indium tin oxide transparent conductor measured by photoelectron spectroscopy*. AIP: 1996; Vol. 68, p 2699-2701.

151. Irwin, M. D.; Buchholz, D. B.; Hains, A. W.; Chang, R. P. H.; Marks, T. J. *Proceedings of the National Academy of Sciences* **2008,** 105, (8), 2783-2787.
152. http://www.world-aluminium.org/About+Aluminium/Benefits/Properties. accessed on 23/05/2012.
153. Sirringhaus, H.; Brown, P. J.; Friend, R. H.; Nielsen, M. M.; Bechgaard, K.; Langeveld-Voss, B. M. W.; Spiering, A. J. H.; Janssen, R. A. J.; Meijer, E. W.; Herwig, P.; de Leeuw, D. M. *Nature* **1999,** 401, (6754), 685-688.
154. Kline, R. J.; McGehee, M. D.; Toney, M. F. *Nat. Mater.* **2006,** 5, (3), 222-228.
155. Wong, M. K.; Wong, K. Y. *Synth. Met.* **2013,** 170, (0), 1-6.
156. To, T. T.; Adams, S. *Comput. Mater. Sci.* **2014,** Submitted.
157. Tang, L.; Long, M.; Wang, D.; Shuai, Z. *Sci. China Ser. B-Chem.* **2009,** 52, (10), 1646-1652.
158. Jun, G. H.; Jin, S. H.; Lee, B.; Kim, B. H.; Chae, W.-S.; Hong, S. H.; Jeon, S. *Energ. Environ. Sci.* **2013**.
159. Koster, L. J. A.; Smits, E. C. P.; Mihailetchi, V. D.; Blom, P. W. M. *Phys. Rev. B* **2005,** 72, (8), 085205.
160. Zhang, T.; Birgersson, E.; Luther, J. *J. Appl. Phys.* **2013,** 113, (17), 174505-10.
161. Breyer, C.; Gerlach, A. *Prog. Photovoltaics Res. Appl.* **2013,** 21, (1), 121-136.
162. Parra, V.; Carballo, T.; Cancillo, D.; Moralejo, B.; Martinez, O.; Jimenez, J.; Bullo; x; n, J.; Mi; guez, J. M.; Orda; s, R. In *Trends in crystalline silicon growth for low cost and efficient photovoltaic cells*, Electron Devices (CDE), 2013 Spanish Conference on, 12-14 Feb. 2013, 2013; 2013; pp 305-308.
163. MacKay, D. J. C. *Philosophical Transactions of the Royal Society A: Mathematical, Physical and Engineering Sciences* **2013,** 371, (1996).
164. Smil, V., *Energy Myths and Realities: Bringing Science to the Energy Policy Debate*. AEI Press: 2010.
165. Mathur, A.; Agrawal, G. D.; Chandel, M. *Renew. Sust. Energ. Rev.* **2013,** 17, (0), 104-109.
166. Nagengast, A.; Hendrickson, C.; Scott Matthews, H. *Energy and Buildings* **2013,** 64, (0), 493-502.
167. Jäger-Waldau, A., Photovoltaics photovoltaic (PV) , Status of. In *Sol Energy*, Richter, C.; Lincot, D.; Gueymard, C., Eds. Springer New York: 2013; pp 174-211.
168. Krozer, Y. *Renew Energ* **2013,** 50, (0), 68-73.

Appendix

A. Modified P3HT Forcefield

A.1. Forcefield

The forcefield presented here is based on the tetrathiophene model developed in 2004.[77] It was adapted to P3HT system by various groups.[78, 80] The full functional form of the forcefield can be seen in Section 2.2.1.1.

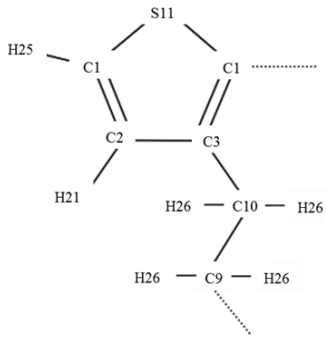

Figure. A1. Forcefield type notations for P3HT system used in this work

Forcefield Type	ϵ (kcal·mol^{-1})	σ (Å)	q (e)
C1	0.070	3.55	0.0748
C2	0.070	3.55	-0.1819
C3	0.070	3.55	-0.1979
C9	0.066	3.50	0
C10	0.066	3.50	0.1984
S11	0.250	3.55	-0.1496
H21	0.030	2.42	0.1561
H25	0.030	2.42	0.1919
H26	0.030	2.50	0

Table. A1. Diagonal Van der Waals parameters and charges

i	j	k_{bonds} (kcal·mol^{-1}·Å^2)	r_0 (Å)
C1	C1	787.20	1.446
C1	C2	1026.15	1.386
C1	C3	1026.15	1.386
C1	S11	581.42	1.726
C1	H21	740.98	1.080
C2	C3	895.80	1.436
C2	H21	740.98	1.080
C3	C10	906.44	1.499
C9	C9	646.02	1.525
C9	C10	646.02	1.525
C9	H26	682.00	1.112
C10	H26	682.00	1.112
C1	H25	740.98	1.080

Table. A2. Bond stretch parameters

i	j	k	k_{angle} (kcal·mol^{-1}·rad^{-2})	θ_0 (degree)
C1	C1	C2	109.35	127.67
C1	C1	C3	109.35	127.67
C1	C1	S11	83.45	120.76
C2	C1	S11	172.66	111.64
C3	C1	S11	172.66	111.64
H21	C1	S11	57.55	123.00
H21	C1	C2	70.50	125.10
H21	C1	C3	70.50	125.10
C1	C2	C3	79.13	110.28
H21	C2	C3	70.50	124.40
C1	C3	C2	79.13	110.28
C1	C3	C10	67.62	122.30
C2	C3	C10	67.62	122.30
C9	C9	C9	96.40	111.00
C9	C9	C10	96.40	111.00
C9	C9	H26	84.89	109.31
C10	C9	H26	84.89	109.31
H26	C9	H26	79.13	107.60
C3	C10	C9	77.70	110.60
C3	C10	H26	79.13	109.31
C9	C10	H26	84.89	109.31
H26	C10	H26	79.13	107.60
C1	S11	C1	172.66	91.63
H25	C1	S11	57.55	123.00
H25	C1	C2	70.50	125.10
H25	C1	C3	70.50	125.10
H21	C2	C1	70.50	125.10

Table. A3. Angle bend parameters

i	j	k	l	V_1(kcal·mol^{-1})	V_2(kcal·mol^{-1})	V_3(kcal·mol^{-1})	V_4(kcal·mol^{-1})
S11	C1	C1	S11	-3.9697	9.1853	-1.7845	2.4383
C2	C1	C1	S11	0	0	0	0
C2	C1	C1	C3	0	0	0	0
C3	C1	C1	S11	0	0	0	0
C10	C9	C9	C9	1.74	-0.16	0.32	0
H26	C10	C9	C9	0	0	0.46	0
H26	C10	C9	H26	0	0	0.32	0
H26	C9	C9	C9	0	0	0.46	0
H26	C9	C9	H26	0	0	0.32	0
S11	C1	C2	C3	0	9.51	0	0
S11	C1	C3	C2	0	9.51	0	0
C1	S11	C1	C2	0	9.51	0	0
C1	S11	S11	C3	0	9.51	0	0
C1	C1	C1	S11	0	9.51	0	0

Table. A4. Torsions parameters

A.2. Other Benchmarking Against DFT

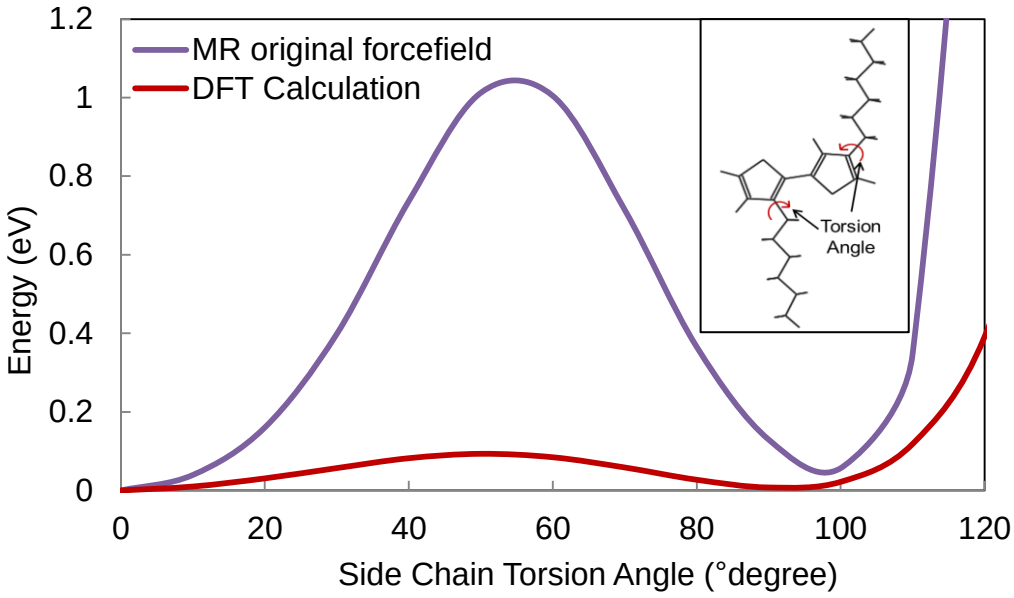

Figure. A2. Energy variation of P3HT mere as a function of side chain torsion angle (c.f. inset) computed using benchmark DFT and MRC forcefield. Close agreement in term of most stable configuration allows us to leave the torsion terms contribution from the side chains intact.

B. Coarse-grained P3HT Forcefield

B.1 Forcefield

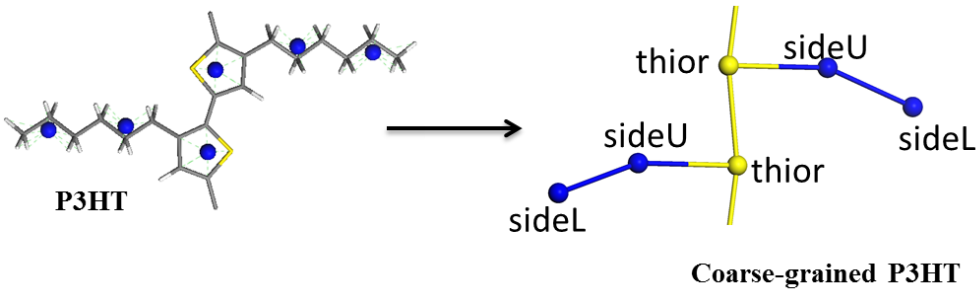

Figure. B1. Forcefield type notations for coarse-grained P3HT system used in this work

Forcefield Type	ϵ (kcal·mol^{-1})	σ (Å)	q (e)
thior	0.4368	3.385	-0.1087
sideU	0.2948	4.517	0.0957
sideL	0.3182	4.287	0.0129

Table. B1. Diagonal Van der Waals parameters and charges

i	j	k_{bonds} (kcal·mol^{-1}·Å^2)	r_0 (Å)
sideU	sideL	633.57	3.861
thior	sideU	2015.05	4.143
thior	thior	925.61	3.924

Table. B2. Bond stretch parameters

i	j	k	k_{angle} (kcal·mol^{-1}·rad^{-2})	θ_0 (degree)
sideL	sideU	thior	448.25	157.74
thior	thior	sideU	505.58	110.08
thior	thior	thior	542.08	171.38

Table. B3. Angle bend parameters

i	j	k	l	V_1(kcal·mol^{-1})	V_2(kcal·mol^{-1})	V_3(kcal·mol^{-1})	V_4(kcal·mol^{-1})
sideU	thior	thior	sideU	-3.97	9.18	-1.78	2.44

Table. B4. Torsions parameters

B.2 Fitting of Short Range Interaction

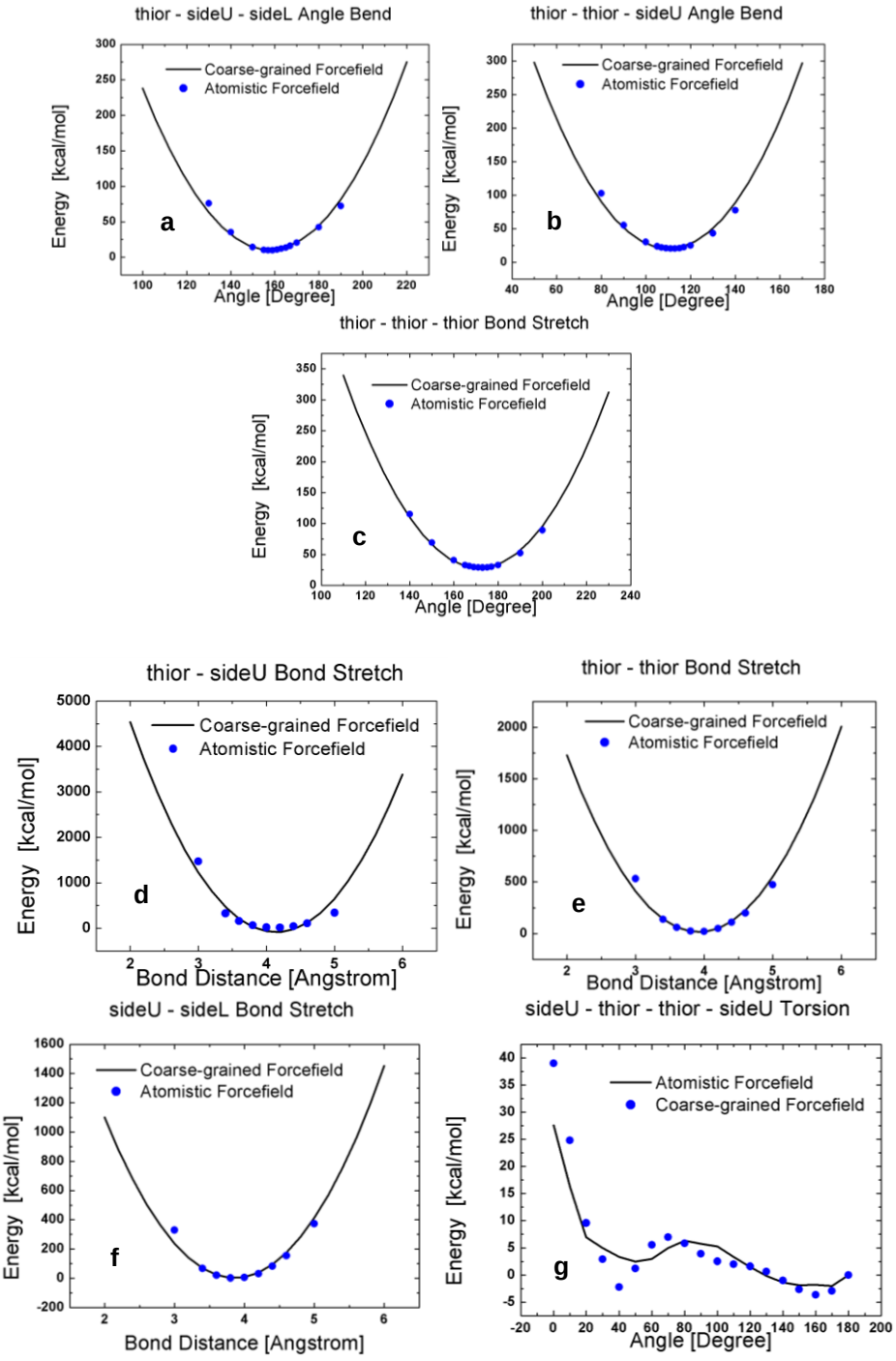

Figure. B2. Fitting against atomistic forcefield was used to obtain short range interaction parameters for coarse-grained forcefield. Here fitting results for all interaction contributions are shown with Angle Bend: a) thior-sideU-sideL, b) thior-thior-sideU and c) thior-thior-thior; Bond Stretch: d) thior-sideU, e) thior-thior and f) sideU-sideL; and Torsion: g) sideU-thior-thior-sideU

C. Coarse-grained PCBM Forcefield

C.1 Forcefield

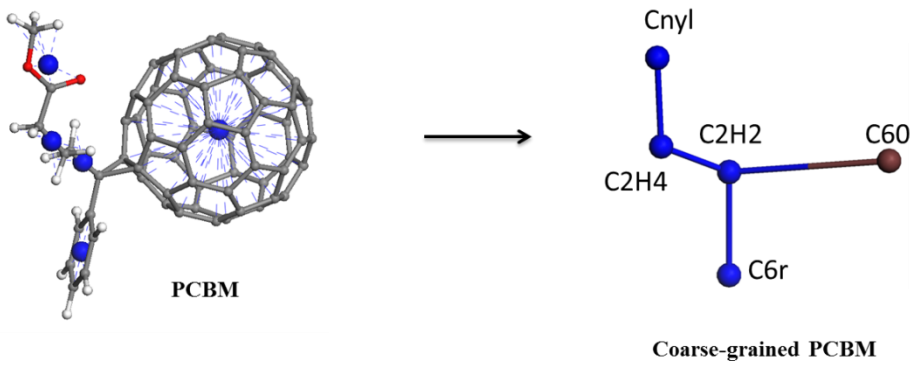

Figure. C1. Forcefield type notations for coarse-grained P3HT system used in this work

Forcefield Type	ϵ (kcal·mol^{-1})	σ (Å)	q (e)
C_2H_2	0.14784	5.438	-0.0280
C_2H_4	0.19404	5.456	0.1060
C_{60}	3.234	9.355	0.0301
C6r	0.4389	3.763	-0.1555
Cnyl	0.47047	6.650	0.0474

Table. B 5. Diagonal Van der Waals parameters and charges

i	j	k_{bonds} (kcal·mol^{-1}·Å^2)	r_0 (Å)
C_2H_4	C_2H_2	526.53	2.579
C_2H_4	Cnyl	853.38	2.963
C_{60}	C_2H_2	1202.30	5.573
C6r	C_2H_2	641.85	3.481

Table. B 6. Bond stretch parameters

i	j	k	k_{angle} (kcal·mol^{-1}·rad^{-2})	θ_0 (degree)
C_2H_2	C_2H_4	Cnyl	519.67	117.32
C_{60}	C_2H_2	C_2H_4	1948.96	126.86
C6r	C_2H_2	C_2H_4	565.19	115.67
C6r	C_2H_2	C_{60}	8984.41	100.37

Table. B 7. Angle bend parameters

i	j	k	l	V_1(kcal·mol^{-1})	V_2(kcal·mol^{-1})	V_3(kcal·mol^{-1})	V_4(kcal·mol^{-1})
Cnyl	C_2H_4	C_2H_2	C60	-57.80	-29.04	-5.35	-6.09

Table. B 8. Torsions parameters

C.2 Fitting of Short Range Interaction

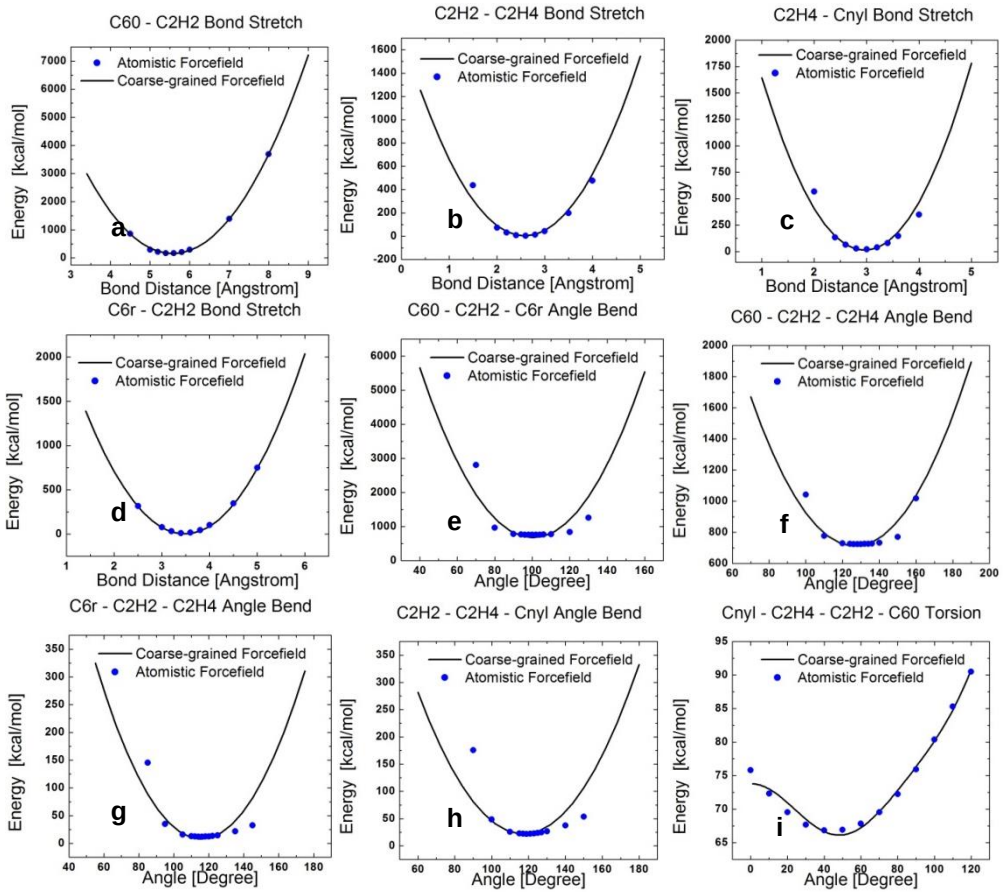

Figure. C1. Fitting against atomistic forcefield was used to obtain short range interaction parameters for coarse-grained forcefield. Here fitting results for all interaction contributions are shown with Bond Stretch: a) C60-C2H2, b) C_2H_2-C_2H_4, c) C_2H_4-Cnyl and d) C6r-C_2H_2; Angle Bend: e) C_{60}-C_2H_2-C6r, f) C_{60}-C_2H_2-C_2H_4 g) C6r-C_2H_2-C_2H_4 and h) C_2H_2-C_2H_4-Cnyl; and Torsion: i) Cnyl-C_2H_4-C_2H_2-C_{60}